教育部補助大專校院延攬國際頂尖人才執行成果簡介

請依下列標題提供中英文版本，影音、照片及檔案若無，可免填。*為必填。

*標題	拓樸量子奈米線中的拓樸近滕效應 The topological Kondo model out of equilibrium
*計畫成果簡述	在量子電腦中，維持量子位元的相干性是能否實現大規模量子計算的關鍵之一，因此找到對於外界擾動相對穩定的材料對於實現量子計算非常重要。近年對拓樸態的研究發現，拓樸態具有全域性，不容易被局域的擾動破壞，因此若能使用拓樸態作為量子位元，將對於實現穩定的量子計算很有幫助。此類拓樸態已被提出能在奈米線中實現，需利用半導體與傳統超導體的鄰近效應。雖然近年在嘗試實現該系統已經很大的進展，但依然缺乏此系統的全域性性質的直接證據。其中一個能顯現出全域性的特性的設計是考慮兩條耦合的奈米線。若兩條奈米線處於拓樸態中，將形成等效的單一自旋，進而造成近滕效應。此效應可在系統的傳輸性質上被觀察到。 在哥本哈根大學尼爾斯·波耳研究所合作的研究中，學者發展出計算耦合奈米線的低溫傳輸性質的演算法，並成功模擬系統中的拓樸近滕效應。目前共有三篇一系列的論文，有一篇已發表在 Phys. Rev. B，另外兩篇預計近期會發表在 Phys. Rev. B 與 Phys. Rev. Letter。 在教學方面，配合國家以及學校的 EMI 全英授課的教學政策，學者每年教授兩門研究所的量子力學，以及一門大學部數值方法與數據分析，皆為 EMI 全英授課的必修課，致力於培養物理的年輕研究人才。 學者同時為本系新成立的計算物理中心的成員，在本計畫期間協助中心建構了總共超過200核心的叢集電腦計算設備，大幅提升系上的計算資源與計算能力。
*成果說明	學術期刊論文： 1. PhysRevB.106.094308.pdf 2. arXiv:2307.03773 3. arXiv:2304.13756 4. arXiv:2303.08376

成果影音	成果影音標題	
	Youtube 網址	
	說明	
成果照片 (請另行提供圖檔)	成果照片	
	照片說明	
成果檔案 (請另行提供檔案)	檔案名稱	PhysRevB.106.094308.pdf 2303.08376.pdf 2304.13756.pdf 2307.03773.pdf

Matrix product state simulations of quantum quenches and transport in Coulomb blockaded superconducting devices

Chia-Min Chung [1,2,3] Matteo M. Wauters [3] and Michele Burrello [3]
[1]*Department of Physics, National Sun Yat-sen University, Kaohsiung 80424, Taiwan*
[2]*Center for Theoretical and Computational Physics, National Sun Yat-Sen University, Kaohsiung 80424, Taiwan*
[3]*Niels Bohr International Academy and Center for Quantum Devices, Niels Bohr Institute, Copenhagen University, Universitetsparken 5, 2100 Copenhagen, Denmark*

(Received 5 July 2022; revised 14 September 2022; accepted 14 September 2022; published 21 September 2022)

Superconducting devices subject to strong charging energy interactions and Coulomb blockade are one of the key elements for the development of nanoelectronics and constitute common building blocks of quantum computation platforms and topological superconducting setups. The study of their transport properties is nontrivial and some of their nonperturbative aspects are hard to capture with the most ordinary techniques. Here we present a matrix product state approach to simulate the real-time dynamics of these systems. We propose a study of their transport based on the analysis of the currents after quantum quenches connecting such devices with external leads. Our method is based on the combination of a Wilson chain construction for the leads and a mean-field BCS description for the superconducting scatterers. In particular, we employ a quasiparticle energy eigenbasis which greatly reduces their entanglement growth and we introduce an auxiliary degree of freedom to encode the device's total charge. This approach allows us to treat nonperturbatively both their charging energy and coupling with external electrodes. We show that our construction is able to describe the Coulomb diamond structure of a superconducting dot with subgap states, including its sequential tunneling and cotunneling features. We also study the conductance zero-bias peaks caused by Majorana modes in a blockaded Kitaev chain and compare our results with common Breit-Wigner predictions.

DOI: 10.1103/PhysRevB.106.094308

I. INTRODUCTION

The study of the transport properties of nanostructures is a pillar in the understanding of semiconducting and superconducting materials and in the engineering of devices for quantum technologies. Quantum dots, single-electron transistors, and superconducting Cooper pair boxes are fundamental building blocks of many of the envisioned devices for quantum information processing based on solid-state architectures, and the main diagnostic tools adopted in their experimental investigation are provided by tunneling spectroscopy. These Coulomb blockaded elements play a crucial role in the design of novel platforms for nanoelectronics and hybrid heterostructures, as the ones adopted, for instance, for the fabrication of topological superconductors. It is therefore of the uttermost importance to develop suitable theoretical and numerical tools to simulate their dynamics and estimate the nonlinear conductance of such nanostructures characterized by strong charging energy effects.

The most common strategies to model the transport across these interacting systems typically rely on master-equation approaches [1] and perturbation theory over the coupling with the external leads (see, for example, the review [2]). Such techniques have been very fruitful in describing many blockaded devices but they often fail in capturing the emergence of nonperturbative phenomena, as the ones characterizing, for example, several impurity problems.

For strongly correlated quantum impurity systems, a plethora of perturbative renormalization group techniques have been developed since the Wilsonian formulation of the renormalization group and numerical renormalization group (NRG) [3,4]. These methods are efficient to describe toy models based on a reduced number of degrees of freedom. They capture indeed the main universal features of the systems under investigation. However, they become computationally demanding when dealing with more realistic scenarios that include a larger number of degrees of freedom, and they suffer from limitations when dealing with nonequilibrium steady states [5,6]. Therefore the development of novel and complementary techniques to study the transport of complex many-body scatterers is a task of considerable importance in the modeling of nanodevices.

In this work, we present a nonperturbative strategy for the evaluation of the nonlinear conductance of blockaded and superconducting quantum scatterers from a microscopic and out-of-equilibrium perspective. In particular, we will address systems with both strong charging energies and sizable couplings with the external leads, while accounting for the backaction of the scatterer onto the leads.

In this respect, tensor networks [7,8] offer a very efficient set of tools to study the dynamics of quasi 1D interacting models, with the possibility of modeling interaction effects in a nonperturbative way, and limitations set instead by the

growth of the entanglement of the system during its time evolution.

We will present an approach based on matrix product states (MPS) and the time dependent variational principle (TDVP) [9,10] to estimate the conductance of blockaded devices through the real-time simulation of their dynamics. This allows us to evaluate the current as a function of time, to derive its transient behavior, and to estimate the transport features of these interacting systems in the stationary limit. We focus in particular on topological superconducting models, where the interplay between charging energy and superconductivity gives rise to the main signatures of Majorana modes observed so far in tunnel spectroscopy experiments [11].

Previous works have successfully applied time-dependent density matrix renormalization group (DMRG) to the study of conductance and noise in the interacting resonant level model out of equilibrium [5,12–18] and to the evaluation of the transport in simple nanostructures [19]. Additionally, hybrid NRG-DMRG techniques have been adopted for simulating the quench dynamics of several quantum impurity models [20,21]. Very recently, the dynamics after a quench of the Anderson impurity models have also been studied through TDVP [22–24].

Our approach is developed from similar techniques: we will consider systems composed by a Coulomb blockaded scatterer and two external leads and we will perform TDVP simulations of their dynamics after a quantum quench. Our algorithm adopts a Wilson chain description of the leads in terms of energy eigenstates inspired by NRG studies. The scatterer is instead represented based on two main technical ingredients. (i) We adopt a BCS mean-field description and, in particular, we employ a (Bogoliubov) single-particle energy eigenstate basis to model the inner degrees of freedom of the scatterer in the MPS; this greatly reduces the entanglement growth during the evolution after the quench. (ii) We introduce an additional degree of freedom that keeps track of its charge dynamics; this allows us to capture the Coulomb charging energy of the system, obviating the violation of its particle number conservation caused by the BCS mean-field Hamiltonian [25]. The combination of these two elements allows us to avoid the necessity of simulating a number-conserving system with long-range interactions (for instance the Richardson-Gaudin model [26], see also the DMRG calculation of the spectra of models involving superconducting leads and quantum dots in Refs. [27–29]), whose dynamics is typically difficult to simulate over sufficiently long time durations.

The quantum quench simulations we perform are reminiscent of the study of quenches in interacting one-dimensional models [30], as, for example, the domain wall melting in the quantum XXZ chains (see, for instance, Refs. [31–34]). In integrable models, these real-time simulations are known to provide good electric and thermal conductance estimates, which typically match the Landauer Büttiker predictions obtained in a bosonization framework [35]. Our calculations extend these results to general interacting models in which a Landauer Büttiker approach cannot be straightforwardly applied.

The rest of the paper is organized as follows. In Sec. II, we describe the general structure of the blockaded systems we analyze. In Sec. III, we discuss the general relation between quantum quench dynamics and transport properties in these systems. In Sec. IV, we outline the main features of our tensor network simulations, and in Sec. V, we present our results for two paradigmatic models of superconducting scatterers, a generic p-wave superconducting quantum dot and the (blockaded) Kitaev chain, which provides a toy model for topological superconductors. For the former, our simulations provide estimates for the cotunneling conductance; for the latter, our nonperturbative approach confirms the validity of the Breit-Wigner prediction in Ref. [36] for small coupling, but evidences the onset of additional effects in a strong coupling regime. Finally we illustrate our conclusions in Sec. VI. Further details on the inclusion of and additional Josephson coupling, the symmetries of our MPS construction, the rate equation estimates and the comparison of different quench protocols are presented in the appendices.

II. MODEL

In this work, we analyze transport problems in Coulomb blockaded devices connected with external one-dimensional metallic leads. To illustrate our method, we focus on systems of spinless fermions and only two leads; however the generalization to spinful models and multiple leads is straightforward.

The general structure of the Hamiltonian we study is

$$\widehat{H}_T = \widehat{H}_{\text{leads}} + \widehat{H}_{\text{sys}} + \widehat{H}_{\text{c}} + \widehat{H}_{\text{tunn}}, \tag{1}$$

where $\widehat{H}_{\text{leads}}$ describes the two metallic leads; $\widehat{H}_{\text{sys}}$ defines the scatterer device whose transport properties are under scrutiny, and it may include interactions and a mean-field superconducting BCS pairing; $\widehat{H}_{\text{c}}$ determines its charging energy, which is the specific interaction responsible for the Coulomb blockaded regime; finally, $\widehat{H}_{\text{tunn}}$ represents the tunneling Hamiltonian between the device and the leads (see the schematic representation in Fig. 1).

The paradigmatic system we consider is a one dimensional p-wave topological superconductor, hence we describe the scatterer as a Kitaev chain [37] with open boundaries. Its charging energy is given by the electrostatic repulsion arising from the finite capacitance of the floating—i.e., not grounded—device. The scatterer energy is thus defined by the following Hamiltonian contributions:

$$\widehat{H}_{\text{sys}} = \sum_{j=1}^{\mathcal{M}} \left[-t_s \hat{d}_{j+1}^\dagger \hat{d}_j + \Delta \hat{d}_{j+1}^\dagger \hat{d}_j^\dagger + \text{H.c.}\right] - \mu_s \hat{d}_j^\dagger \hat{d}_j, \tag{2}$$

$$\widehat{H}_{\text{c}} = E_c(\widehat{N} - n_g)^2, \tag{3}$$

where t_s is the nearest-neighbors hopping amplitude, Δ the p-wave supeconducting pairing, and μ_s the chemical potential. $E_c = \frac{e^2}{2C}$ is the energy associated to the addition of a single charge e to the system, which here we consider to have an effective capacitance C. The electrostatic energy then depends on the difference between the charge of the scatterer $\widehat{N}$ and the charge n_g, typically induced in the experiments by a tunable voltage gate. Importantly, the Kitaev Hamiltonian does not conserve the particle number: superconductivity is indeed included in a BCS mean-field approximation. The device charge $\widehat{N}$, instead, is a conserved quantity if the scatterer is isolated

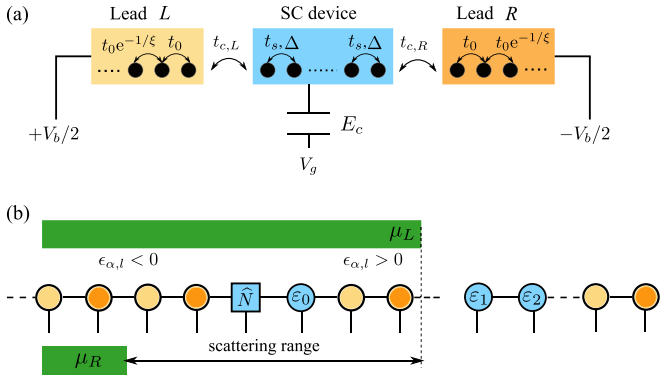

FIG. 1. (a) Sketch of the system we model with matrix product states: a floating superconducting (SC) island is connected to two normal leads, where we measure a single electron current. The gate voltage V_g is used to tune the induced charge on the superconductor $n_g = \frac{eV_g}{2E_c}$. (b) Matrix product state representation of the system. Each MPS site corresponds to a single-particle energy level of either the leads or the SC device (for $t_{c,\alpha} = 0$). Yellow and orange circles represent the single-particle eigenstates of the left and right leads, respectively, ordered by their energies $\epsilon_{\alpha,l}$, whereas blue circles are the quasiparticle states of the superconductor, with energies ε_n. The square MPS site is the bosonic auxiliary site encoding the charge of the device. The leads energy levels are filled up to the corresponding chemical potential $\mu_{L/R}$; the states in the interval $V_b = \mu_L - \mu_R$ are those mostly involved in the transport process.

and it accounts for the charge of both the Cooper pair condensate and the quasiparticle excitations. In particular, the total charge $\widehat{N}$ is different from the operator $\sum_j \hat{d}_j^\dagger \hat{d}_j$, which takes into account only the quasiparticle contribution to the charge; however, they share the same fermionic parity. We emphasize that the Hamiltonian $\widehat{H}_{\rm sys}$ can be easily generalized to different lattice models; in particular, short-range interactions can also be included with additional but affordable computational cost. Hereafter we will label with $\mathcal{M}$ the number of sites involved in $\widehat{H}_{\rm sys}$.

The leads are described by simple one-dimensional nearest-neighbor hopping Hamiltonians

$$\widehat{H}_{\rm leads} = \sum_{\alpha=L,R} \sum_{l=1}^{\mathcal{L}} \left[-t_{0l}^{\alpha} \hat{c}_{\alpha,l+1}^\dagger \hat{c}_{\alpha,l} + \text{H.c.}\right] - \mu_\alpha \hat{c}_{\alpha,l}^\dagger \hat{c}_{\alpha,l}, \quad (4)$$

where $\alpha = L, R$ labels the two different leads. The sites are ordered such that in both leads we start counting from the contact with the scatterer. Notice also that the hopping amplitude can be site dependent: specifically, we choose an exponential decay of the form

$$t_{0l}^{\alpha} = t_0 e^{-(l-1)/\xi}, \quad (5)$$

with a decay length $\xi < \mathcal{L}$, building what is known in the literature as Wilson chain [3,38,39]. Physically, it corresponds to a logarithmic discretization of the original continuous Hamiltonian, where the lattice spacing increases as we move farther away from the scatterer. This choice provides two main advantages, which will become clearer in the following section: first, there are more eigenvalues with energies close to the Fermi level, which increases our resolution close to zero voltage bias in the quench protocols; second, the exponentially decaying hopping prevents the current to reach the end of the leads, acting as a sort of effective sink. This improves the convergence in time towards the intermediate quasi-steady-state we are interested in to compute transport properties. In the rest of the paper, we consider the two leads as equivalent under inversion symmetry, so we can drop the α index in the hopping amplitude, and we set the zero of the energy at the Fermi level corresponding to half-filled leads.

Finally, the tunneling between leads and system is described by

$$\widehat{H}_{\rm tunn} = -t_{c,L}\left(\hat{d}_1^\dagger \hat{c}_{L,1} + \text{H.c.}\right) - t_{c,R}\left(\hat{d}_{\mathcal{M}}^\dagger \hat{c}_{R,1} + \text{H.c.}\right). \quad (6)$$

In the following, we will also consider $t_{c,L} = t_{c,R} = t_c$ for the sake of simplicity.

III. TRANSPORT PROPERTIES FROM QUANTUM QUENCHES

Our main goal is to compute the conductance of a given device from its nonequilibrium dynamics, without relying on perturbative approaches. To this purpose, we simulate the time evolution of the system after a quantum quench and extract the conductance from the emerging quasisteady state.

In the thermodynamic limit and for noninteracting models, the system relaxes toward a nonequilibrium steady-state with a current flow corresponding to the prediction of the Landauer-Büttiker (LB) formula [40] after a quench in which leads with different densities are suddenly connected at time $\mathrm{t} = 0$ ($t_c(\mathrm{t}) \propto \Theta(\mathrm{t})$, with Θ being the Heaviside step function). In finite systems, instead, the LB regime appears only as a transient [41] before the current is reflected back from the edges (see Fig. 2 for a qualitative example) and eventually a trivial steady state is reached. An estimate of the conductance of the system must rely on this transient nonequilibrium quasi steady state (NEQSS) which is, therefore, the object of our investigation. When the lead Hamiltonian $\widehat{H}_{\rm leads}$ includes only local terms, the post-quench time evolution obeys a Lieb-Robinson bound [42,43]; the central scatterer region is not affected by the finite size effects of the simulation until the quasiparticles excited by the quench in the central region reach the boundaries and come back. Therefore we can consider the NEQSS as a faithful representation of what happens in the thermodynamic limit (see, for instance, Refs. [31,40,44,45]).

To bring the system out of equilibrium, we can consider two different quench protocols [41].

(1) *μ quench*. The system is initially prepared in the ground state of $\widehat{H}_T$ where both leads have the same chemical potential. At $t = 0$, a voltage bias $V_b = \mu_L - \mu_R$ is introduced and the system evolves accordingly to the new Hamiltonian $\widehat{H}_T(V_b)$.

(2) *Density quench*. The device and the leads are initially decoupled and the system is prepared in the ground state of $\widehat{H}_{\rm sys} + \widehat{H}_{\rm leads}$, where a voltage bias V_b is used to induce a density difference between the two leads. At $\mathrm{t} = 0$, the bias is turned off and the system evolves with $\widehat{H}_T$.

After the quench, me measure the current in the leads, following the definition:

$$I_{\alpha,l}(\mathrm{t}) = 2\pi i t_{0l}^{\alpha} \langle \Psi(\mathrm{t}) | \hat{c}_{\alpha,l+1}^\dagger \hat{c}_{\alpha,l} - \hat{c}_{\alpha,l}^\dagger \hat{c}_{\alpha,l+1} | \Psi(\mathrm{t}) \rangle, \quad (7)$$

where $|\Psi(\mathrm{t})\rangle$ is the time-evolved many-body wave function.

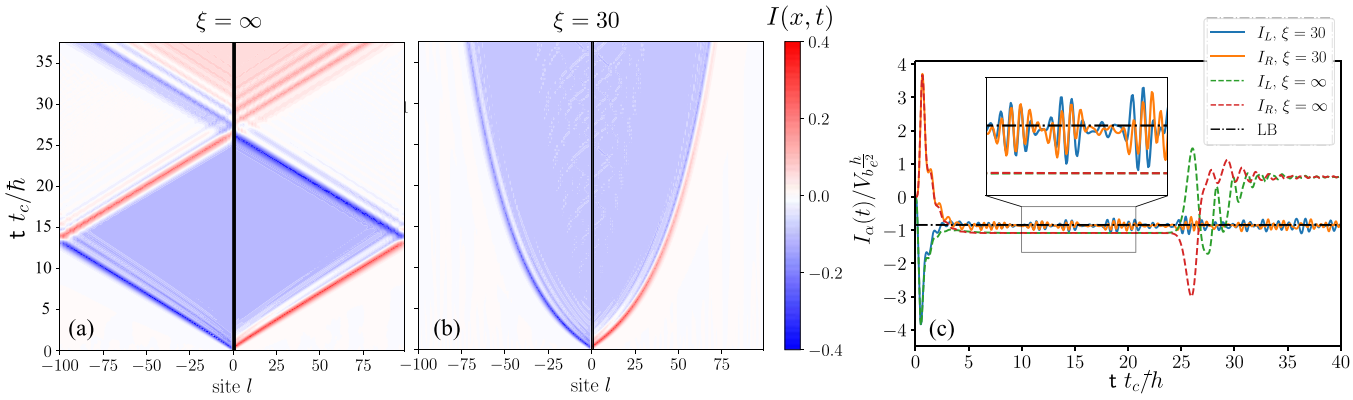

FIG. 2. Exact evolution of a noninteracting impurity model. (a) Space-time profile of the current, with uniform hopping in the leads. The vertical black lines mark the position of the impurity site. (b) Space-time profile of the current when the hopping in the leads decays exponentially with a characteristic length $\xi = 30$. (c) Comparison between the time evolution of the current at the left and right edge of the scattering region, for uniform leads ($\xi = \infty$, dashed lines) and Wilson chains ($\xi = 30$, solid lines). The horizontal dot-dashed line indicates the Landauer-Büttiker prediction. The inset zooms in the time interval $\mathrm{t}t_c/\hbar \in [10, 20]$; the left and right currents for $\xi \to \infty$ are perfectly superimposed. The energy of the impurity site is $\varepsilon_{\mathrm{imp}} = 0.1t_0$ and the bias is chosen to be in resonance, hence $V_b = \varepsilon_{\mathrm{imp}}$. The other parameters are $\mathcal{L} = 100$ and $t_c = 0.25t_0$.

Although for small biases the two quench protocols give consistent results, they are not exactly equivalent. This can be easily seen if we consider a noninteracting case and the related structure of its scattering matrix in one dimension. In the μ quench, the leads have different chemical potential, meaning that an energy step is added on top of the scattering matrix of the device. Hence, momentum is not conserved when a particle is transmitted across the device. In the density quench, instead, far from the device the two leads have the same chemical potential and the momentum is a good quantum number for the scattering process.

In our simulation, we have verified that the density quench protocol gives usually better results for the estimates of the conductance, both in terms of a shorter relaxation time before reaching the quasisteady state and a more stable current profile. Thus, unless otherwise stated, all the results we present are obtained with the density quench protocol. Concerning the simulation of the time evolution of the system, however, both quench protocols can be implemented with analogous accuracy.

To illustrate the main physical properties and limitations of studying transport properties through quantum quenches, we discuss next the performance of the method on a noninteracting impurity model. First, let us consider the situation where the leads have a uniform hopping amplitude, corresponding to an infinite decay length $\xi \to \infty$. The single site impurity with energy $\varepsilon_{\mathrm{imp}}$ is described by the Hamiltonian $\widehat{H}_{\mathrm{sys}} = \varepsilon_{\mathrm{imp}}\hat{d}^\dagger\hat{d}$. In Fig. 2, we summarize the main characteristics of the quench protocol. The system is initialized with a density imbalance between the left and the right leads, which induces a current flow in the chain. At first, the current involves only the sites immediately adjacent to the impurity. The initial discontinuity in the density profile splits into two fronts counterpropagating along the two leads with constant speed in the whole system. This is clearly shown in Fig. 2(a), where we plot the evolution of current density $I(\mathrm{t})$ in time and space. In particular, we emphasize than inside this broadening "cone" a NEQSS emerges, carrying a steady current consistent with the LB result, as seen in Fig. 2(c).

However, the finite length of the chain has two consequences: the first, and more obvious, is that the current is reflected back from the edges of the leads and the NEQSS changes when this signal reaches again the edges of the scatterer. In general, different NEQSS exist inside each of these rhomboids confined by the propagating signal, as suggested by the different plateaus displayed by the data corresponding to uniform leads ($\xi = \infty$, dashed lines) in Fig. 2(c). Eventually, the system will reach a trivial steady-state with zero current.

The second consequence is the limit on the energy resolution due to the finite level spacing in the leads which is of the order $2t_0/\mathcal{L}$. This becomes particularly important when computing the current from a small voltage bias, because in the initial state the particle number in the two leads will differ only by a few units. As a consequence, the current develops finite size corrections which deviate from the exact LB formula, again visible from Fig. 2(c). Analogous issues emerge also for the μ quenches.

Both these problems are partially cured by choosing a finite decay length for the leads' hopping amplitude, as reported in panels (b) and (c) of Fig. 2. Indeed, now the reflection from the edges of the system is strongly suppressed and quasistationary state survives for longer time. Also the finite size corrections with respect to the LB formula are reduced, at the cost of a noisier current signal. However, this noise is easily eliminated by averaging the current in time, after the plateau is reached.

Physically, the Wilson chain construction in Eqs. (4) and (5) can be thought as a real space renormalization applied to the leads [3,38], where the further we are from the contact with the scatterer, the more chain sites are merged together. By comparing panels (a) and (b) in Fig. 2, it is easy to realize that the introduction of the exponential dumping of the tunneling amplitude t_0 amounts to a compression of the

spreading correlation cone. While in the uniform chain the signal travels with constant Fermi speed $v_f = 2t_0$, leading to a space-time profile $\mathsf{t} = \frac{l-1}{2t_0}$, in the Wilson chain the speed is exponentially damped. This results in the space-time profile $\mathsf{t} = \frac{\xi}{2t_0}(e^{(l-1)/\xi} - 1)$. In this way, we can simulate effectively larger system sizes, thus reducing the finite size effects. This construction modifies also the spectrum of the leads: the eigenvalue spacing is denser at low energies, thus allowing a finer resolution at small voltage biases.

The main difficulty of this approach is the choice of a proper decay length; if ξ is too large, its effect is negligible and if it is too small the current is reflected back from the effective edge created by the vanishing hopping amplitude. This trade-off also depends on the strength of the bias, since larger values of V_b also require larger decay length. In our MPS simulations, we adjust heuristically the value of ξ by choosing a value that does not introduce a nonphysical reflection in the current before the lead edges.

For the rest of the paper, unless otherwise specified, the leads will be described by two chains of $\mathcal{L} = 100$ sites, with a bare hopping amplitude $t_0 = 1$ that sets all other energy scales in the model and a decaying length $\xi = 40$. The latter has been chosen in such a way that all the data we present do not display an artificial reflection of the current from the edges and the signal converges fast enough enabling us to average it over a sufficiently large time interval.

IV. MATRIX PRODUCT STATE IMPLEMENTATION

We implement the quench dynamics of the systems by using matrix product state (MPS) techniques [7]. As all tensor network techniques, the underlying approximation restricts the maximal entanglement allowed in the simulated state at any time. In particular, we adopt a maximum bond dimension χ which varies as a function of time and is not uniform in the MPS construction. In the following numerical simulations, the maximum bond dimension is limited by $\chi \lesssim 2500$, which implies that the simulation of the time evolution of the system is reliable until the correlations between its partitions are below a suitable threshold, which can be estimated by the maximum value of the entanglement entropy $S_{\max} = \log_2 \chi$.

Concerning the quench protocol, we will focus on the density quench presented in Sec. III: the scatterer is initially decoupled and the voltage bias V_b is symmetrically applied ($\mu_L = -\mu_R = V_b/2$) to induce different electron densities in the two leads before the quench, corresponding to their Fermi-Dirac distribution at zero temperature. The initial state is thus composed by the product of the independent ground states of the leads and the scatterer. The ground state in the noninteracting leads is simply a free-electron state; however, interacting leads can be considered as well and they can be initialized through density matrix renormalization group (DMRG) [46,47] calculations. DMRG can be adopted to initialize the scatterer in its ground state as well. At time $\mathsf{t} > 0$, the system is quenched to a Hamiltonian with no bias, while the scatterer and the leads are coupled by the tunneling interaction $\widehat{H}_{\text{tunn}}$ (we present a comparison with the μ-quench protocol in Appendix D).

Our aim is to tackle superconducting and blockaded devices, with the possibility of describing the out-of-equilibrium physics of setups with large voltage bias and sizable tunneling interactions between the leads and the scatterer. In the following, we discuss in detail the construction of our computational basis, its consequences and the introduction of the charging energy in a number nonconserving model.

The method is implemented by using ITensor library [48]. The source code can be found in Ref. [49].

A. Energy basis

A well-known challenge for the simulations of the dynamics of out-of-equilibrium many-body systems with tensor network techniques is the growth of their entanglement in time [50]. To reduce the entanglement, Rams and Zwolak proposed a basis which mixes an energy eigenbasis for the tight-binding lead description and a real-space basis for the scatterer [22]. With such a choice, the entanglement is greatly reduced from a linear to a logarithmic growth with time (see Appendix B for more details).

In the following, we adopt this strategy and we use a single-particle eigenbasis of $\widehat{H}_{\text{leads}}$ for the leads, with MPS sites ordered by increasing energy. The Wilson chain approach allows us to get a higher resolution in energy close to the Fermi level, thus in the energy window in which the dynamics has major effects. Concerning the scatterer degrees of freedom, we may adopt different bases depending on the physical system and we discuss the details of their choice in Sec. IV C.

In particular, for BCS Hamiltonians in the form of Eq. (2) and charging energy (3), we represent the scatterer through MPS sites associated with its Bogoliubov quasiparticles, and we complete the system description by including an additional MPS site to account for the scatterer total charge (see Sec. IV B). Figure 1(b) shows a schematic representation of the MPS construction that relies on this energy basis, and the initial occupation of the lead sites is based on their chemical potential.

As a result of this construction, during the time-evolution of the system we can identify three energy intervals: for energies considerably smaller than $-V_b/2$ the eigenstates of the leads are approximately frozen in an occupied state, for energies larger than $V_b/2$, the eigenstates of the leads are equally frozen in the empty state; in the intermediate *scattering range*, the states of the scatterer and the leads strongly interact and develop nontrivial correlations.

We illustrate this behavior in Fig. 3 for a simple model of a superconducting (SC) quantum dot with two quasiparticle states and charging energy given by Eq. (3); the way of dealing with the charging energy will be introduced later in Sec. IV B. Inside the scattering range (yellow shading), we can clearly observe the onset of resonances identified by the variation in time of the occupation number of the two leads at energies set by the energy differences among many-body states of the scatterer. These are identified by the vertical dashed lines in Figs. 3(a)–3(c) and such resonances are consistent with the results of the standard rate equation approaches [1,2]. The initial lead distributions are taken at zero temperature and the resulting width of the depletion/filling regions following the quench is set by the coupling strength t_c between the leads and the SC device. Physically, this corresponds to a regime where the broadening of the device energy levels

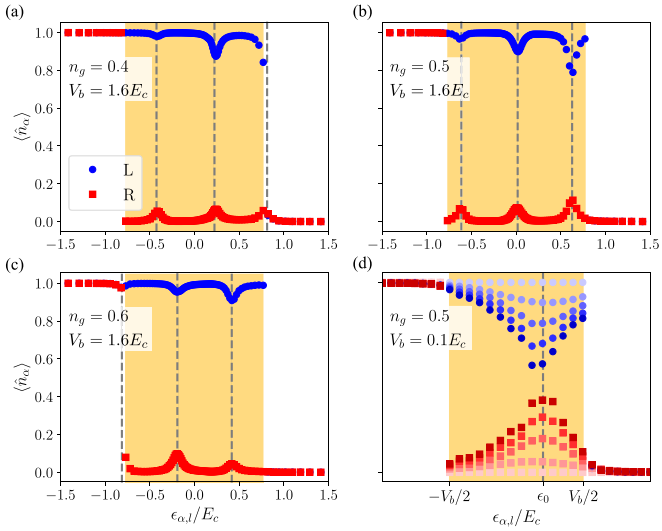

FIG. 3. Time evolution of SC quantum dots with two quasiparticle states of energies $\varepsilon_0 = 0.02E_C$ and $\varepsilon_1 = 0.6E_c$. The coupling with the leads is $t_c = 0.2E_c$ and $E_c = t_0$. [(a)–(c)] Occupation number $\langle \hat{n}_\alpha \rangle$ of the energy levels in the two leads as a function of their energy $\epsilon_{\alpha,l}$ after a quench, once the NEQSS is reached ($\mathfrak{t} \sim 20\hbar/t_c$). Vertical dashed lines correspond to the resonances with the transitions between different many-body states in the device. The panels refer to induced charges $n_g = 0.4,\ 0.5$, and 0.6. (d) Time dependence of the occupation number close to a resonance for small bias $V_b = 0.1E_c$. The color progression from light to dark indicates longer evolution times; the data refer to $\mathfrak{t} = [0, 20, 40, 60, 80]$ in units of $\hbar/t_c$. Vertical dashed lines highlight the resonance at $\varepsilon_0 = 0.02E_c$, while the shaded areas indicate the scattering window given by the voltage bias.

induced by the hybridization with the leads is larger than the temperature.

The time evolution of the occupation numbers of the leads eigenstates close to a resonance is summarized in Fig. 3(d); as time increases (from lighter to darker colors), the leads are progressively depleted/filled. The NEQSS we are interested in survives as long as there is a sufficient difference between the occupation numbers of the left and right leads.

In simulation efficiency, the advantage of adopting the energy eigenbasis is two-fold: (i) Contrary to a real state basis, most of the leads and device states are only marginally involved in the time evolution, thus the entanglement growth is limited to the scattering energy range, consistently with Ref. [22]. (ii) This approach allows us to evaluate the conductance also for moderately large bias voltage, which is typically a difficult task for a real space basis.

Notwithstanding that the coupling between the leads and the scatterer becomes nonlocal in the energy basis, $\widehat{H}_{\text{tunn}}$ can be expressed in terms of matrix product operators (MPOs) of small bond dimensions [22] (in the implementation by ITensor, the MPO can be generated by AutoMPO). As we will discuss in the following, such MPO will also take into account the nonlocal charging energy effects. As a consequence, the dynamics of the system can be efficiently simulated by using TDVP [9,10]. In practice, we use TDVP with single-site update together with Krylov subspace expansion [51]. The subspace expansion is performed in advance of the TDVP evolution at each time step.

We mention that for leads with local interaction (as in the case of Luttinger liquids), the MPO bond dimension in the energy basis typically grows proportional with the system size [7]. In this case, the advantage of such a basis is reduced with respect to the real-space choice, which, however, has been proved efficient to simulate transport in systems with simple scatterers [5,12–19,52].

We finally remark that our energy basis choice is opposite and complementary with respect to several other techniques, including both NRG, where typically one works in a basis such that the Hamiltonian defines an effective 1D tight-binding chain with local interactions only, and recent studies of quench dynamics in Anderson impurity models [23,24], where an alternative ordering of the MPS sites has been proposed in a position basis, in order to alternate filled and empty leads sites and simplify the description of particle-hole pairs.

B. Charging energy and superconducting scatterers

The BCS mean-field description of a superconducting system does not preserve its particle number, but only its parity. This implies that the charge $\widehat{N}$ of the scatterer cannot be simply deduced by considering the occupation of the sites of its tensor network description; therefore, to account for the charging energy interaction $\widehat{H}_c$, the MPS construction must be suitably extended. To this purpose, inspired by the approach adopted in Ref. [25], we add an auxiliary bosonic site to our tensor network representation of the system (we locate it at the center of the whole MPS chain). This MPS site behaves as a counter for the number of particles in the scatterer and it is defined by a local Hilbert space spanned by the eigenstates $|N\rangle$ of the scatterer charge $\widehat{N}$.

To keep the Hilbert space dimension of the auxiliary site finite, we introduce a truncation parameter $N_{\max}$, such that in our simulations we consider only a set of $2N_{\max} + 1$ orthogonal charge states $|N\rangle$ with $N \in [-N_{\max}, N_{\max}]$ (for n_g taken between -1 and 1, otherwise we can shift this range). The operator $\widehat{N}$ is diagonal in this basis and, in particular, describes the charge variation of the scatterer around the reference value $N = 0$, which corresponds to the ground state of the isolated superconductor in absence of induced charge ($n_g = 0$). Given the charge truncation parameter $N_{\max}$, our tensor network description provides reliable results when the charging energy E_c is sufficiently large, such that the fluctuations of the charge of the scatterer, determined by the coupling with the leads (and, potentially, by additional Josephson terms) are much smaller than $N_{\max}$. In our simulations, we verified indeed that for strong charging energies, thus in the case of Coulomb blockaded device, the population of states far from $N \sim n_g$ is exponentially suppressed and at the cutoff $\pm N_{\max}$ it remains below machine precision.

As a general rule, the introduction of such an auxiliary degree of freedom must be accompanied with a physical constraint. Here, we impose that the parity $(-1)^{\widehat{N}}$ of the auxiliary site needs to be the same as the parity of the occupation of the scatterer sites. Namely, let us define the operator:

$$\widehat{P} = (-1)^{\widehat{N} + \sum_{i=1}^{\mathcal{M}} \hat{d}_i^\dagger \hat{d}_i}. \tag{8}$$

For any physical state $|\psi_{\rm phys}\rangle$, the constraint

$$\widehat{P}|\psi_{\rm phys}\rangle = |\psi_{\rm phys}\rangle \tag{9}$$

must hold. Besides this physical requirement, we also observe that the total number of particles,

$$\widehat{N}_{\rm tot} = \widehat{N} + \sum_{\alpha=L,R}\sum_{i=1}^{\mathcal{L}} \hat{c}^\dagger_{\alpha,i}\hat{c}_{\alpha,i}, \tag{10}$$

is a conserved quantity. Our MPS and MPO constructions encode both the $\mathbb{Z}_2$ constraint (9) and the global symmetry associated to Eq. (10) through suitable quantum numbers in its virtual indices. Due to the peculiarities of the conserved operators $\widehat{P}$ and $\widehat{N}_{\rm tot}$, the local symmetry properties of the tensors associated with lead and scatterer sites are different. In particular, the parity constraint affects only the auxiliary and the scatterer sites, whereas the particle number conservation affects only the auxiliary and the lead sites (see Appendix A for more detail).

Based on this MPS construction, the charging energy term $\widehat{H}_{\rm c}$ can be included in a straightforward way in the MPO description of the Hamiltonian, since it simply corresponds to a diagonal operator acting locally on the auxiliary site.

More care is needed instead in the definition of the tunneling operators from the leads to the scatterer, which must be dressed with suitable operators acting on the auxiliary site. To this purpose, we define the operators

$$\widehat{\Sigma}^+ = \sum_{N=-N_{\rm max}}^{N_{\rm max}-1} |N+1\rangle\langle N| \quad \text{and} \quad \widehat{\Sigma}^- = (\widehat{\Sigma}^+)^\dagger, \tag{11}$$

which respectively raise and lower by 1 the scatterer charge $\widehat{N}$; the tunneling Hamiltonian acquires the form:

$$\widehat{H}_{\rm tunn} = -t_c\left[\hat{d}^\dagger_1\hat{c}_{L,1}\widehat{\Sigma}^+ + \hat{d}^\dagger_{\mathcal{M}}\hat{c}_{R,1}\widehat{\Sigma}^+ + \text{H.c.}\right], \tag{12}$$

where the lead operators $\hat{c}$ and the scatterer operators $\hat{d}^\dagger$ are taken in the real space basis. In the BdG basis which will be introduced below, the creation and destruction operators must be rewritten as the proper linear combination of eigenstates in the chosen representation. Independently from the basis choice, $\widehat{H}_{\rm tunn}$ becomes a sum of nonlocal three-site operators, acting simultaneously on one lead, the scatterer and the auxiliary charge site. Despite the apparently complicated structure, the whole Hamiltonian can be efficiently represented by an MPO of bond dimension 10. The related dynamics can thus be conveniently evaluated through a TDVP approach.

C. Quasiparticle basis

Depending on the considered model and the corresponding $\widehat{H}_{\rm sys}$, we can apply different basis choices for the scatterer. The simplest is a real-space basis, in which the scatterer sites are kept together, ordered by their positions and located in proximity of the zero-energy single-particle states of the leads. This choice is convenient in the presence of local interactions within the scatterer Hamiltonian $\widehat{H}_{\rm sys}$. Instead, when the only interaction is provided by the charging energy $\widehat{H}_{\rm c}$, and the mean-field superconducting pairing is present [e.g., the SC quantum dot model analyzed in Fig. 3 or the Kitaev chain model described by Eq. (2)], the best option for the basis is given by the quasiparticle energy eigenstates derived from the quadratic Bogoliubov - de Gennes (BdG) formulation of the corresponding Hamiltonians. Accordingly, to study such models, we developed a MPS description of the scatterer based on the occupation number of the Bogoliubov eigenmodes $\hat{\gamma}_j$ that diagonalize the BCS Hamiltonians $\widehat{H}_{\rm sys}$. This choice greatly speeds our simulations of the system dynamics because it avoids the strong entanglement growth caused by the formation of Cooper pairs that characterizes the real-space basis. In the single-particle energy eigenbasis, only the considerably weaker entanglement between quasiparticles contributes indeed to the entanglement entropy built during the time evolution.

In this basis, the scatterer Hamiltonian reads

$$\widehat{H}_{\rm sys} = \sum_{j=1}^{\mathcal{M}} \varepsilon_j \hat{\gamma}_j^\dagger\hat{\gamma}_j - \frac{1}{2}\sum_{j=1}^{\mathcal{M}}(\varepsilon_j + \mu_s), \tag{13}$$

where ε_j and $\hat{\gamma}_j^\dagger$ are the quasiparticle energies and creation operators, corresponding to the *positive* eigenenergies of the BdG Hamiltonian. The first and the second term correspond to the excited states and the ground state energies, respectively. In this basis, the real-space operators $\hat{d}_i$ acquire the form $\hat{d}_i = \sum_{j=1}^{\mathcal{M}} u_{ij}\hat{\gamma}_j + v^*_{ij}\hat{\gamma}_j{}^\dagger$. We stress that although the complete BdG Hamiltonian has $2\mathcal{M}$ eigenstates, half of them with positive energies and half of them with negative energies, the $\mathcal{M}$ positive energy states are enough to form a complete set due to particle-hole symmetry. Therefore the number of basis states in the new basis remains unchanged. Furthermore, this construction does not rely on any particular symmetry in the quadratic Hamiltonian $\widehat{H}_{\rm sys}$, such that we can easily introduce local potentials, disorder or position-dependent tunneling and coupling terms.

As discussed in the previous section, the first step in the simulation of the time evolution of the system for the density quenches requires to determine the ground state of the scatterer. Since $\widehat{H}_{\rm sys}$ and $\widehat{H}_{\rm c}$ are completely decoupled in our representation, this ground state is the tensor product of two parts referring to the Bogoliubov quasiparticles and the auxiliary charge site. Such tensor product can display either even or odd fermionic parity and it respectively assumes the form $|\psi^+\rangle|N=0\rangle$ or $|\psi^-\rangle|N=1\rangle$, for $n_g \in [0,1]$. These are indeed the combinations that fulfill the physical constraint in Eq. (9).

In the quasiparticle basis, $|\psi^+\rangle$ and $|\psi^-\rangle$ are simply the vacuum state and the state $|1,0,0,\ldots\rangle$, respectively; for general bases and $\widehat{H}_{\rm sys}$, $|\psi^\pm\rangle$ can be computed by DMRG. The ground state is then determined as the state of lower total energy including both the contributions of $\widehat{H}_{\rm sys}$ and $\widehat{H}_{\rm c}$, and it is adopted to initialize the time evolution.

To illustrate the efficiency of the quasiparticle basis, we consider a Kitaev chain in the topological phase and compare the convergences to a NEQSS under small voltage bias obtained by using two different basis for the MPS construction: the first corresponds to the free electron eigenbasis of the kinetic term t_s only [see Eq. (2)]; in this case, the pairing term is included in the MPO; the second corresponds instead to

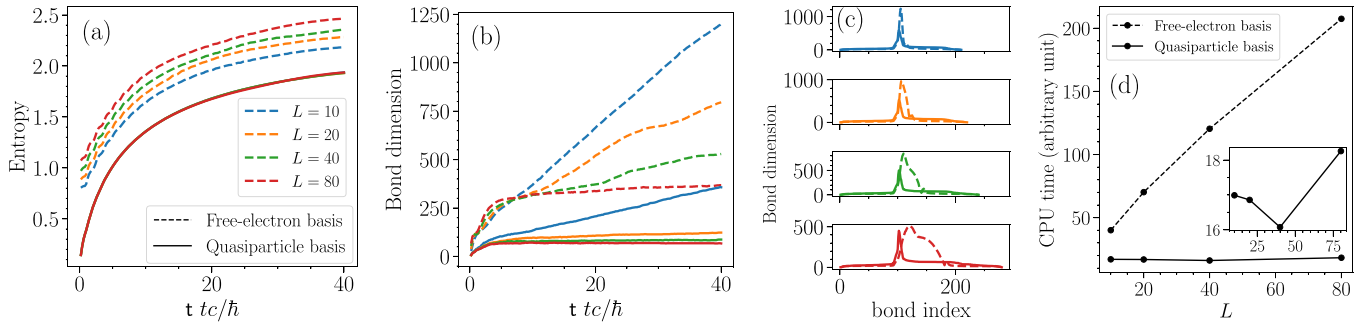

FIG. 4. Comparisons for quench dynamics between a free electron basis (dashed lines) and the Bogoliubov quasiparticle basis (solid lines). The scatterer is a Kitaev chain with parameters $E_c = t_0$, $t_s = 0.4E_c$, $\mu_s = -0.1E_c$, $\Delta = 0.5E_c$, $t_c = 0.2E_c$, $n_g = 0.5$, and $V_b = 0.1E_c$, the same with Fig. 5. (a) Maximal entanglement entropy and (b) largest bond dimension reached in the time evolution. (c) Bond dimension on each bond in the MPS. (d) CPU time for the whole simulations for different scatterer lengths. The inset is a zoom in of the solid curve.

the Bogoliubov quasiparticle basis, which already takes into account the superconducting pairing. As shown in Fig. 4(a), for the free electron basis, the entanglement entropies become progressively larger for longer systems (dashed lines). Instead, for the Bogoliubov quasiparticle basis, the entanglement entropies are basically independent on the system length, and are smaller than the entropies in the free electron basis. Surprisingly, the largest bond dimensions required by the algorithm during the time evolution become smaller for longer chains in both bases, as shown in Fig. 4(b). This can be understood as an effect of the finite overlap acquired by the Majorana edge-modes for short chains, which enhances the entanglement. For all lengths, the largest bond dimensions reached in the Bogoliubov basis are smaller than the bond dimensions in the free electron basis. Another advantage of using the quasiparticle basis can be seen in the bond dimension distribution on each bond in the MPS. As shown in Fig. 4(c), the region of large bond dimension is broader in the free electron basis than in the quasiparticle basis. This is because under small voltage bias the transport is mainly contributed by the Majorana bound state (MBS), which corresponds to a single site in the quasiparticle basis, whereas in the free-electron basis, the MBS is an entangled state spread through the whole scatterer region. Figure 4(d) shows the comparison of CPU times. The Bogoliubov quasiparticle basis is in general more efficient than the free electron basis, and the advantage becomes stronger when the system length is larger.

The construction we presented can be extended, in full generality, by considering any arbitrary quasiparticle basis for the device, and considering a suitable tunneling matrix between the leads and the scatterer. In particular, for the modeling of the transport across specific nanostructures, one may want to consider only a selected number of low-energy single-particle eigenstates by including only the most relevant states involved in the transport process, rather than starting from a tight-binding microscopic model such as Eq. (2). This kind of approximation has been successfully applied, for instance, to study Coulomb blockaded transport within the framework of rate equations [53,54]; our MPS representation can easily be adapted to this approach and, together, they also provide a systematic way of improving the resulting conductance estimates by increasing the number of low energy states included in the scatterer description.

V. PHYSICAL EXAMPLES

In this section, we benchmark our method on two test systems: a p-wave SC quantum dot with two quasiparticle states and a Kitaev chain. We will use the Kitaev chain to illustrate the main features of our method as well as its limitations, whereas the small Hilbert space dimension of the quantum dot allows for faster simulations and an easier characterization of the Coulomb blockaded structure.

In general, we simulate the nonequilibrium dynamics following a density quench. For any choice of n_g and V_b, the system is initially prepared in the corresponding ground state with no couplings between the leads and the device ($t_c = 0$). At $\mathsf{t} = 0$, we turn the tunnel coupling t_c on and quench the voltage bias to zero; the transport properties of the system are then estimated based on the NEQSS reached after the initial transient time. Throughout all the simulations, the main observable we measure is the current flowing from one lead to the other as a function of the voltage bias V_b and the induced charge n_g. The current is measured on both edges of the central device, in the first links *entirely* in the leads [$l = 1$ in Eq. (7)], to facilitate comparison between data associated to different couplings between the leads and the scatterer or hopping decay length in the leads. Since we always consider superconducting models and symmetric voltage drops, we assume that the current $I(V_b, n_g)$ is an odd function of the voltage bias, hence we perform all simulations for $V_b > 0$, corresponding to a particle current flowing from left to right. After the current has converged to the stationary value, we divide each data set in several batches from which we compute its average value and standard deviation. From the current, we compute the differential conductance $G = dI/dV_b$ using a fourth-order discrete derivative method. Other meaningful observables we can extract are the charge on the SC island and the entanglement entropy on each link, which is naturally obtained during the singular value decomposition (SVD) performed at each step of the time evolution.

To give an example of the behavior of these quantities in the quench protocol, we report in Fig. 5 the results for a topological Kitaev chain of $\mathcal{M} = 40$ sites at the charge degeneracy point $n_g = 0.5$ and a small voltage bias $V_b = 0.1E_c$. Panel (a) reports the postquench time dependence of the current at the left and right edges of the scatterer; its behavior is very

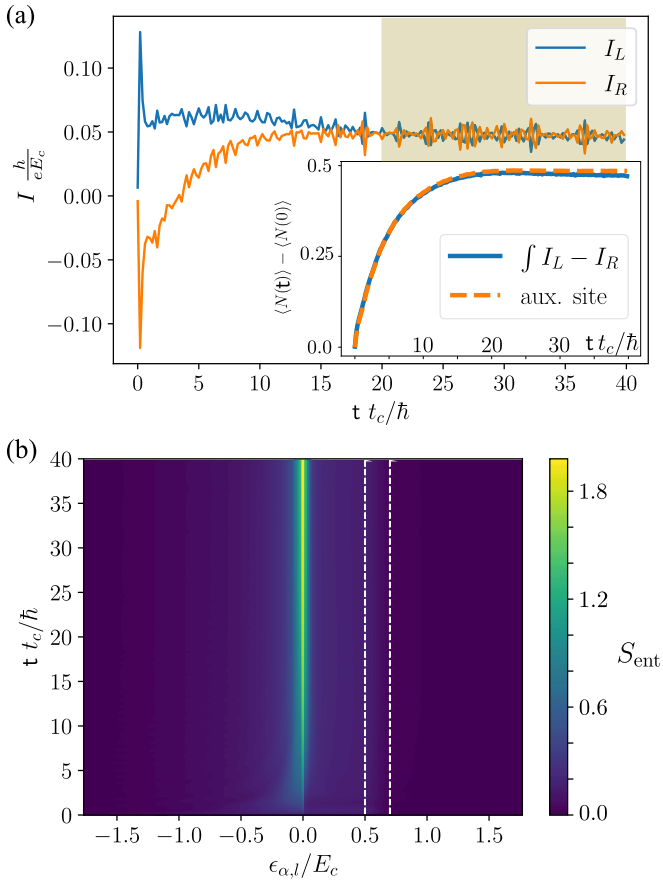

FIG. 5. (a) Evolution in time of the left and right currents (I_L and I_R, respectively) after the density quench. The shaded area corresponds to the interval where we average the current to extract its steady-state value. The inset shows the change in time of the charge of the SC island, both as the average particle number in the auxiliary site (dashed line) and as the integral of the current difference between the left and right contact (solid line). (b) Entanglement entropy at each bond of the MPS chain. The two vertical dashed lines indicate the region where the excited quasiparticle states of the Kitaev chain are located, while the auxiliary charge site and the Majorana modes lies at zero energy, where most of the entanglement is concentrated. The parameters in the Kitaev chains are $E_c = t_0$, $t_s = 0.4E_c$, $\mu_s = -0.1E_c$, $\Delta = 0.5E_c$, and $t_c = 0.2E_c$. The current is computed in proximity of the zero-bias peak at the charge degeneracy point $n_g = 0.5$ and $V_b = 0.1E_c$.

similar to that shown in the noninteracting case, illustrated in Fig. 2, suggesting that the MPS simulation is capturing correctly the transport phenomenon. The shaded area highlights the NEQSS regime from which we extract the expectation value of the current. To compute the error, we use a standard binning technique: we divide the interval in several "batches" (or bins), each with 10–20 data points, and extract the mean and the variance of the current in each of these. Then, we average the current again and propagate the error to extract the variance of the final result. The inset shows the corresponding behavior of the charge accumulated on the device, comparing the difference between the ingoing and outgoing currents and the variation of the occupation number of the auxiliary charge site. Their agreement is a good sanity check to verify that the simulation is physically meaningful and the stationary value $\langle\hat{N}(t)\rangle - \langle\hat{N}(0)\rangle \sim 0.5$ is correctly reached. The system is initially prepared in the BCS ground state with no quasiparticle excitation ($\langle\hat{N}(0)\rangle = 0$) which is degenerate with the state with the MBS occupied (since we are deep in the topological phase); after the quench, the system approaches a NEQSS characterized by an equal superposition of the two degenerate many-body states, hence the increase of the charge (in Appendix D we present a comparison of this transient dynamics with the μ-quench protocol). Figure 5(b) shows the spread of the entanglement in the energy-ordered MPS chain: thanks to the basis choice, the entanglement is confined to low energy states. In particular, states of the Kitaev chain above the energy gap—located in the region between the two dashed vertical lines—remain almost uncorrelated with the rest of the system, signaling that transport is mediated mainly by the Majorana modes. This situation represents the ideal case of application of our method: when only a few scatterer states are involved in the transport process, while most remain untouched by the dynamics, the convergence of the simulation towards a NEQSS is robust and it is not limited by the system size.

A. SC quantum dot

A clear example of the physical results that can be explored by our approach is provided by a floating p-wave superconducting two-level system, one of the simplest SC model that displays Coulomb blockaded transport. Its small size allows for fast and accurate simulations over a wide bias range, making it easy to characterize the Coulomb blockaded differential conductance in the whole n_g-V_b plane. Indeed, the limited growth of the entanglement in this model yields that there is no need of fine tuning the simulation parameters (as the duration of the TDVP time steps or the decay length ξ) to ensure the convergence to a NEQSS.

This system is represented by the Hamiltonian:

$$\widehat{H}_{\rm sys} = \varepsilon_0 \hat{\gamma}_0^\dagger \hat{\gamma}_0 + \varepsilon_1 \hat{\gamma}_1^\dagger \hat{\gamma}_1, \tag{14}$$

where $\hat{\gamma}_{1,2}$ are the destruction operators of the quasiparticle levels.[1] Although simple, this toy model can be used as an approximation for a hybrid semiconductor/superconductor nanowire with strong spin-orbit coupling to allow for the emergence of an effective p-wave SC pairing (see, for instance, Refs. [53,54]): in this case, the lowest energy level ε_0 represents a nondegenerate subgap state (Andreev or Majorana bound state), whereas the eigenstate at $\varepsilon_1 \sim \Delta$ constitutes an effective representation of all the quasiparticle states above the SC gap. To reconstruct the Coulomb blockade diamonds, we perform the quench simulations of a grid of points in the n_g-V_b plane, with a denser sampling close to the zero-bias peak, and compute the time-dependent current averaged over the left and right contacts. Then, we follow the procedure described at the beginning of Sec. V to extract the differential conductance.

Our results show that the MPS + TDVP simulation allows to capture all the expected perturbative transport features of

[1] On a practical level, the SC quantum dot is described as a very short Kitaev chain (2) with $\mathcal{M} = 2$ sites only.

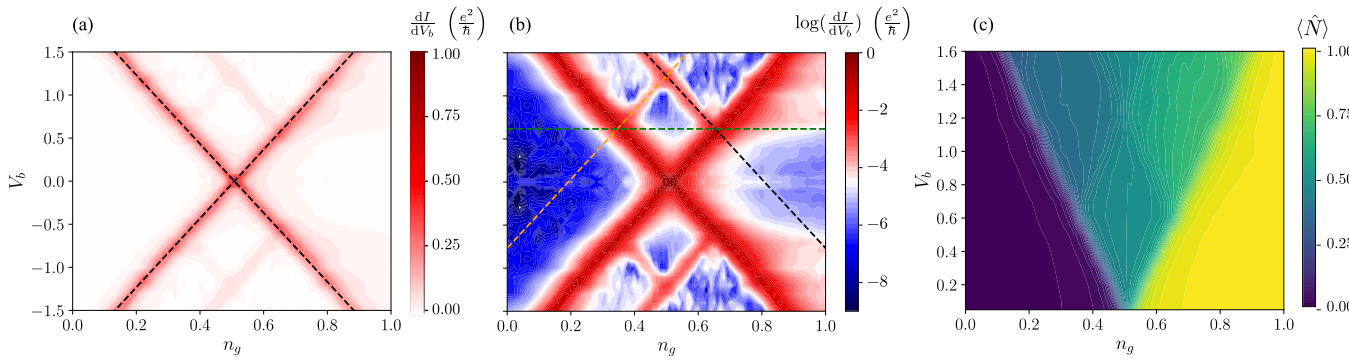

FIG. 6. (a) Differential conductance close to a charge degeneracy point in the n_g-V_b plane, for a two level SC systems with $\varepsilon_0 = 0.02E_c$, $\varepsilon_1 = 0.6E_c$, and $t_c = 0.2E_c$. Transport is dominated by the sequential tunneling resonances (black dashed lines), corresponding to $V_b/2 = \pm[E_c(1-2n_g)+\varepsilon_0]$. (b) Differential conductance in log-scale, illustrating the cotunneling step in the odd Coulomb valley that arises at $V_b \sim \pm(\varepsilon_1 - \varepsilon_0)$ (green dashed line). Also the transitions involving excited states are more visible: $V_b/2 = [E_c(1-2n_g)+\varepsilon_1]$ (black dashed line) and $V_b/2 = [E_c(2n_g-1)+\varepsilon_1]$ (orange dashed line). (c) Average charge in the NEQSS of the SC quantum dot, for positive bias. Notice how the sequential tunneling resonances are reflected in the structure of $\langle\widehat{N}\rangle$.

these SC blockaded systems, including both sequential tunneling resonances and inelastic cotunelling effects at finite bias. In particular, Fig. 6(a) illustrates the differential conductance in the n_g-V_b plane for a quantum dot with $\varepsilon_0 = 0.02E_c$ and $\varepsilon_1 = 0.6E_c$. The charging energy is the dominant energy scale, alongside the "bare" hopping amplitude in the leads $t_0 = E_c$, while the tunnel coupling between the leads and the system is $t_c = 0.2E_c$.

The first feature emerging in the differential conductance is the appearance of resonances caused by the incoherent sequential tunneling mediated by the low energy state ε_0. These bright conductance resonances are clearly visible [indicated by black dashed lines in Fig. 6(a) and appear when the voltage bias matches the energy difference between the ground states in the even and odd sectors $V_b/2 = \pm E_c(1-2n_g)+\varepsilon_0$. Sequential tunneling is indeed the main transport mechanism emerging in the perturbative rate equation approaches and the related conductance peaks are commonly observed in superconducting blockaded devices; see, for instance, the experimental data referring to SC islands in nanowires in Refs. [53–56] and the theoretical analysis in [36,57].

The sequential tunneling mediated by the state ε_0 is not the only perturbative feature that characterizes the intermediate t_c regime we are exploring. In Fig. 6(b), we report the same data in the logarithmic scale, where a richer structure emerges more clearly. One can indeed observe the fainter resonances corresponding to sequential tunneling processes involving the high-energy quasiparticle level ε_1 (orange and black dashed lines).

Interestingly, besides these sequential tunneling features, which correspond to first-order phenomena in the tunnel coupling t_c, we can clearly spot cotunelling effects, related instead to second-order phenomena in t_c. The main cotunelling feature is the appearance of an even-odd effect that distinguishes Coulomb diamonds with different parities of the particle number $\widehat{N}$ [36,54]. In particular, the finite-bias conductance in the Coulomb valleys with odd particle number [$n_g > 0.5$ in Fig. 6(b)] displays an inelastic cotunneling step visible for $V_b \sim \varepsilon_1 - \varepsilon_0$ (green dashed line). The lack of appreciable cotunneling in the even valley is due to the destructive interference between the possible cotunneling paths when the ground state has even parity, while the interference becomes constructive in the odd valley. Indeed, with our method we simulate the coherent evolution of a closed quantum systems, where interference effects can play a dominant role. In their absence, cotunneling steps would appear also in the even valley; in particular, when the lowest quasiparticle state has an energy $\varepsilon_0 \ll E_c,\ \Delta_{\rm SC}$, the conductance predicted by rate equations in the even and the odd valley would be almost identical.

Finally, in Fig. 6(c), we report the average occupation number $\langle\widehat{N}\rangle$ of the auxiliary site that describes the total charge of the device. In the simulation we set the charge truncation at $N_{\rm max} = 5$. This truncation has very little effect on the simulations since in the steady state the average charge acquires values between 0 and 1, for $n_g \in [0, 1)$, while the occupation of the states at the cutoff $\widehat{N} = N_{\rm max}$ lies below numerical precision. From the figure, it is clear that, when transport is suppressed, the SC island has a well defined integer charge determined by n_g [blue and yellow areas in Fig. 6(c)]. When transport is present, instead, the device is in a mixed state resulting in an average charge $\langle\widehat{N}\rangle \sim 0.5$, with a series of plateaus delimited by the sequential tunneling resonances.

Despite the fact that both sequential tunneling and inelastic cotunneling features are evident in our simulations, we cannot expect a quantitative agreement on the amplitude of the differential conductance peaks between our nonperturbative simulations and the perturbative rate equation techniques. There are indeed two aspects to be emphasized. First, our MPS calculations simulate the unitary evolution of a closed system at zero temperature, whereas rate equations only describe the noncoherent evolution of the populations of the scatterer many-body states. Therefore the MPS + TDVP method captures interference effects between transport channels in higher-order processes such as cotunneling, as mentioned before, while rate equations do not. Second, rate equations are rigorously justified only when the temperature is larger than the tunnel coupling t_c and mainly describe temperature-broadened conductance peaks (see Appendix C). In this respect, the tunneling strength we used for most of

the simulations, $t_c = 0.2E_c$, is definitely beyond their range of validity.

Finally, we remark that the MPS approach is able to capture also nonperturbative effects. In this respect, we observe that a faint zero-bias peak is visible in Fig. 6(b) for $0.5 < n_g < 0.9$, thus in the odd diamond. Its appearance suggests the onset of a weak nonperturbative Kondo-like effect which cannot be captured by rate equations.

Therefore our technique provides a method which is complementary to the standard rate equation approach: the MPS + TDVP simulations allow for the investigation of transport in the low-temperature and strong coupling regime, which is typically hard to tackle with traditional techniques. For small tunneling rates and higher temperatures, instead, transport is dominated by perturbative phenomena which can be efficiently captured by rate equations.

B. Coulomb blockaded Kitaev chain

We now analyze the quantum transport across a Kitaev chain in the topological phase and characterize the zero-bias peak of the differential conductance and its dependence on the voltage bias at the charge degeneracy point. By simulating the dynamics of a chain with $\mathcal{M} = 40$ sites, we show that our method correctly captures the low-bias transport mediated by the Majorana modes. At small voltage bias we observe nonperturbative effects such as the quantization of the conductance at the charge degeneracy point $n_g = 0.5$, for symmetric left and right tunnel coupling t_c. Moreover, the analysis of the stationary current as a function of t_c shows that we can investigate the dynamics of large systems in a strong coupling regime, beyond the validity of both first-order rate equations and single resonant level [36] approaches. To characterize the current dependence of the voltage bias at $n_g = 0.5$, we focus, instead, on a shorter chain; even though we can study much longer *gapped* systems at *small biases*, we chose $\mathcal{M} = 8$ because the simulations with a considerably larger number of quasiparticle states and large biases are subject to a fast entanglement growth and their correlations rapidly saturate the maximum bond dimension we set.

The most characteristic feature of Coulomb blockaded transport is the zero-bias peak that appears at the charge degeneracy point. Its presence is easily understood by a first order rate equation approach (see Appendix C): when the energy of the BCS ground state with even fermionic parity—i.e., no quasiparticle (QP)—matches the energy of the ground state with odd parity—thus with the lowest lying QP state occupied—electrons can tunnel into and out the SC device without paying energy. In the presence of Majorana zero-energy modes, however, this process results in a coherent teleportation of electrons between the two leads mediated by the MBS [58,59]. Therefore, in the limit of large energy separation between the zero-energy MBS and the other QP states, the zero-bias conductance peak can be estimated based on a nonperturbative Breit-Wigner (BW) formula for resonant tunneling mediated by the Majorana modes [36]. Indeed, if we consider a single resonant fermionic level, the differential conductance close to the charge degeneracy point $n_g = 0.5$ is approximated by

$$G_{BW}(\omega) = \frac{e^2}{h}\frac{\Gamma_L\Gamma_R}{(\omega - E_c(1-2n_g))^2 + (\Gamma_L+\Gamma_R)^2/4}, \quad (15)$$

where $\Gamma_\alpha = t_{c,\alpha}^2|u_\alpha|^2/t_0$ is the effective tunnel rate that takes into account the local density of states $\nu = (2\pi t_0)^{-1}$ of the leads with open boundary conditions at the Fermi energy and the projection of the particle-like component of the resonant level on the device edges, u_α. ω is the energy at which the conductance is probed. G_{BW} neglects the transport effect of QP states above the SC gap and results in the quantization of the differential conductance peaks at zero bias ($\omega = 0$) for symmetric rates $\Gamma_R = \Gamma_L$. From now on, we will focus on the symmetric coupling and denote the effective tunneling rare with Γ.

From Eq. (15) it is straightforward to obtain the current at finite voltage V_b. By integrating the conductance between $\omega = -V_b/2$ and $\omega = V_b/2$, we obtain

$$I(V) = \Gamma\Big[\arctan\Big(\frac{V_b - 2E_c(1-2n_g)}{2\Gamma}\Big) + \arctan\Big(\frac{V_b + 2E_c(1-2n_g)}{2\Gamma}\Big)\Big]. \quad (16)$$

An important observation is that Γ sets both the amplitude of the current and the width of the linear response regime where the conductance is quantized at $n_g = 0.5$.[2]

In the following, we compare our numerical results with this BW theoretical prediction. In analogy with Eqs. (15) and (16), also the MPS simulations are not perturbative in the tunnel coupling t_c; at the same time, they provide a more complete description than the BW formula because they take into account the presence of multiple energy levels above the SC gap.

In Fig. 7(a), we show the current at small bias $V_b = 0.1E_c$ for several values of t_c and compare our numerical results with the values predicted by Eq. (16) (solid black lines). We observe and excellent agreement between the two approaches for small tunneling strengths while their discrepancy increases as t_c becomes larger. Indeed, in the strong coupling regime, the MPS simulations predict a larger current than the BW approximation, in particular in the odd valley $n_g > 0.5$. Indeed, the population of quasiparticles above the superconducting gap is no longer negligible for $t_c = 0.4E_c = 0.8\Delta_{SC}$, where Δ_{SC} is the energy separation between the Majorana bound states and the higher excited states. Hence, the single resonant level approximation behind Eqs. (15) and (16) is no longer valid, as more transport channels become available.

We further emphasize that V_b is too large to observe the quantization of the conductance (for $\Gamma_L = \Gamma_R$) in the linear response regime $I = \frac{e^2}{h}V_b$, indicated by the horizontal dot-dashed line in Fig. 7(a). To observe such quantization, it is necessary to measure the current at smaller voltage biases, such that $V_b \lesssim \Gamma$. In this regime, a fourth-order finite differences approach to estimate $G = dI/dV_b$ gives results

[2]Linear response holds when the Taylor expansion of the arctan functions can be trunctaed at linear order. For $n_g = 0.5$, that requires $2\Gamma \gg V_b$.

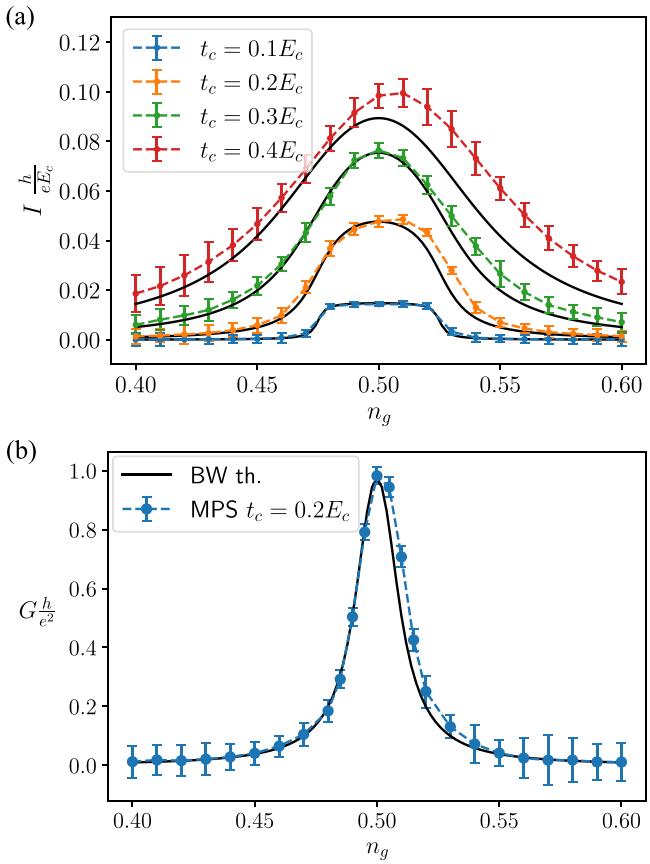

FIG. 7. (a) Comparison between the steady state current obtained with the MPS simulations and Eq. (16) (solid black lines) for several values of the tunnel coupling t_c. The current is computed at small but finite bias $V_b = 0.1E_c$. The horizontal dot-dashed line indicates the value of the current for a quantized conductance $G = e^2/h$. (b) Zero-bias conductance peak obtained with foruth-order method with finite differences, extracted from current signals at $V_b = 0.02E_c$ and $V_b = 0.04E_c$. The solid black lines is the theoretical prediction from Eq. (15). The other physical parameters are $\Delta = t_s = 0.3E_c$, $\mu_s = -0.1E_c$, $E_c = t_0$, and $\mathcal{M} = 40$.

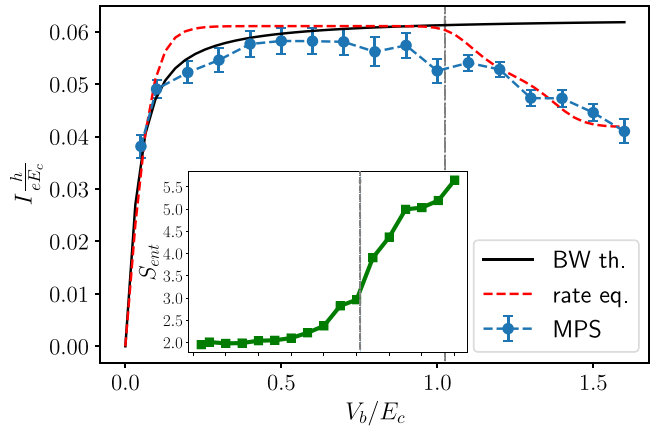

FIG. 8. Current vs voltage bias in correspondence of the induced charge resonance $n_g = 0.5$ for a Kitaev chain with $\mathcal{M} = 8$ sites; the vertical dashed line indicates the energy corresponding to the superconducting gap. The overall scale of the rate equation current (dashed red line) has been arbitrary chosen to approximately match that of the TDVP algorithm. The solid black line is Eq. (16). The inset shows the maximum entanglement entropy in the chain reached as a function of V_b. Again, the vertical dashed line indicates the position of the SC gap, where we observe a fast increase of the entanglement. For the largest two values of V_b considered, the estimate of S_{ent} is no longer reliable because the simulation saturates the maximum bond dimension allowed and the error introduced in the SVD truncation becomes larger than the chosen cutoff of 10^{-7}.

in agreement with the theoretical prediction of Eq. (15), as show in Fig. 7(b): at $n_g = 0.5$, the conductance is quantized $G = e^2/h$ within one errorbar. The numerical data show also a slight asymmetry of the conductance peak, as already observed in Fig. 7(a). This effect seems analogous to the case of the superconducting quantum dot in Fig. 6(b), and can be qualitatively understood based on different amplitudes of cotunneling processes in the even and odd Coulomb valleys.

By recovering the quantization of the zero-bias peak, we have shown that our numerical method can describe nonperturbative effects as well as transport in a strong coupling regime, going beyond single-level approximation for resonant tunneling. A further facet of the complementarity between our zero-temperature simulations and the perturbative rate equation calculations is provided by the behavior of the tails of the peak as a function of the induced charge: rate equations result in a temperature-broadening of the conductance peak with exponentially suppressed tails, whereas our approach describes a broadening induced by the tunneling amplitude, which is instead characterized by a power law decay far from $n_g = 0.5$.

The next step towards the full characterization of the conductance in the n_g-V_b plane is the analysis of the current with respect to the voltage bias. As mentioned above, here we restrict our simulations to $\mathcal{M} = 8$ sites in the scatter to reduce the entanglement growth when V_b becomes larger than the superconducting gap. Our results are reported in Fig. 8, where we plot the current flowing through the Kitaev chain as a function of the voltage difference between the leads, in correspondence to the resonance $n_g = 0.5$. Since we expect single-electron processes to be dominant at the charge degeneracy point, we compare our data with the prediction of first order rate equations (dashed red line), which indeed give a qualitative agreement. However, it must be noticed that both the overall amplitude of the current obtained with rate equations, and the temperature used in the corresponding Fermi factors have been arbitrary set to approximately match the profile given by the MPS data (see Appendix C for more detail). We also consider the comparison with the BW approximation in Eq. (16) (solid black line).

As expected, the current increases sharply at small values of V_b (the zero-bias peak) and then saturates in the region where transport is mostly mediated by the Majorana edge modes while the voltage is too small to excite states above the SC gap, indicated by the vertical dashed line. In this regime, the Eq. (16) is a valid approximation for finite bias transport, as observed from its good agreement with the MPS simulations. When $V_b > \Delta_{\text{SC}} \sim 0.5E_c$, the current decreases because transport across excited states is less efficient with respect to the Majorana modes, due to the reduced projection on the device edges. From the point of view the differential conductance, this appears as a region with negative G, as

observed in several experiments on SC devices with subgap states [53,56]. In this regime, multiple quasiparticle states are involved in transport processes and, therefore, the BW approximation is no longer valid, while the first-order rate equations method allows us to capture the qualitative features of the I-V curve.

An important effect of the excited states is the abrupt increase of the entanglement entropy at the central bond when V_b exceeds the SC gap, as reported in the inset of Fig. 8. Indeed when the voltage is large enough for multiple quasiparticle states to become populated, the entanglement grows accordingly. When the bias is smaller than $\sim 0.7E_c$, the simulations are accurate (truncation error below 10^{-7}). When the bias becomes large, $V_b/2 \gtrsim 0.7E_c$, the system progressively saturates the maximum entanglement allowed by our simulations, which is set by the maximal bond dimension $\chi_{\max} = 2500$, and the errors of our simulations are no longer under control.

This constitutes the principal limitation of our method: when a continuous spectrum or a large number of excited states are within the bias energy window, thus having significant contribution to the transport of electrons, the entanglement will grow rapidly with time, hence requiring more computational resources for the accurate simulation of the dynamics, in line with general limitations of tensor network methods for studying quantum quenches. There are several strategies to fine tune the simulations parameter and mitigate these limitations, such as choosing optimal time step durations and adjusting the localization length ξ in the leads. The best choice depends, however, on the physical parameters of the model and needs to be set accordingly.

The entanglement entropy at each link is therefore a useful quantity to monitor because it determines whether the simulation succeeds or not: if the entanglement entropy grows too much, so does the bond dimension χ needed to describe faithfully the quench dynamics. χ, in turn, is constrained by the memory and computational time allocated for the calculation. On a practical level, we need to ensure that the maximum bond dimension $\chi_{\max}$ allowed is large enough to observe the emergence of a stationary value for the current.

Figure 9(a) shows the increase in time of the entanglement entropy S_{ent} corresponding to partitions of the tensor network at three different positions and for several lengths of the scatterer (color-coded). Solid lines correspond to a cut at the position of the charge site, which lies at the center of the MPS. Dashed and dot-dashed lines instead correspond to cuts in the middle of the leads bandwidth, at negative and positive energies, respectively. The simulations are performed at the charge degeneracy point $n_g = 0.5$ with a small bias $V_b = 0.1E_c$. Notice that the entanglement entropy at the auxiliary charge site position, where the entropy is the largest, is almost independent from the length of the scattering region $\mathcal{M}$. Hence, in the regime where a single state mediates transport, the efficiency and speed of the simulations depend very weakly on the number of single-particle states in the SC device, allowing for studying relatively large systems.

In Fig. 9(b), we plot the entanglement entropy profile as a function of the energy of the MPS sites, at the end of the time evolution. Different curves refer to different values of V_b, corresponding to the data presented in Fig. 8, where larger voltage biases induce larger entanglement and also a wider

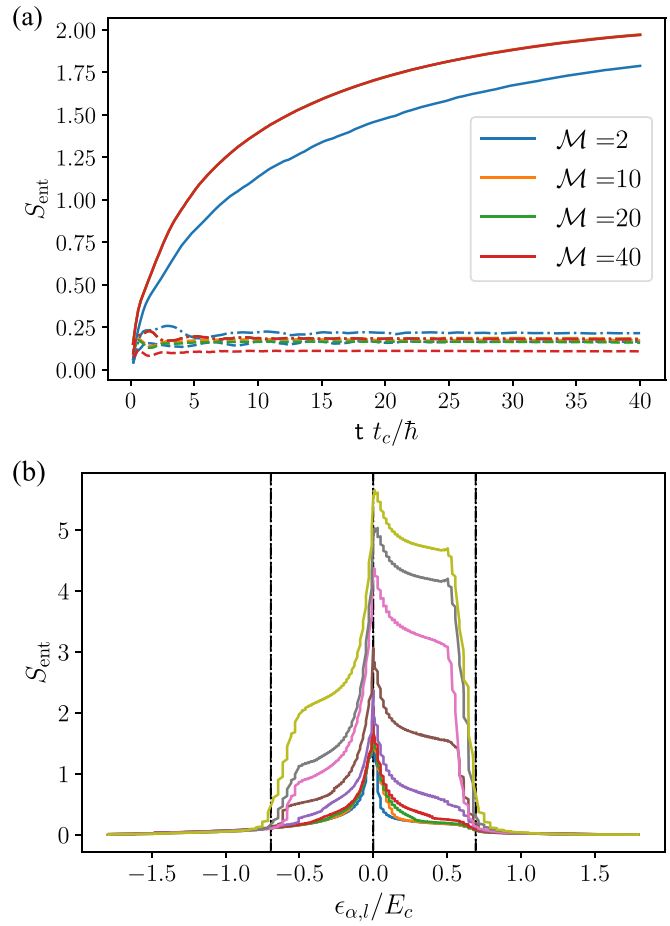

FIG. 9. (a) increase of S_{ent} in time for cuts in three different positions: auxiliary charge site (solid lines), right left lead bulk (dashed lines), and right lead bulk (dot-dashed lines). The color encodes the size of the scatterer; Notice that the curves corresponding to the entropy at the charge site (solid curves) are perfectly superimposed for $\mathcal{M} > 2$, indicating that S_{ent} is almost independent from $\mathcal{M}$ as long as transport is dominated by a single channel. The voltage bias is $V_b = 0.1E_c$. (b) entropy profile of S_{ent} at the end of the time evolution, for different values of the $V_b \in [0.1E_c, 1.6E_c]$. Larger entropy is associated to larger biases. The vertical dashed lines indicate the energy range of the possible manybody transitions of the scatterer, where the total charge changes by 1. This interval is centered around 0 because the data are taken at the charge degeneracy point $n_g = 0.5$. The other parameters in the Kitaev chains are $\Delta = t_s = 0.3E_c$, $\mu_s = -0.1E_c$, and $t_c = 0.2E_c$.

region of the MPS where S_{ent} grows. Notice, however, that the entanglement is mostly restricted to energies limited by the bandwidth of the scattering device, indicated by the vertical dashed lines.

These data make clear the advantage deriving from our basis choice: the entanglement grows logarithmically in time and is concentrated in an energy window limited by the minimum between V_b and the bandwidth of the scatterer. The "bulk" of the leads, meaning states far in energy from the Fermi level, almost remains in its initial product state, as seen also from Fig. 3. The logarithmic growth of the entanglement entropy implies that the bond dimension grows linearly in time, making the simulation efficient, since the resources required

increase at most as a power law of the system size and the total evolution time. However, the situation is not always so favorable: in general, the larger the current, the faster the entanglement and bond dimension grow.

VI. CONCLUSIONS

In this paper, we illustrated an efficient method to simulate transport phenomena in Coulomb blockaded one-dimensional superconducting systems, which encompass several fundamental building blocks for the realization of both SC qubits and many proposed platform for topologically protected qubits. We extract their differential conductance from the quasi-steady state current arising after a quantum quench in which we bring the system out of equilibrium by imposing a finite voltage bias between two leads connected to it.

Our method allows for exploring the system behavior in the strong coupling regime between the leads and the interacting SC device and for describing results beyond perturbative approaches (for instance, standard rate equation approaches). It is therefore suited for the study of nonperturbative phenomena such as Kondo or topological Kondo effects.

We simulate the real-time system dynamics within the MPS framework, where each site represent a single-particle energy eigenstate and the charging energy is encoded in an auxiliary site describing the total charge of the scattering region. In this basis, the system entanglement remains localized [22] an we are able to compute efficiently the time evolution for long times.

In this paper, we focused on simple p-wave superconducting spinless models and noninteracting leads; in particular, we analyzed two physical examples: a superconducting dot with two quasiparticle states and a blockaded Kitaev chain. Concerning the former, our method reproduces the predicted sequential tunneling and cotunneling signatures and accounts for the interference between different coherent transport processes. Concerning the latter, our method recovers the quantization of the conductance peak predicted in the case of symmetric left and right tunneling rates for low t_c, and evidences a typical asymmetry of the zero-bias peak caused by the quasiparticle states above the superconducting gap in the strong coupling regime. Therefore it gives a more complete description of the transport process than the resonant level approximation and provides a complementary approach to perturbative rate equations.

Our method can be easily extended to take into account more leads, additional interactions, the presence of disorder or smooth potential profiles in the scatterer and spinful systems. A weak Josephson coupling between the superconducting scatterer and grounded superconductors can also be efficiently described, as well as interacting or more complex leads. Furthermore, several recent works applied MPS methods to describe the time evolution after a quantum quench and the transport in interacting systems with leads of infinite length [52,60–62]. Such techniques can be integrated in our approach and can provide a method, alternative to the Wilson chain description, to mitigate finite size effects.

Our results to estimate the system conductance can also be integrated with recently developed techniques to simulate a dissipative time evolution of the system based on suitable Lindblad operators [6,63,64]. Indeed, our simulations focused on the unitary evolution of closed systems. However, the description we have chosen for the leads degrees of freedom can be extended to account for the coupling with external electronic reservoirs, as well as other thermodynamic baths imposing a dissipative dynamics to the system. Furthermore, the introduction of suitably tailored dissipative terms that decrease the weight of nonlocal operators in the MPS time evolution has been proven beneficial to reduce the increase of the system entanglement in diffusive systems [65]; such technique could be implemented also in our TDVP evolution, thus allowing for longer simulation times.

Adding the possibility of simulating the quench dynamics at finite temperature is also a necessary step to observe some of the scaling properties associated to topological [66–74] or charge Kondo effects [75–77]. A possible route to include a finite temperature within the tensor network framework, is to promote the system wavefunction to a density matrix, encoded in a matrix product operator (MPO), which can describe both a pure and an open mixed state [78,79]. Alternatively, one can keep a pure state description of the system, thus maintaining its MPS structure, by exploiting a *thermofield* transformation [21,24,80], where the thermal distribution in the leads is reached by tracing out a set of auxiliary sites.

ACKNOWLEDGMENTS

We warmly thank K. Flensberg, M. Leijnse, J. Paaske, R. Seoane Souto, and Mingru Yang for useful discussions. This project is supported by the Villum Foundation (Research Grant No. 25310) and received funding from the European Union's Horizon 2020 research and innovation program under the Marie Sklodowska-Curie Grant Agreement No. 847523 "INTERACTIONS." C.-M.C. acknowledges the support by the Ministry of Science and Technology (MOST) under Grant No. 111-2112-M-110-006-MY3, and by the Yushan Young Scholar Program under the Ministry of Education (MOE) in Taiwan.

APPENDIX A: DETAILS ON THE MPS CONSTRUCTION

1. Josephson energy and inclusion of a superconducting lead

In the main text, we discussed systems in which the scatterer exchanges particles with the leads only. The introduction of the auxiliary site, however, allows us to to extend further our model in order to effectively account for an additional SC lead, which exchanges Cooper pairs with the SC scatterer. This is possible by replacing the Hamiltonian $\widehat{H}_c$ with a more general form:

$$\widehat{H}_{\mathrm{SC\,box}} = E_c(\widehat{N} - n_g)^2 - E_J[(\widehat{\Sigma}^+)^2 + (\widehat{\Sigma}^-)^2]. \tag{A1}$$

This constitutes the Hamiltonian of a Cooper pair box [81], and the energy scale E_J represents its Josephson energy. The second term in Eq. (A1) varies the number of electrons in the scatterer by ± 2 [see Eq. (11)] and indeed represents a process in which Cooper pairs tunnel in and out of the system. Given the limitation provided by the truncation $N_{\max}$, the simulation of the system is reliable only when E_J is sufficiently smaller than E_c, such that, in practice, the states $|\pm N_{\max}\rangle$ display a negligible population. Therefore the extension of the original

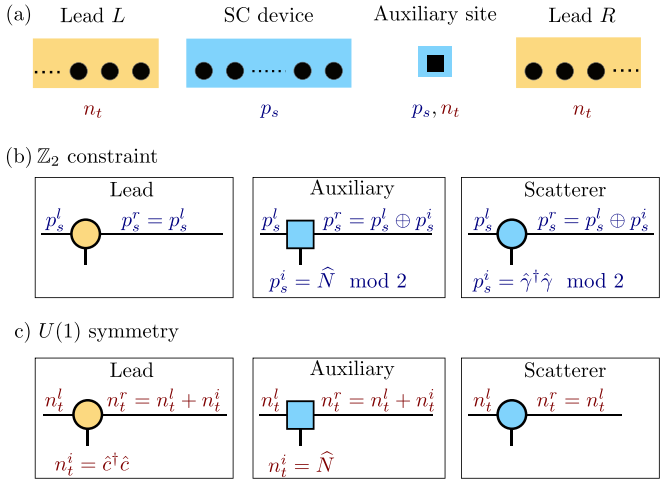

FIG. 10. (a) The quantum numbers p_s and n_t refer to the fermionic parity of the scatterer and the total particle number respectively. The scheme indicates for which kind of sites in the MPS these quantum numbers are defined. (b) The $\mathbb{Z}_2$ parity constraint (9) is imposed by building tensors fulfilling the depicted rules. The lead tensors connect virtual states with the same parity. The auxiliary and scatterer sites, instead, modify the fermionic parity of the virtual states accordingly to the physical degree of freedom, such that they are $\mathbb{Z}_2$ invariant. (c) The global U(1) gauge invariance is enforced by assigning to each virtual link in the MPS chain a virtual charge n_t. For the auxiliary and lead sites, the tensors increase the virtual charge based on the charge of the physical state n_t^i. The scatterer sites, instead, leave the virtual charge unaltered.

model provided by Eq. (A1) is suitable to describe scatterers which are typically in a Coulomb-dominated regime, as in the case of SC charge qubits. The opposite transmon limit $E_J > E_c$, instead, cannot be satisfactorily explored.

When replacing $\widehat{H}_c$ with $\widehat{H}_{\text{SC box}}$, the conservation of total particle numbers (in the leads and the scatterer) is reduced to the conservation of parity, which may assume both values depending on the initial lead states.

By including the Josephson energy, the model becomes effectively a three-terminal device, able to simulate the interacting Coulomb blockaded regime of systems analogous to the ones studied in Refs. [82,83]. We also observe that, by switching off the tunnel coupling with one lead, it is possible to study two-terminal normal-superconducting junctions mediated by a blockaded scatterer described by $\widehat{H}_{\text{sys}}$.

2. Symmetry

Our MPS construction, represented in Fig. 1, exactly implements the parity constraint given by Eqs. (8) and (9) and the U(1) global symmetry associated to the conservation of the charge in Eq. (10). These are two independent symmetry conditions which the MPS construction must fulfill, and we emphasize that the first involve only the physical degrees of freedom of the scatterer and the auxiliary state, whereas the second involves only the physical degrees of freedom of the leads and the auxiliary site. The tensors entering the description of the system must accordingly fulfill the $\mathbb{Z}_2$ and U(1) charge conservation rules represented in Fig. 10, which involve both the physical and virtual indices (see Refs. [8,84,85] for general overviews of symmetries in tensor networks). These requirements are set by assigning two independent quantum numbers, which we label by p_s and n_t and correspond to the scatterer fermionic parity and the total particle number, to all the states in each (virtual or physical) bond of the MPS.

Figure 10(a) summarizes which kind of physical sites contribute to the quantum numbers p_s and n_t of the MPS tensors. The quantum number $p_s = 0, 1$ concerns the $\mathbb{Z}_2$ fermionic parity of the scatterer degrees of freedom. In particular, p_s on the bond l refers to the fermionic parity accumulated in the scatterer physical sites (including the auxiliary charge site) on the MPS sites before the bond l. In Fig. 10(b), $p_s^{l/r}$ labels left and right virtual states of the tensors respectively; p_s^i refers instead to the fermionic parity of the physical sites of the scatterer. In order for the constraint (9) to be satisfied, the lead tensors must connect left and right virtual states with the same parity p_s, irrespective of the lead physical degree of freedom [since Eq. (9) does not involve them]; the auxiliary and scatterer site tensors, instead, must connect virtual left and right states with different parity whenever the physical fermionic parity of the site is odd, and leave the virtual parity p_s invariant when the physical parity is even. This corresponds to the conservation of the fermionic parity p_s depicted in Fig. 10(b). The constraint (9) is enforced by a suitable choice of the tensor boundary conditions.

Concerning the global U(1) charge conservation, instead, the physical degrees of freedom involved are the ones of the leads and the auxiliary site. Such charge conservation is imposed by assigning a further charge quantum number n_t to all states in the MPS bonds. In this case, the lead and auxiliary site tensors must suitably increase this virtual charge from the left to the right tensor link based on the charge of the physical site. The scatterer site tensors, instead, connect virtual states with the same virtual charge. See Fig. 10(c).

We emphasize that p_s must not be confused with the parity of n_t. Clearly, since Eq. (10) sets a U(1) symmetry of the system, it also enforces an additional parity conservation for the lead and auxiliary site degree of freedom, which corresponds the $\mathbb{Z}_2$ symmetry that characterizes the system when introducing the additional Josephson coupling E_J in Eq. (A1). In this case, the constraints in Fig. 10(c) are relaxed to analogous relations involving only the new parity $q_t = n_t \mod 2$.

APPENDIX B: ENERGY BASIS AND ENTANGLEMENT GROWTH

In this section, we briefly review the entanglement growth with real-time dynamics in the real-space and the energy bases.

The growth of entanglement is the main challenge in the MPS simulations, which typically prevents the possibility of reaching an accurate description of the system dynamics for long times [50]. This is clearly a major limitation, since the estimate of the conductance of a given scatterer is based on the NEQSS behavior of the current. When considering an MPS based on a real space basis, the entanglement growth is captured by the entanglement entropy S associated to any

partition that separates the degrees of freedom in different leads. Each particle coming from the leads is partially reflected and partially transmitted in a coherent way by the scatterer, generating entangled particle-hole pairs [22,23]. This results in a linear increment of $S \propto V_b t$ in time and voltage bias, which is consistent with the Lieb-Robinson picture of the dynamics of the system after a quench: the NEQSS appearing inside its space-time cone is constituted by a number of particle-hole pairs that increases linearly in time.

To mitigate the restrictions imposed by this growth of the entanglement, Rams and Zwolak proposed to adopt a different basis [22]: when the leads are modeled based on an ordered single-particle energy eigenbasis, only states lying in an intermediate energy window defined by the voltage bias are affected in a major way by the time evolution. By modeling a system with a mixed eigenbasis—an energy eigenbasis for the leads and a spacial basis for the scatterer—the entanglement entropy typically displays only a logarithmic growth in time [22], thus allowing for simulations of a considerably longer time evolution (see also Ref. [86]).

APPENDIX C: RATE EQUATION APPROACH

To compare our numerical results with an analytical approach, we use a standard rate equation approach, where we consider a classical probability distribution for the occupation numbers of the quasiparticle (QP) states in the scatterer and transition rates given by Fermi golden rule.

First, let us rewrite the Hamiltonians of the quantum dot:

$$\widehat{H}_{\rm sys} = \sum_{n=1}^{N} \epsilon_n \hat{\gamma}_n^\dagger \hat{\gamma}_n + \mathcal{E}_0 + E_c (N - n_g)^2, \tag{C1}$$

where $\mathcal{E}_0$ is the energy of the BdG vacuum and $\hat{\gamma}_n$ is the destruction operator of the quasiparticle state with positive energy ϵ_n.

Regarding the leads, we make a wide-band approximation, with a linear dispersion and a constant density of states

$$\widehat{H}_{\rm leads} = \sum_{\alpha=R,L} \sum_k \xi_{\alpha,k} \hat{c}_{\alpha,k}^\dagger \hat{c}_{\alpha,k}, \tag{C2}$$

where we assume that the eigenstates are plane waves with momentum quantization $k = \frac{2\pi}{L} j$, with j integer. To link this approximation with the original tight binding description we fix $\xi_{\alpha,k} = \hbar v_\alpha^F k - \mu_\alpha = 2t_0^\alpha k a - \mu_\alpha$, being $2t_0^\alpha a/\hbar$ the lead Fermi velocity at half filling and a the lattice spacing.

Finally, the tunneling Hamiltonian between lead α and the SC device reads

$$\widehat{H}_{\rm tunn}^\alpha = -t_{c,\alpha} \sum_{k,n} [(\hat{\gamma}_n^\dagger u_n^*(x_\alpha) + \hat{\gamma}_n v_n(x_\alpha)) \hat{c}_k \phi_{\alpha,k} + \text{H.c.}]. \tag{C3}$$

Here, $u_n^*(x_\alpha)$ and $v_n(x_\alpha)$ are the particle and hole weights, respectively, of the $n-$ th eigenstate on the first ($x_L = 1$) or last ($x_R = N$) site of the chain, while $\phi_{\alpha,k}$ are the plane waves states of the leads.

Since we are interested in a strong Coulomb blockaded regime, we restrict the scatterer Hilbert space considering only states with total charge $N = 0, 2$, with no QP excitation, and $N = 1$, with a single QP state occupied. We will denote with P_0, P_2, and P_n the populations of such states.

Sequential tunneling events connect states with different quasiparticle occupation. hence we need to compute the four transition rates Γ_{0n}^α, Γ_{n0}^α, Γ_{2n}^α, Γ_{n2}^α for both contacts with the external leads. Following Fermi golden rules, we can compute these rates as

$$\Gamma_{if} = \frac{2\pi}{\hbar} |\langle f | \widehat{H}_{\rm tunn} | i \rangle|^2 w_i \delta(E_i - E_f), \tag{C4}$$

where $|i\rangle$ and $|f\rangle$ are the initial and final states and w_i the thermal weight of the initial states. Standard calculations lead to

$$\begin{aligned}
\Gamma_{0n}^\alpha &= \frac{\pi}{h} \frac{t_{c,\alpha}^2}{t_0} |u_n(x_\alpha)|^2 f(\Delta E_{10} + \epsilon_n - \mu_\alpha), \\
\Gamma_{n0}^\alpha &= \frac{\pi}{h} \frac{t_{c,\alpha}^2}{t_0} |u_n(x_\alpha)|^2 [1 - f(\Delta E_{10} + \epsilon_n - \mu_\alpha)], \\
\Gamma_{2n}^\alpha &= \frac{\pi}{h} \frac{t_{c,\alpha}^2}{t_0} |v_n(x_\alpha)|^2 [1 - f(\Delta E_{21} - \epsilon_n - \mu_\alpha)], \\
\Gamma_{n2}^\alpha &= \frac{\pi}{h} \frac{t_{c,\alpha}^2}{t_0} |v_n(x_\alpha)|^2 f(\Delta E_{21} - \epsilon_n - \mu_\alpha).
\end{aligned} \tag{C5}$$

$\Delta E_{N,N'}$ is the charging energy difference between two states with different total charge and $f(\cdot)$ is the Fermi distribution. Once the rates are known, we can derive the nonequilibrium steady state by looking for the kernel of the transition matrix obtained from the rates in Eq. (C5).

An important thing to notice is the asymmetry between the transition $0 \leftrightarrow n$ and $2 \leftrightarrow n$. Indeed, in the first, a particle is directly transferred from the leads to a quasiparticle state, or vice-versa, while, in the second, the process involves the destruction (creation) of a Cooper pair. If the particle and hole weights happen to be very different, for instance, in a Kitaev chain in the topologically trivial phase, this asymmetry is reflected in the Coulomb diamonds. Indeed, the current associated to direct tunneling of an electron in a quasiparticle state would be much larger than the current associated to process involving a destruction or creation of a Cooper pair.

Once the rates are computed, the stationary probability distribution for the states of the SC island $P^{\rm eq}$ are found by solving the linear system of equations

$$\begin{aligned}
\sum_n \Gamma_{n0} P_n^{\rm eq} - \Gamma_{0n} P_0^{\rm eq} = 0, \\
\Gamma_{0n} P_0^{\rm eq} + \Gamma_{2n} P_2^{\rm eq} - (\Gamma_{n0} + \Gamma_{n2}) P_n^{\rm eq} = 0, \\
\sum_n \Gamma_{n2} P_n^{\rm eq} - \Gamma_{2n} P_2^{\rm eq} = 0,
\end{aligned} \tag{C6}$$

where $\Gamma_{n0} = \Gamma_{n0}^L + \Gamma_{n0}^R$ and similarly for the other rates. Notice that Eq. (C6) only considers states with one or no QP state occupied, which is valid only at small voltage bias. In order to obtain a more accurate description and take into account also transitions between excited states, situations in which tow or more quasiparticle are present should also be considered. This has been done, for instance, to obtain all the main sequential tunneling resonances appearing as diagonal lines in Fig. 6(b). Such extensions of the considered many-states involved in the

transport, however, rapidly increase the dimension and the complexity of the transfer matrix describing the incoherent evolution of the scatterer, making it intractable for systems with more than a few sites, despite they do not complicate the calculation of the rates themselves.

Combining the definition of the transition rates in Eq. (C5) and the associated probability distribution from Eq. (C6), the sequential tunneling contribution to the current from lead α to the device reads

$$I_\alpha = e\sum_n \left(\Gamma^\alpha_{n2} - \Gamma^\alpha_{n0}\right)P^{\rm eq}_n + \Gamma^\alpha_{0n}P^{\rm eq}_0 - \Gamma^\alpha_{2n}P^{\rm eq}_2, \qquad \text{(C7)}$$

where we adopted the convention that an ingoing particle current is positive. If the system has only two terminals, $I_L = -I_R$ using this convention. In the main text, we make a different choice for the current sign: a positive (particle) current flows from the left lead to the device and then to the right lead, while a negative current flows in the opposite direction. An important thing to notice about Eqs. (C6) and (C7) is that $P^{\rm eq}$ is independent from the tunneling strength t_c between the leads and the SC island, while the current inherits a global factor $|t_c|^2$ from the rates Γ, which sets the overall scaling of I_α with t_c. Moreover both $P^{\rm eq}$ and I_α require a finite temperature T to be well defined and to avoid discontinuities in the rates and in the stationary probability distribution due to sharp jumps in the Fermi factors at $T = 0$. Hence, it is impossible to compare quantitatively the result of the perturbative rate equations and our exact solution of the unitary dynamics using tensor networks at zero temperature. The former requires $T > 0$ and only describes a $|t_c|^2$ scaling of the current. Moreover the conductance resonances are broadened only by the temperature and not by the finite coupling between the leads and the scatterer. Our MPS approach, instead, works at $T = 0$ and predicts a coupling-induced broadening of the conductance peaks as well as a less trivial scaling of the current amplitude with t_c. Thus, when comparing qualitatively the two approaches, it is necessary to choose an appropriate scaling factor if one wishes the current signals to have similar amplitudes, as we did in Fig. 8.

APPENDIX D: μ-QUENCH PROTOCOL

All the data presented in the main text are obtained following the density quench protocol, where the system is prepared at $\mathsf{t} = 0$ with the scatterer uncoupled from the leads, initialized with different Fermi energies, and then it is evolved by turning t_c on and removing the chemical potential difference at $\mathsf{t} > 0$. In this way, the system starts from a product state $|\psi_0\rangle = |\psi_L\rangle \otimes |\psi_S\rangle \otimes |\psi_R\rangle$, where L, S, and R refer to the three regions, and a particle transmitted through the device conserves both its energy and momentum.

The alternative approach is what we called the μ quench, which consists in preparing the ground state of the leads coupled to the interacting scattering region, using DMRG, but with no voltage bias. Then, at $\mathsf{t} = 0$, the chemical potential of the two leads is shifted, such that $\mu_L - \mu_R = V_b$ and a current starts flowing. In Fig. 11, we present the current following a μ quench for a topological Kitaev chain with $\mathcal{M} = 40$ sites,

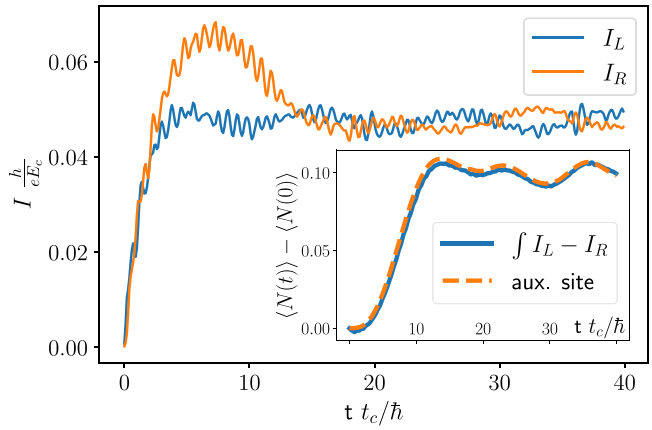

FIG. 11. Evolution in time of the left and right currents (I_L and I_R, respectively) in the μ-quench protocol. The inset shows the change in time of the charge of the SC island, both as the average particle number in the auxiliary site (dashed line) and as the integral of the current difference between the left and right contact (solid line). The parameters in the Kitaev chains are $E_c = t_0$, $t_s = 0.4E_c$, $\Delta = 0.5E_c$, $\mu_s = -0.1E_c$, $\mathcal{M} = 40$, and $t_c = 0.2E_c$, exactly the same with Fig. 5. The hopping decay length in te leads is $\xi = 40$. The current is computed in proximity of the zero-bias peak at the charge degeneracy point $n_g = 0.5$, $V_b = 0.1E_c$.

analogously to Fig. 5. Comparing the two pictures, we clearly see that the current in the μ quench displays an oscillatory behavior, on top of the usual current noise, which is absent in the density quench. These oscillation are an effect of considering finite leads and decrease by increasing their length $\mathcal{L}$ or by reducing the hopping decay length ξ, as also observed in Ref. [39]. However, this second method is suitable only for very small bias, as short decay lengths are unsuited to simulate the evolution with $V_b \gg \Gamma$.

Moreover, while for small V_b the two approaches are substantially equivalent, at large bias the μ quench introduces a nonphysical decrease of the current, resulting in a negative differential conductance. This is an effect of considering leads with a finite bandwidth: as V_b increase, the energy interval where the bands of the two leads overlap becomes smaller and smaller, as they are rigidly shifted by their chemical potential. Hence, the number of states in the leads that can contribute to transport decreases, leading to a suppression of the current [5].

The μ-quench protocol can, however, be more convenient at small biases and close to a charge degeneracy point, where the NEQSS is expected to be in a superposition of two charge states. This can be observed by the evolution of the charge in the scatter, shown in the inset of Fig. 11, where $\langle N(t)\rangle$ changes much less with respect to the density quench, see the inset of Fig. 5(a). While in the density quench the superposition is reached after an initial transient with a characteristic time set by he hybridization strength Γ, in the μ-quench protocol the system already starts from a coherent superposition, closer to the targeted NEQSS. However, for an easier comparison between simulations with different induced charge or voltage bias, we choose to use only the density quench, which, on average, also shows a more robust convergence to constant current flow.

[1] C. W. J. Beenakker, Theory of Coulomb-blockade oscillations in the conductance of a quantum dot, Phys. Rev. B **44**, 1646 (1991).

[2] I. Aleiner, P. Brouwer, and L. Glazman, Quantum effects in Coulomb blockade, Phys. Rep. **358**, 309 (2002).

[3] K. G. Wilson, The renormalization group: Critical phenomena and the Kondo problem, Rev. Mod. Phys. **47**, 773 (1975).

[4] R. Bulla, T. A. Costi, and T. Pruschke, Numerical renormalization group method for quantum impurity systems, Rev. Mod. Phys. **80**, 395 (2008).

[5] F. Heidrich-Meisner, A. E. Feiguin, and E. Dagotto, Real-time simulations of nonequilibrium transport in the single-impurity Anderson model, Phys. Rev. B **79**, 235336 (2009).

[6] M. Lotem, A. Weichselbaum, J. von Delft, and M. Goldstein, Renormalized Lindblad driving: A numerically exact nonequilibrium quantum impurity solver, Phys. Rev. Res. **2**, 043052 (2020).

[7] U. Schollwöck, The density-matrix renormalization group in the age of matrix product states, Ann. Phys. **326**, 96 (2011), January 2011 Special Issue.

[8] P. Silvi, F. Tschirsich, M. Gerster, J. Jünemann, D. Jaschke, M. Rizzi, and S. Montangero, The Tensor Networks Anthology: Simulation techniques for many-body quantum lattice systems, SciPost Phys. Lect. Notes 8 (2019).

[9] J. Haegeman, J. I. Cirac, T. J. Osborne, I. Pižorn, H. Verschelde, and F. Verstraete, Time-Dependent Variational Principle for Quantum Lattices, Phys. Rev. Lett. **107**, 070601 (2011).

[10] J. Haegeman, C. Lubich, I. Oseledets, B. Vandereycken, and F. Verstraete, Unifying time evolution and optimization with matrix product states, Phys. Rev. B **94**, 165116 (2016).

[11] R. M. Lutchyn, E. P. A. M. Bakkers, L. P. Kouwenhoven, P. Krogstrup, C. M. Marcus, and Y. Oreg, Majorana zero modes in superconductor–semiconductor heterostructures, Nat. Rev. Mater. **3**, 52 (2018).

[12] P. Schmitteckert, Nonequilibrium electron transport using the density matrix renormalization group method, Phys. Rev. B **70**, 121302(R) (2004).

[13] E. Boulat, H. Saleur, and P. Schmitteckert, Twofold Advance in the Theoretical Understanding of Far-From-Equilibrium Properties of Interacting Nanostructures, Phys. Rev. Lett. **101**, 140601 (2008).

[14] A. Branschädel, E. Boulat, H. Saleur, and P. Schmitteckert, Shot Noise in the Self-Dual Interacting Resonant Level Model, Phys. Rev. Lett. **105**, 146805 (2010).

[15] S. T. Carr, D. A. Bagrets, and P. Schmitteckert, Full Counting Statistics in the Self-Dual Interacting Resonant Level Model, Phys. Rev. Lett. **107**, 206801 (2011).

[16] F. Heidrich-Meisner, I. González, K. A. Al-Hassanieh, A. E. Feiguin, M. J. Rozenberg, and E. Dagotto, Nonequilibrium electronic transport in a one-dimensional Mott insulator, Phys. Rev. B **82**, 205110 (2010).

[17] K. A. Al-Hassanieh, A. E. Feiguin, J. A. Riera, C. A. Büsser, and E. Dagotto, Adaptive time-dependent density-matrix renormalization-group technique for calculating the conductance of strongly correlated nanostructures, Phys. Rev. B **73**, 195304 (2006).

[18] A. Feiguin, P. Fendley, M. P. A. Fisher, and C. Nayak, Nonequilibrium Transport through a Point Contact in the $\nu = 5/2$ Non-Abelian Quantum Hall State, Phys. Rev. Lett. **101**, 236801 (2008).

[19] B. M. Schoenauer, N. M. Gergs, P. Schmitteckert, F. Evers, and D. Schuricht, Long-lived circulating currents in strongly correlated nanorings, Phys. Rev. Res. **1**, 022006 (2019).

[20] F. Güttge, F. B. Anders, U. Schollwöck, E. Eidelstein, and A. Schiller, Hybrid NRG-DMRG approach to real-time dynamics of quantum impurity systems, Phys. Rev. B **87**, 115115 (2013).

[21] F. Schwarz, I. Weymann, J. von Delft, and A. Weichselbaum, Nonequilibrium Steady-State Transport in Quantum Impurity Models: A Thermofield and Quantum Quench Approach Using Matrix Product States, Phys. Rev. Lett. **121**, 137702 (2018).

[22] M. M. Rams and M. Zwolak, Breaking the Entanglement Barrier: Tensor Network Simulation of Quantum Transport, Phys. Rev. Lett. **124**, 137701 (2020).

[23] L. Kohn and G. E. Santoro, Efficient mapping for Anderson impurity problems with matrix product states, Phys. Rev. B **104**, 014303 (2021).

[24] L. Kohn and G. E. Santoro, Quench dynamics of the Anderson impurity model at finite temperature using matrix product states: Entanglement and bath dynamics, J. Stat. Mech.: Theory Exp. (2022) 063102.

[25] A. Keselman, C. Murthy, B. van Heck, and B. Bauer, Spectral response of Josephson junctions with low-energy quasiparticles, SciPost Phys. **7**, 050 (2019).

[26] J. Dukelsky, S. Pittel, and G. Sierra, Colloquium: Exactly solvable Richardson-Gaudin models for many-body quantum systems, Rev. Mod. Phys. **76**, 643 (2004).

[27] J. C. Estrada Saldaña, A. Vekris, L. Pavešić, P. Krogstrup, R. Žitko, K. Grove-Rasmussen, and J. Nygård, Excitations in a superconducting Coulombic energy gap, Nat. Commun. **13**, 1 (2022).

[28] L. Pavešić, D. Bauernfeind, and R. Žitko, Subgap states in superconducting islands, Phys. Rev. B **104**, L241409 (2021).

[29] L. Pavešić and R. Žitko, Qubit based on spin-singlet Yu-Shiba-Rusinov states, Phys. Rev. B **105**, 075129 (2022).

[30] P. Calabrese and J. Cardy, Quantum quenches in 1+ 1 dimensional conformal field theories, J. Stat. Mech.: Theory Exp. (2016) 064003.

[31] B. Bertini, M. Collura, J. De Nardis, and M. Fagotti, Transport in Out-Of-Equilibrium *xxz* Chains: Exact Profiles of Charges and Currents, Phys. Rev. Lett. **117**, 207201 (2016).

[32] M. Collura, A. De Luca, and J. Viti, Analytic solution of the domain-wall nonequilibrium stationary state, Phys. Rev. B **97**, 081111(R) (2018).

[33] A. Biella, M. Collura, D. Rossini, A. De Luca, and L. Mazza, Ballistic transport and boundary resistances in inhomogeneous quantum spin chains, Nat. Commun. **10**, 4820 (2019).

[34] M. Collura, A. De Luca, P. Calabrese, and J. Dubail, Domain wall melting in the spin-$\frac{1}{2}$ xxz spin chain: Emergent Luttinger liquid with a fractal quasiparticle charge, Phys. Rev. B **102**, 180409(R) (2020).

[35] E. Langmann, J. L. Lebowitz, V. Mastropietro, and P. Moosavi, Steady states and universal conductance in a quenched Luttinger model, Commun. Math. Phys. **349**, 551 (2017).

[36] B. van Heck, R. M. Lutchyn, and L. I. Glazman, Conductance of a proximitized nanowire in the Coulomb blockade regime, Phys. Rev. B **93**, 235431 (2016).

[37] A. Y. Kitaev, Unpaired Majorana fermions in quantum wires, Phys. Usp. **44**, 131 (2001).

[38] A. K. Mitchell, M. R. Galpin, S. Wilson-Fletcher, D. E. Logan, and R. Bulla, Generalized Wilson chain for solving

multichannel quantum impurity problems, Phys. Rev. B **89**, 121105(R) (2014).

[39] L. G. G. V. Dias da Silva, F. Heidrich-Meisner, A. E. Feiguin, C. A. Büsser, G. B. Martins, E. V. Anda, and E. Dagotto, Transport properties and Kondo correlations in nanostructures: Time-dependent DMRG method applied to quantum dots coupled to Wilson chains, Phys. Rev. B **78**, 195317 (2008).

[40] M. Ljubotina, S. Sotiriadis, and T. Prosen, Non-equilibrium quantum transport in presence of a defect: The non-interacting case, SciPost Phys. **6**, 004 (2019).

[41] C.-C. Chien, M. Di Ventra, and M. Zwolak, Landauer, Kubo, and microcanonical approaches to quantum transport and noise: A comparison and implications for cold-atom dynamics, Phys. Rev. A **90**, 023624 (2014).

[42] E. H. Lieb and D. W. Robinson, The finite group velocity of quantum spin systems, Commun. Math. Phys. **28**, 251 (1972).

[43] L. Bonnes, F. H. L. Essler, and A. M. Läuchli, "Light-Cone" Dynamics After Quantum Quenches in Spin Chains, Phys. Rev. Lett. **113**, 187203 (2014).

[44] J. Viti, J.-M. Stéphan, J. Dubail, and M. Haque, Inhomogeneous quenches in a free fermionic chain: Exact results, Europhys. Lett. **115**, 40011 (2016).

[45] F. H. L. Essler and M. Fagotti, Quench dynamics and relaxation in isolated integrable quantum spin chains, J. Stat. Mech.: Theory Exp. (2016) 064002.

[46] S. R. White, Density Matrix Formulation for Quantum Renormalization Groups, Phys. Rev. Lett. **69**, 2863 (1992).

[47] S. R. White, Density-matrix algorithms for quantum renormalization groups, Phys. Rev. B **48**, 10345 (1993).

[48] M. Fishman, S. R. White, and E. M. Stoudenmire, The ITensor software library for tensor network calculations, arXiv:2007.14822.

[49] The source code can be found in the repository: https://github.com/chiaminchung/QuenchTransport.

[50] N. Schuch, M. M. Wolf, K. G. H. Vollbrecht, and J. I. Cirac, On entropy growth and the hardness of simulating time evolution, New J. Phys. **10**, 033032 (2008).

[51] M. Yang and S. R. White, Time-dependent variational principle with ancillary Krylov subspace, Phys. Rev. B **102**, 094315 (2020).

[52] Y.-T. Kang, C.-Y. Lo, M. Oshikawa, Y.-J. Kao, and P. Chen, Two-wire junction of inequivalent Tomonaga-Luttinger liquids, Phys. Rev. B **104**, 235142 (2021).

[53] A. P. Higginbotham, S. M. Albrecht, G. Kiršanskas, W. Chang, F. Kuemmeth, P. Krogstrup, T. S. Jespersen, J. Nygård, K. Flensberg, and C. M. Marcus, Parity lifetime of bound states in a proximitized semiconductor nanowire, Nat. Phys. **11**, 1017 (2015).

[54] S. Vaitiekėnas, R. S. Souto, Y. Liu, P. Krogstrup, K. Flensberg, M. Leijnse, and C. M. Marcus, Evidence for spin-polarized bound states in semiconductor–superconductor–ferromagnetic-insulator islands, Phys. Rev. B **105**, L041304 (2022).

[55] S. M. Albrecht, A. P. Higginbotham, M. Madsen, F. Kuemmeth, T. S. Jespersen, J. Nygård, P. Krogstrup, and C. M. Marcus, Exponential protection of zero modes in Majorana islands, Nature (London) **531**, 206 (2016).

[56] A. Vekris, J. C. E. Saldaña, T. Kanne, T. Hvid-Olsen, M. Marnauza, D. Olsteins, M. M. Wauters, M. Burrello, J. Nygård, and K. Grove-Rasmussen, Electronic transport in double-nanowire superconducting islands with multiple terminals, Nano Lett. **22**, 5765 (2022).

[57] Y.-H. Lai, S. Das Sarma, and J. D. Sau, Theory of Coulomb blockaded transport in realistic Majorana nanowires, Phys. Rev. B **104**, 085403 (2021).

[58] G. W. Semenoff and P. Sodano, Stretched quantum states emerging from a Majorana medium, J. Phys. B: At., Mol. Opt. Phys. **40**, 1479 (2007).

[59] L. Fu, Electron Teleportation via Majorana Bound States in a Mesoscopic Superconductor, Phys. Rev. Lett. **104**, 056402 (2010).

[60] V. Zauner, M. Ganahl, H. G. Evertz, and T. Nishino, Time evolution within a comoving window: Scaling of signal fronts and magnetization plateaus after a local quench in quantum spin chains, J. Phys.: Condens. Matter **27**, 425602 (2015).

[61] C.-Y. Lo, Y. Fukusumi, M. Oshikawa, Y.-J. Kao, and P. Chen, Crossover of correlation functions near a quantum impurity in a Tomonaga-Luttinger liquid, Phys. Rev. B **99**, 121103(R) (2019).

[62] Y. Wu, Time-dependent variational principle for mixed matrix product states in the thermodynamic limit, Phys. Rev. B **102**, 134306 (2020).

[63] G. Wójtowicz, J. E. Elenewski, M. M. Rams, and M. Zwolak, Open-system tensor networks and Kramers' crossover for quantum transport, Phys. Rev. A **101**, 050301(R) (2020).

[64] M. Brenes, J. J. Mendoza-Arenas, A. Purkayastha, M. T. Mitchison, S. R. Clark, and J. Goold, Tensor-Network Method to Simulate Strongly Interacting Quantum Thermal Machines, Phys. Rev. X **10**, 031040 (2020).

[65] T. Rakovszky, C. W. von Keyserlingk, and F. Pollmann, Dissipation-assisted operator evolution method for capturing hydrodynamic transport, Phys. Rev. B **105**, 075131 (2022).

[66] B. Béri and N. R. Cooper, Topological Kondo Effect with Majorana Fermions, Phys. Rev. Lett. **109**, 156803 (2012).

[67] B. Béri, Majorana-Klein Hybridization in Topological Superconductor Junctions, Phys. Rev. Lett. **110**, 216803 (2013).

[68] A. Altland and R. Egger, Multiterminal Coulomb-Majorana Junction, Phys. Rev. Lett. **110**, 196401 (2013).

[69] A. Altland, B. Béri, R. Egger, and A. M. Tsvelik, Multichannel Kondo Impurity Dynamics in a Majorana Device, Phys. Rev. Lett. **113**, 076401 (2014).

[70] A. Zazunov, A. Altland, and R. Egger, Transport properties of the Coulomb–Majorana junction, New J. Phys. **16**, 015010 (2014).

[71] B. Béri, Exact Nonequilibrium Transport in the Topological Kondo Effect, Phys. Rev. Lett. **119**, 027701 (2017).

[72] K. Michaeli, L. A. Landau, E. Sela, and L. Fu, Electron teleportation and statistical transmutation in multiterminal Majorana islands, Phys. Rev. B **96**, 205403 (2017).

[73] F. Buccheri and R. Egger, Topological Kondo effect, in *Strongly Coupled Field Theories for Condensed Matter and Quantum Information Theory*, edited by A. Ferraz, K. S. Gupta, G. W. Semenoff, and P. Sodano (Springer International Publishing, Cham, 2020), pp. 131–153.

[74] J. I. Väyrynen, A. E. Feiguin, and R. M. Lutchyn, Signatures of topological ground state degeneracy in Majorana islands, Phys. Rev. Res. **2**, 043228 (2020).

[75] M. Papaj, Z. Zhu, and L. Fu, Multichannel charge Kondo effect and non-Fermi-liquid fixed points in conventional and topological superconductor islands, Phys. Rev. B **99**, 014512 (2019).

[76] D. Giuliano, L. Lepori, and A. Nava, Tunable spin/charge Kondo effect at a double superconducting island connected to two spinless quantum wires, Phys. Rev. B **101**, 195140 (2020).

[77] C. Han, Z. Iftikhar, Y. Kleeorin, A. Anthore, F. Pierre, Y. Meir, A. K. Mitchell, and E. Sela, Fractional Entropy of Multichannel Kondo Systems from Conductance-Charge Relations, Phys. Rev. Lett. **128**, 146803 (2022).

[78] T. Prosen and M. Žnidarič, Matrix product simulations of non-equilibrium steady states of quantum spin chains, J. Stat. Mech.: Theory Exp. (2009) P02035.

[79] G. Benenti, G. Casati, T. Prosen, D. Rossini, and M. Žnidarič, Charge and spin transport in strongly correlated one-dimensional quantum systems driven far from equilibrium, Phys. Rev. B **80**, 035110 (2009).

[80] I. de Vega and M.-C. Bañuls, Thermofield-based chain-mapping approach for open quantum systems, Phys. Rev. A **92**, 052116 (2015).

[81] V. Bouchiat, D. Vion, P. Joyez, D. Esteve, and M. H. Devoret, Quantum coherence with a single Cooper pair, Phys. Scr. **T76**, 165 (1998).

[82] J. Danon, A. B. Hellenes, E. B. Hansen, L. Casparis, A. P. Higginbotham, and K. Flensberg, Nonlocal Conductance Spectroscopy of Andreev Bound States: Symmetry Relations and BCS Charges, Phys. Rev. Lett. **124**, 036801 (2020).

[83] G. C. Ménard, G. L. R. Anselmetti, E. A. Martinez, D. Puglia, F. K. Malinowski, J. S. Lee, S. Choi, M. Pendharkar, C. J. Palmstrøm, K. Flensberg, C. M. Marcus, L. Casparis, and A. P. Higginbotham, Conductance-Matrix Symmetries of a Three-Terminal Hybrid Device, Phys. Rev. Lett. **124**, 036802 (2020).

[84] S. Singh, R. N. C. Pfeifer, and G. Vidal, Tensor network decompositions in the presence of a global symmetry, Phys. Rev. A **82**, 050301(R) (2010).

[85] E. Zohar and M. Burrello, Building projected entangled pair states with a local gauge symmetry, New J. Phys. **18**, 043008 (2016).

[86] Z. He and A. J. Millis, Entanglement entropy and computational complexity of the Anderson impurity model out of equilibrium: Quench dynamics, Phys. Rev. B **96**, 085107 (2017).

Coexistence of superconductivity with partially filled stripes in the Hubbard model

Hao Xu,[1,*] Chia-Min Chung,[2,3,4,*] Mingpu Qin,[5] Ulrich Schollwöck,[6,7] Steven R. White,[8] and Shiwei Zhang[9]

[1]*Department of Physics, College of William and Mary, Williamsburg, Virginia 23187, USA*
[2]*Department of Physics, National Sun Yat-sen University, Kaohsiung 80424, Taiwan*
[3]*Center for Theoretical and Computational Physics, National Sun Yat-Sen University, Kaohsiung 80424, Taiwan*
[4]*Physics Division, National Center for Theoretical Sciences, Taipei 10617, Taiwan*
[5]*Key Laboratory of Artificial Structures and Quantum Control, School of Physics and Astronomy, Shanghai Jiao Tong University, Shanghai 200240, China*
[6]*Arnold Sommerfeld Center for Theoretical Physics, Ludwig-Maximilians-Universität München, 80333 Munich, Germany*
[7]*Munich Center for Quantum Science and Technology (MCQST), 80799 Munich, Germany*
[8]*Department of Physics and Astronomy, University of California, Irvine, California 92697, USA*
[9]*Center for Computational Quantum Physics, Flatiron Institute, New York, NY 10010, USA*

Combining the complementary capabilities of two of the most powerful modern computational methods, we find superconductivity in both the electron- and hole-doped regimes of the two-dimensional Hubbard model (with next nearest neighbor hopping). In the electron-doped regime, superconductivity is weaker and is accompanied by antiferromagnetic Néel correlations at low doping. The strong superconductivity on the hole-doped side coexists with stripe order, which persists into the overdoped region with weaker hole density modulation. These stripe orders, neither filled as in the pure Hubbard model (no next nearest neighbor hopping) nor half-filled as seen in previous state-of-the-art calculations, vary in fillings between 0.6 and 0.8. The resolution of the tiny energy scales separating competing orders requires exceedingly high accuracy combined with averaging and extrapolating with a wide range of system sizes and boundary conditions. These results validate the applicability of this iconic model for describing cuprate high-T_c superconductivity.

I. INTRODUCTION

Does the Hubbard model qualitatively capture the essential physics of the high temperature superconducting cuprates? This question has been debated since shortly after these materials were discovered [1–10]. As the decades have passed it has become clearer that the answer has to come from simulations powerful enough to give definitive results on the properties of the model, so that one can see whether these properties match those observed experimentally. This has proved to be especially difficult because the ground states of the models have been shown to be exceptionally sensitive to small changes in the model terms and parameters, with competing [11] or cooperating [12] charge, spin [13], and superconducting (SC) orders [14–18]. The relevant model parameters are in the most difficult regime – moderately strongly-coupled – where most approaches struggle. The frequent presence of stripes in the ground states increases the sizes of the clusters needed to extrapolate to the thermodynamic limit.

A powerful tool has emerged to help overcome these difficulties: the use of combinations of simulation methods with complementary strengths and weaknesses[19]. The density matrix renormalization group (DMRG) [20–22] provides the most accurate and reliable results when applied on fairly narrow cylinders [23]. Other methods work either directly in the thermodynamic limit [24, 25] or at least on much wider clusters [26], but have approximations tied to unit cell size[24, 27, 28], coupling strength, etc [25, 29, 30]. The constrained path (CP) auxiliary field quantum Monte Carlo (AFQMC) method [26, 31, 32] is particularly complementary to DMRG: it can be used on much wider systems; the errors from CP to control the sign problem have been consistently modest [19]; and the underlying approximation of CP is unrelated to the low entanglement approximation of DMRG. AFQMC is based on a wave picture of superposition of Slater determinants, while DMRG is rooted in the particle picture with strong coupling. Their quantitative handshake proved to be crucial for uncovering the delicate nature of the stripe correlations as we discuss below. Previously, we used this combination, extrapolating to the two-dimensional thermodynamic limit, to find that superconductivity is absent in the pure (i.e., with no next nearest-neighbor hopping) Hubbard model [11]. In that case, the lack of superconductivity was tied to the occurrence of filled striped states[33].

Here, we apply this approach, with new developments, to tackle the Hubbard model with a non-zero next nearest-neighbor hopping, t'. In connection to the typical phase diagram of cuprates, a nonzero t' is necessary to account for the particle-hole asymmetry and the band structures. The $t' \neq 0$ model is significantly more difficult computationally, with challenges for both DMRG and AFQMC. Where both methods apply, DMRG certifies the high accuracy and reliability of AFQMC as used here. As discussed below, in cases of ambiguity (e.g., in some width-6 cylinders), resolving the discrepancies

*These two authors contributed equally to this work.

has often created new synergy between the two methods, and led to new insights. The phase diagram with t' also turns out to be significantly more complicated, with partially filled stripes coexisting with superconductivity on the hole-doped side, and uniform antiferromagnetic order coexisting with superconductivity on the electron side. The final results for superconductivity, extrapolated to the thermodynamic limit, are impressively similar to the properties of cuprates, with both electron and holed doped SC "domes", but with the hole doped side being significantly stronger.

The Hamiltonian of the Hubbard model is

$$\hat{H} = -t \sum_{\langle ij \rangle, \sigma} \hat{c}^{\dagger}_{i\sigma} \hat{c}_{j\sigma} - t' \sum_{\langle\langle ij \rangle\rangle, \sigma} \hat{c}^{\dagger}_{i\sigma} \hat{c}_{j\sigma} + U \sum_{i} \hat{n}_{i\uparrow} \hat{n}_{i\downarrow} - \mu \sum_{i\sigma} \hat{n}_{i\sigma} \tag{1}$$

where i or j labels a site on a square lattice, $\hat{c}^{\dagger}_{i\sigma}$ is the electron creation operator, $\sigma = \{\uparrow, \downarrow\}$ denotes spin, $\hat{n}_{i\sigma} = \hat{c}^{\dagger}_{i\sigma} \hat{c}_{i\sigma}$ is the particle-number operator, and $\langle ij \rangle$ and $\langle\langle ij \rangle\rangle$ indicate nearest- and next-nearest-neighbors, respectively. We set t as the energy unit. In cuprates $t' < 0$ [34]; however,using a particle-hole transformation to map fillings $1+\delta \to 1-\delta$, we can study electron doping by changing the sign of t'. We use $t' = -0.2$ for hole-doping and $t' = +0.2$ for electron-doping, appropriate values for cuprates based on band structure calculations [35, 36]. The onsite repulsion U is fixed at $U = 8$, again a representative value for cuprates. We scan a range of doping (denoted by δ) by varying μ.

Our study focuses on the ground state, which we obtain in either cylindrical or fully periodic systems. The use of cylinders serves two purposes. First they allow direct comparisons between AFQMC and DMRG, which is highly accurate in narrow cylinders. Second, they are convenient for studying spin and charge orders, in which we apply spin-symmetry-breaking pinning fields on the edges of the cylinder to help detect ordering from the resulting local spin and charge densities. The fully periodic simulation cells allow AFQMC to better approach the thermodynamic limit (TDL). As shown below, it turns out to be crucial to systematically average over different boundary conditions. To compute the pairing order parameter, we apply twist averaged boundary conditions (TABC) over a large number of random twists, in systems with up to 500 lattice sites. The computations presented in this work became possible only with new algorithmic developments in both our methods, which improved capability and increased accuracy, as we discuss further in the Method Section.

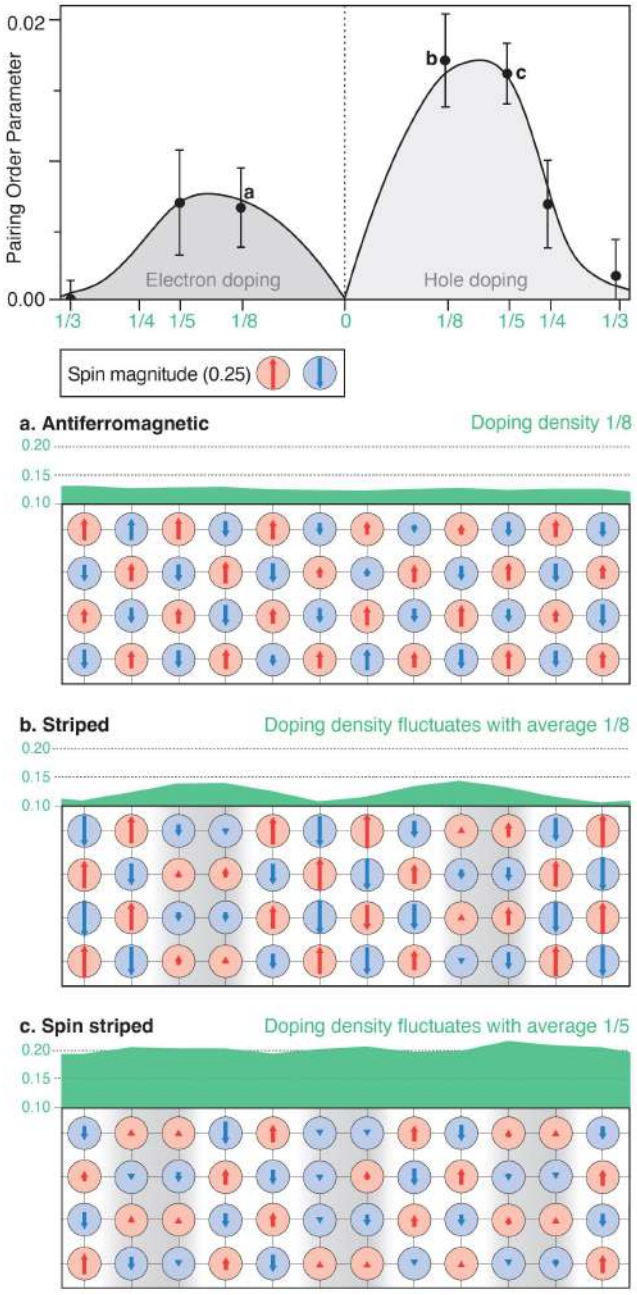

FIG. 1: The d-wave pairing order parameter versus doping δ in the ground state for the hole-doped ($t' = -0.2$) and electron-doped ($t' = +0.2$) regimes. Representative spin and charge correlations are also shown for three parameter sets a, b, and c. Δ_d are the spontaneous pairing order in the thermodynamic limit, while the spin and charge (hole) patterns are drawn from the middle of 28×8 (a), 24×8 (b), and 40×8 (c) cylinders with antiferromagnetic spin pinning fields applied to the two edges. Note that hole densities start at 0.1. Grey shadows for spins are to aid the eye.

II. RESULTS

A. Overview of pairing and coexisting spin/charge orders

Figure 1 presents an overview of our results, a "phase diagram" of the computed pairing order parameter, together with representative spin and charge correlations. The pairing order parameters have been extrapolated to the TDL, using full TABC in large simulation cells (see Method and SM). We expect this zero-temperature property to be loosely connected to the transition temperature T_c most readily observed experimentally (however, see [37, 38]). On both the electron- and hole-doped sides, we find dome-like d-wave pairing orders which resemble the T_c domes in the typical phase diagram of cuprates. The pairing order is significantly larger in the hole-doped region than in the electron-doped region, which is also consistent with the phase diagram of cuprates [39]. Spin and hole densities are shown for the three representative systems marked as a, b, and c. These calculations were performed with AFM pinning fields on the edges of the cylindrical simulation cells (details in SM). The spin and hole densities thus provide a simple and convenient way to visualize the spin and charge correlations. We have taken care to ensure that the results are drawn from very large systems and the spin and charge patterns are representative of different boundary conditions. In the electron-doped region, the spins show single-domain antiferromagnetism with nearly uniform hole densities in the bulk. In the hole-doped region, stripe and spin-density wave (SDW) correlations are observed, with modulated antiferromagnetic domains separated by phase flip lines where holes are more concentrated. In contrast with the pure Hubbard model, we find that the wavelength of the modulation is not an integer multiple of $1/\delta$ (filled stripes). Nor are the stripes half-filled as seen in previous state-of-the-art calculations [40]. Rather, they are best described as partially filled, with fractional fillings which vary with δ as well as system size and boundary conditions. These behaviors of spin and charge are again consistent with the phase diagram of the cuprates [39], where uniform AF correlations persist with substantial doping on the electron-doped side, but short or long-ranged incommensurate magnetism and stripes are observed starting at small doping on the hole-doped side [41, 42].

This phase diagram contrasts sharply with that of the t-t'-J model[43, 44], which can be derived as an approximate strong-coupling Hubbard model at low doping. In the t-t'-J model, recent DMRG studies all point to strong d-wave superconductivity on the electron-doped side [43–45], which coexists with antiferromagnetic correlations with increasing strength as t' increases; some differences remain concerning whether long-range AF order occurs [46]. No superconductivity, only stripes, have been found on the hole-doped side. It has been an open question whether this failure of the t-t'-J model to qualitatively explain the cuprates was due to the strong-coupling approximations of that model, or to other flaws or missing terms affecting both the Hubbard and t-t'-J (single band) models. Here the strong differences in the phase diagrams of the two models point to the former. These differences have not been clear in previous studies on narrower cylinders, which are impacted by strong finite-size effects [47, 48].

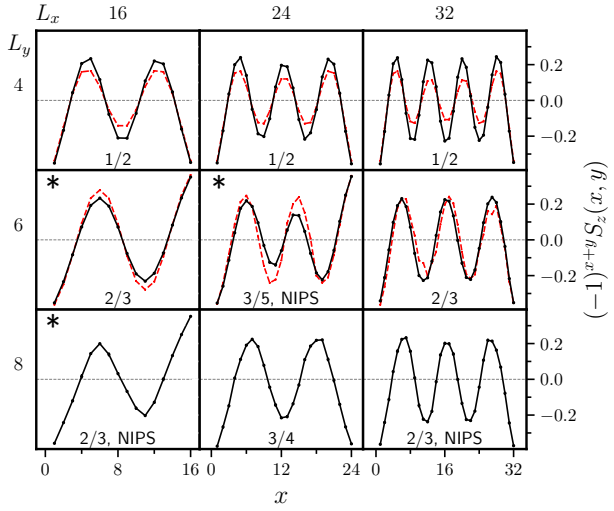

FIG. 2: Evolution of the stripe patterns with system size ($\delta = 1/8$, hole-doped). The staggered spin densities are shown as linecuts in periodic cylinders. The length of the cylinder (L_x) is varied across the three columns and the width (L_y) across rows. AFM pinning fields are applied at the two edges of the cylinder ($x = 1$ and $x = L_x$), either in phase or with a π-phase shift (marked by an asterisk); the one with lower energy is shown. The filling fraction f of each stripe pattern is indicated, with NIPS denoting non integer-pair stripes. DMRG results (red) are shown for width-4 and 6 systems and AFQMC results (black) are in good agreement with them.

B. Underdoped region: 1/8 hole doping

A relatively large pairing order parameter is found here, in coexistence with stripe correlations, as shown in Fig. 1. To better understand the nature of the spin and charge correlations, we systematically study their evolution with system sizes in Fig. 2. The computations were performed in $L_x \times L_y$ cells, with periodic (PBC) or anti-periodic boundary condition (APBC) in the $\hat{y}$-direction and open BC along $\hat{x}$ (i.e., cylinders). AFM pinning fields (along $\hat{z}$) were applied at $x = 1$ and L_x to break the SU(2) symmetry and induce local spin orders, such that the local spin density $S_z(x, y)$ becomes a proxy of spin-spin correlations away from the edges of the cylinder.

Modulated AFM patterns are clearly seen in all the systems. Correspondingly, hole densities are enhanced at the nodes of the spin modulation, as illustrated in Fig. 1

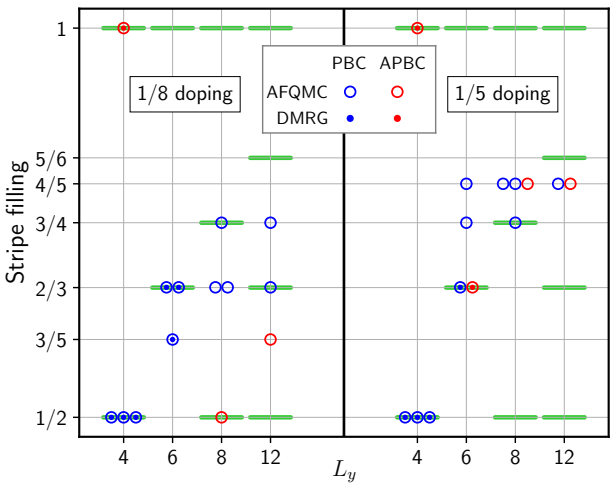

FIG. 3: Partially filled stripe patterns on the hole-doped side, at $\delta = 1/8$ and $1/5$. The stripe fillings are shown for a variety of system sizes, in cylindrical cells with width $L_y = 4$ up to 12, and lengths ranging from 16 to 48 (shown as adjacent symbols at fixed L_y). Results for both PBC and APBC are shown. Narrow cylinders favor integer-pair stripes (IPS, indicated by green bars). Fluctuations are strong even in large systems.

(results on the corresponding hole densities for Fig. 2 can be found in SM). The characteristic wavelength of the modulation, $\lambda_{\rm SDW}$, varies with system size. We define a filling fraction of the stripe: $f \equiv \delta\,\lambda_{\rm SDW}/2$, i.e., the number of holes per lattice spacing along a stripe. In the pure Hubbard model, $f = 1$ since $\lambda_{\rm SDW} = 2/\delta$ [49, 50]. Then, *nominally* the number of electron pairs per stripe is $n_p \equiv f\,L_y/2$. If n_p is an integer, we refer to the state as integer-pair stripe (IPS); otherwise the state is labeled as non-IPS (NIPS).

Previous studies in width-4 cylinders have found that the ground state in this system has half-filled stripes [40, 43, 44]. Our results confirm this picture, with good agreement between AFQMC and DMRG, but also show that the half-filled stripe turns out to be special to width-4. As the system size increases, the stripe filling fluctuates between 3/5 and 3/4. NIPS states appear frequently, which have not been observed before. Previous calculations [11, 51] show that states with IPS are favored, which was taken as an indication of the existence of local pairing of electrons in the stripe state. Here, with the inclusion of t', the electron is more mobile and pairs of electrons become coherent to display long-range pairing order. This is further discussed and contrasted with the over-doped region next.

C. Overdoped region: 1/5 hole doping

A strong superconducting order parameter is found in the ground state of the hole overdoped region of $\delta = 1/5$, with strength comparable to $\delta = 1/8$ (see Fig. 1). The behavior of spin and charge correlations show common features but also significant differences between the two regions. Figure 3 summarizes their stripe fillings side by side, based on computations in about 30 systems. Several trends are evident. In narrow cylinders, IPS states are favored at both dopings. In over a dozen different width-4 and width-6 systems across the two dopings, AFQMC and DMRG agree in each case on the stripe wavelength and filling fraction. In both regimes the filling fraction varies widely with system sizes and boundary conditions, and fluctuations continue through systems with over 500 lattice sites. As the size grows (wider cylinders), IPS states are no longer favored, and both systems tend to fractional stripe fillings. These results indicate that with t', the stripe patterns — but not the existence of stripes — are much more fragile than in the pure Hubbard model.

Both the spin and charge modulations are weaker at 1/5 doping than at 1/8. Although f is larger in the TDL, the holes are more mobile and spread out in the overdoped region. The hole density is nearly uniform, with less than 5% of the holes contributing to the density fluctuations. At 1/8 doping, the stripe order is more pronounced, as illustrated in Fig. 1. Still, the peak density of holes, at the nodes of the spin correlation, is only $\sim$ 30% higher than the average. The notion of stripe filling derives from a particle picture, most applicable to holes in Wigner-crystal-like distributions. The holes here have a strong wave character [49], with which the fractional fillings of stripes we observe are more readily compatible.

D. Electron doped region

Experimentally, the electron-doped side is simpler, without the competing stripe state [41, 52] or pseudogap phase in cuprates [39]. The critical doping for the long-range AF order on the electron-doped side is larger than that on the hole-doped side, the superconducting dome is smaller, and the transition temperature is lower. The phase diagram in Fig. 1 and the spin and hole densities in Fig. 4 are consistent with these features.

Our results reveal several other important features on the electron-doped side. There are considerable variations of the spin and charge correlations with system sizes and boundary conditions, even though the sensitivity is less compared to the hole-doped side. As illustrated in the SM, two entirely different ground-state orders are obtained from width-4 and width-6 cylinders; APBC and PBC also lead to opposite conclusions in each simulation cell. Even in the width-8 systems in Fig. 4, which display robust Néel order, different boundary conditions still show variations in the charge correlation. Superconductivity manifests a more dramatic volatility. Using PBC, the most common approach to date, calculations in width-4 and width-6 cylinders would conclude a strong pairing order in the electron-doped regime. (Note that

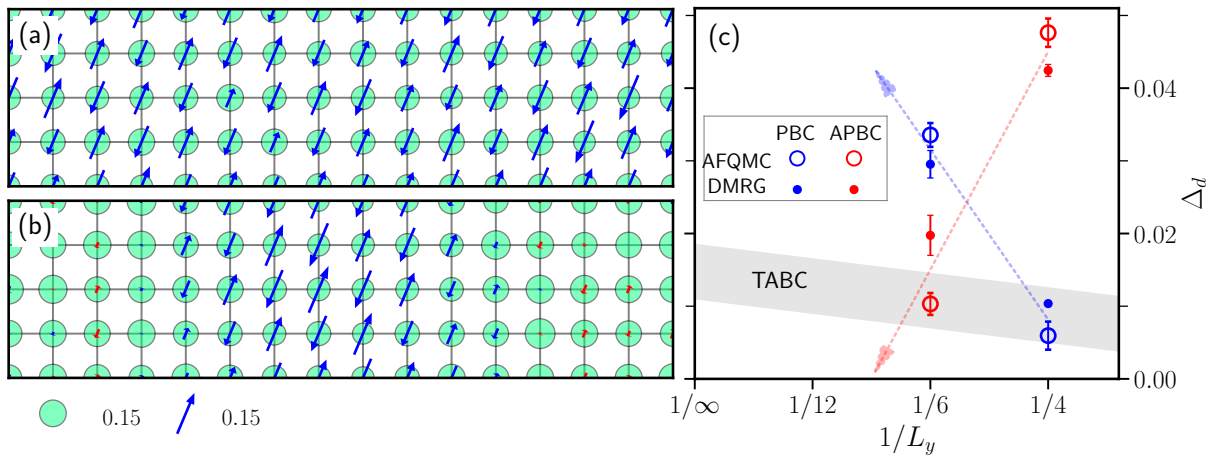

FIG. 4: Spin, charge, and pairing properties on the electron doped side ($\delta = 1/8$), and their variations with boundary conditions. (a) APBC along $\hat{y}$-direction in a 28×8 cylinder gives nearly uniform Neel order (only a 16×4 central region is shown). (b) Under PBC a modulated AFM order with larger spatial variations in spin magnitude is seen. (c) The computed pairing orders in 16×4 and 16×6 cylinders (at a fixed value $h_d = 0.021$ of applied global d-wave pairing fields) show opposite trends with PBC and APBC. The final pairing order, computed from TABC with fully periodic supercells of increasing L_y, is shown together with the TDL extrapolation by the gray band.

DMRG and AFQMC give fully consistent results.) In contrast, under APBC the same calculations predict no pairing. The uncertainties with respect to finite size and boundary conditions are much larger than the final signal at the TDL. Thus even a qualitative conclusion on superconductivity would be challenging without our new approaches employing TABC, systematic extrapolation to large sizes, and other methodological advances, which are discussed next.

III. METHOD

The physics of the Hubbard model has proved highly elusive and challenging to pin down. This was magnified substantially with a non-zero t'. The difficulties include more sensitivity and stronger dependency on system size and BC, as we have illustrated. In addition, t' turns out to affect the interplay between low-lying states in significant ways. For instance, with $t' = 0$, stripe and superconductivity manifest as competing orders. Filled stripe states are particularly stable, with nesting contributing a key factor. A non-zero t' affects the nesting condition (frustrates the Néel order) and alters the landscape of the low-lying states. This has demanded much higher resolution from the numerical methods.

The methodologies employed in this work have a number of distinguishing features which made it possible to achieve a qualitatively higher level of accuracy and reliability. Two complementary, state-of-the-art computational methods are used synergistically. We implement both U(1) [53] and SU(2) symmetry-adapted [54] DMRG calculations for different setups and push them to the large bond-dimension limit. In AFQMC, we introduce a further advance in the optimization of the constraining trial wave function, which is determined fully self-consistently [32], with no input parameter. Extensive and detailed comparisons between AFQMC and DMRG are performed on width-4 and width-6 cylinders, under identical conditions. The same AFQMC algorithm, which has no room for tuning, is applied to larger systems. The formulation of systematic twist averaging for the computation of the pairing order parameters provides an effective way to sample the low-lying states.

A. Twist averaging as an effective means to sample low-lying states

The use of twist-averaging [55, 56] in this work has two crucial roles. First, systematically averaging over twist angles, combined with the ability to reach large system sizes and careful finite size extrapolation, enables us to approach the TDL reliably. Second, the random twist angles provide an effective means to sample the low-lying states, and their averaging reduces the impact of rare events of accidental degeneracy, and smoothes out the effect of level crossings as a function of an applied pairing field (see SM).

As shown in Fig. 4, different boundary conditions can result in variations in the pairing order parameter which are many times larger than the signal, even in nominally rather large sizes (width-6 cylinders). Both PBC and APBC are twist angles of special symmetry, and are often particularly volatile. We apply TABC with quasi-random twist angles [56]. The TBC can be thought of as the electron gaining a phase when it crosses the boundary. Equivalently, we can choose another gauge by dis-

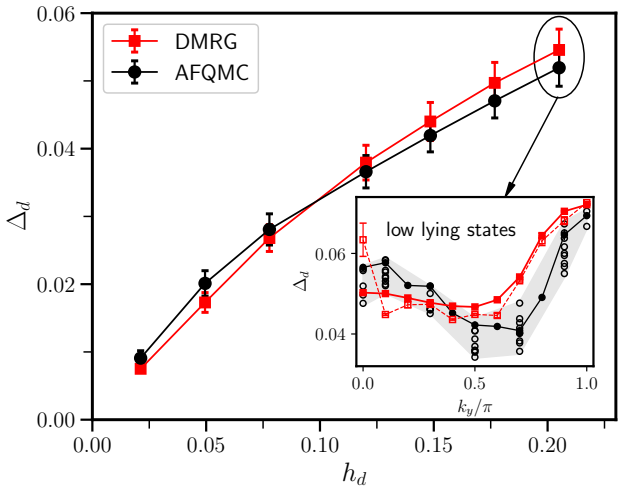

FIG. 5: Importance of TABC for accurate determination of the pairing order. The main figure shows the d-wave pairing order parameters in a 20×4 cylindrical cell at 1/5 hole doping, after full twist-averaging over k_y. AFQMC and DMRG results agree across the entire range of h_d, the strength of the applied pairing fields. The inset focuses on $h_d = 0.205$. Δ_d computed from DMRG and AFQMC are shown as a function of k_y, for the ground state (connected by solid line) and some of the lowest-lying excited states (open symbols). Averages of the solid symbols lead to the TABC results in the main figure.

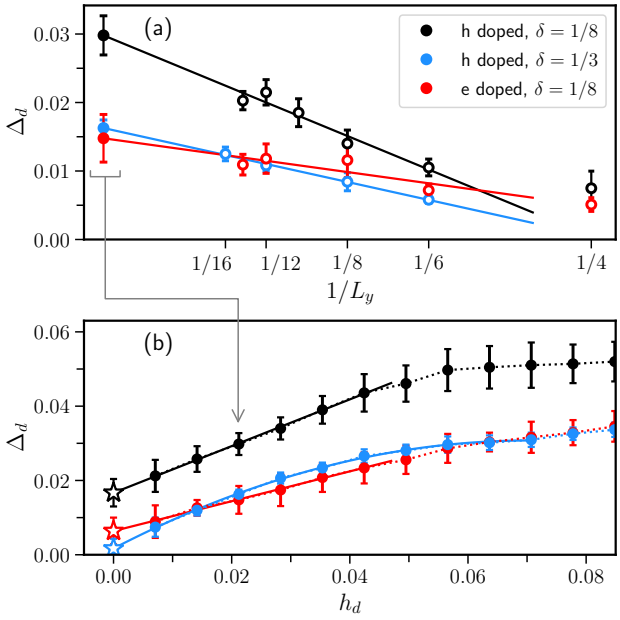

FIG. 6: Computation of the ground-state pairing order parameter at the thermodynamic limit. (a) shows extrapolation to the TDL at a fixed h_d, the strength of the d-wave pairing fields. (b) shows extrapolation of the TDL result from (a) to $h_d \to 0$. Three representative systems are shown. In (a), each data point is obtained by TABC over (k_x, k_y) in supercells of $L_x \times L_y$, and only results from large supercells are included. In (b) linear or quadratic fits are performed at small values of h_d, with extrapolated values marked as stars.

tributing the phase evenly in each hopping term. When a twist is applied, care must be taken in defining the pairing order parameter, whose form is gauge-dependent but the expectation value should be gauge-independent. TABC reduces the fluctuations in the computed pairing order parameter, as seen in Fig. 4, and further discussed below and in the SM. (In Ref. [57], TBC and twist averaging are shown to accelerate the extrapolation with calculations on cylinders.)

With the inclusion of a non-zero t', the perfect nesting in the Fermi surface at half-filling is absent. Subtle variations near the Fermi level from finite size and boundary conditions can have much larger effect on the formation of collective spin modes, hence there is more sensitivity in the property of the low-lying states. These states can be very close in energy such that any small finite temperature (e.g., under experimental conditions) would smear them out and render them indistinguishable. TABC provides an effective sampling of such low-lying states which can average out the fluctuations so as to more reliably capture the intrinsic properties. An illustration is given in Fig. 5. The pairing order parameter exhibits large variations as a function of the twist angle, both in the ground state and low-lying excited states, as seen in the inset for one value of h_d. The calculation can "hop" from one state to another among the bundle of low-lying states, depending on the initial condition, convergence criterion, etc, even under high-quality computational settings (e.g., large bond dimensions in DMRG). This is also reflected in the modest level of agreement between the two methods for each particular state. With TABC, however, their agreement is excellent across the entire range of h_d (which spans many level-crossings, see SM), and the two methods give fully consistent conclusions.

B. Extrapolation of pairing order

The spontaneous pairing order parameter in the TDL, Δ_d, is obtained from a massive number of computations. At each parameter set (t' and doping), $\Delta_d(N, h_d)$ is computed for many different simulation cell sizes N, at tens of h_d values, with each averaged over tens of quasi-random twist angles. We then take the limit $\Delta_d(N \to \infty, h_d)$ at each h_d, followed by the extrapolation $\Delta_d(\infty, h_d \to 0)$. The procedure is illustrated in Fig. 6. Panel (a) shows the first step, where we use fully periodic $N = L_x \times L_y$ systems with quasi-random twist angles (k_x, k_y) applied to both directions. We verify that L_x is sufficiently large such that the results have converged within our statistical accuracy. We then extrapolate the TABC results with respect to $1/L_y$, excluding small sizes. (Deviations are visible from width-4 systems, which can have different pairing symmetry from ordinary d-wave [48].) In Panel (b)

extrapolations are then performed using small h_d values (< 0.05 for linear and last 10 or so points for quadratic fits), yielding the final spontaneous pairing order parameter Δ_d at $h_d \to 0$. As can be seen, the quality of the fits is excellent; in each case, the linear and quadratic fits give consistent values within statistical errors.

IV. CONCLUSION

Can the single band Hubbard model capture the qualitative physics, particularly the superconductivity, of the cuprates? Here, more than 35 years after the discovery of the first cuprate superconductor [1], we conclude that the answer is yes, that the Hubbard model with a next near-neighbor hopping t' distinguishing between electron- and hole-doping captures the essential features of the charge, magnetic, and pairing orders.

The computed pairing order parameter in the ground state displays dome-like structures versus doping, resembling the T_c domes of the cuprates. On the hole-doped side, we find the coexistence of superconductivity with fractionally filled stripe correlations, with nominal stripe fillings in the range 0.6-0.8 in sufficiently large sizes. On the electron-doped side, at lower dopings, uniform or weakly modulated antiferromagnetism, along with uniform or weakly modulated doping, coexists with somewhat weaker superconductivity. The general appearance of stripe orders on the larger systems with non-integral numbers of pairs indicates that pairs fluctuate between stripes, promoting long-distance phase coherence and thus superconductivity; in contrast, for $t' = 0$ the stripes were filled, and superconductivity was absent [11].

This picture is in contrast to that of the t-t'-J model, once thought to be interchangeable with the Hubbard model, but which does not appear to exhibit superconductivity on the hole-doped side [43–45]. The ground states of the models are not universal, and to capture the subtle interaction of the various intertwined orders requires both very careful finite size extrapolation and very high accuracy and reliability in the simulation methods. Even within the single-band t-t' Hubbard model, an enormous body of works exists, with widely varying and often conflicting results. Our results also explain why this has been the case — the model shows extreme sensitivity of the properties to finite sizes and boundary conditions, and to any biases of approximate methods.

Here we have used the combination of DMRG and AFQMC, with DMRG benchmarking and validating the CP approximation in AFQMC on narrower systems and the AFQMC used to reach much larger systems. We have greatly improved the finite size extrapolations by using TABC. These together with methodological advances within each approach provided a powerful tool to address the question with a new level of capability and resolution.

In the models or parameter regimes on the hole-doped side where superconductivity is not present, one still finds strong indications of paired holes. For example, if holes within stripes were not paired, one would expect to find single stripes having an odd number of holes in about half the systems, but instead only even numbers of holes in each stripe are found. Whether there is superconductivity or not seems tied to the properties of a pair, e.g., its effective mass, which is strongly influenced by model parameters such as t'. A heavy pair or one which interacts strongly with the magnetic degrees of freedom of the region around it is more likely to be locked up in a stripe, suppressing phase coherence. This model-specificity and non-universality raises the question: is there any simple analytic theory of cuprate superconductivity in the style of BCS, or must we always resort to simulation?

Our study still leaves much to do in connecting the models quantitatively to experiments. We have not predicted transition temperatures, only order parameters. We have not studied transport and dynamical properties of the models. Many other properties of the one-band Hubbard model remain to be determined and understood. Other terms [58, 59] and effects not present in the Hubbard model may still play important quantitative roles. Nevertheless, it appears that qualitatively, the t-t'-U Hubbard model has "the right stuff".

V. ACKNOWLEDGMENTS

We thank A. Georges, S. Kivelson, A. J. Millis, M. Morales, H. Shi, E. Vitali, and T. Xiang for discussions. We are grateful to Lucy Reading-Ikkanda for help with graphics. M.Q acknowledges the support from the National Key Research and Development Program of MOST of China (2022YFA1405400), the National Natural Science Foundation of China (Grant No. 12274290) and the sponsorship from Yangyang Development Fund. SRW acknowledges the support of the NSF through under DMR-2110041. US acknowledges funding by the Deutsche Forschungsgemeinschaft (DFG, German Research Foundation) under Germany's Excellence Strategy-EXC-2111-390814868. H.X. thanks the Center for Computational Quantum Physics, Flatiron Institute for support and hospitality. The Flatiron Institute is a division of the Simons Foundation. C.-M.C. acknowledges the support by the Ministry of Science and Technology (MOST) under Grant No. 111-2112-M-110-006-MY3, and by the Yushan Young Scholar Program under the Ministry of Education (MOE) in Taiwan.

[1] J. G. Bednorz and K. A. Müller, Zeitschrift für Physik B Condensed Matter **64**, 189 (1986), ISSN 1431-584X, URL https://doi.org/10.1007/BF01303701.

[2] J. Hubbard, Proceedings of the Royal Society of London. Series A. Mathematical and Physical Sciences **276**, 238 (1963), URL https://royalsocietypublishing.org/doi/abs/10.1098/rspa.1963.0204.

[3] P. W. Anderson, Science **235**, 1196 (1987), URL https://www.science.org/doi/abs/10.1126/science.235.4793.1196.

[4] V. J. Emery, Phys. Rev. Lett. **58**, 2794 (1987), URL https://link.aps.org/doi/10.1103/PhysRevLett.58.2794.

[5] F. C. Zhang and T. M. Rice, Phys. Rev. B **37**, 3759 (1988), URL https://link.aps.org/doi/10.1103/PhysRevB.37.3759.

[6] P. W. Anderson and R. Schrieffer, Physics Today **44**, 54 (1991), https://doi.org/10.1063/1.881261, URL https://doi.org/10.1063/1.881261.

[7] E. Dagotto, Rev. Mod. Phys. **66**, 763 (1994), URL https://link.aps.org/doi/10.1103/RevModPhys.66.763.

[8] B. Keimer, S. A. Kivelson, M. R. Norman, S. Uchida, and J. Zaanen, Nature **518**, 179 (2015).

[9] M. Qin, T. Schäfer, S. Andergassen, P. Corboz, and E. Gull, Annual Review of Condensed Matter Physics **13**, 275 (2022), https://doi.org/10.1146/annurev-conmatphys-090921-033948, URL https://doi.org/10.1146/annurev-conmatphys-090921-033948.

[10] D. P. Arovas, E. Berg, S. A. Kivelson, and S. Raghu, Annual Review of Condensed Matter Physics **13**, 239 (2022), https://doi.org/10.1146/annurev-conmatphys-031620-102024, URL https://doi.org/10.1146/annurev-conmatphys-031620-102024.

[11] M. Qin, C.-M. Chung, H. Shi, E. Vitali, C. Hubig, U. Schollwöck, S. R. White, and S. Zhang (Simons Collaboration on the Many-Electron Problem), Phys. Rev. X **10**, 031016 (2020), URL https://link.aps.org/doi/10.1103/PhysRevX.10.031016.

[12] H.-C. Jiang and S. A. Kivelson, Proceedings of the National Academy of Sciences **119**, e2109406119 (2022), https://www.pnas.org/doi/pdf/10.1073/pnas.2109406119, URL https://www.pnas.org/doi/abs/10.1073/pnas.2109406119.

[13] S. R. White and D. J. Scalapino, Phys. Rev. Lett. **91**, 136403 (2003), URL https://link.aps.org/doi/10.1103/PhysRevLett.91.136403.

[14] E. Gull, O. Parcollet, and A. J. Millis, Phys. Rev. Lett. **110**, 216405 (2013), URL https://link.aps.org/doi/10.1103/PhysRevLett.110.216405.

[15] A. S. Darmawan, Y. Nomura, Y. Yamaji, and M. Imada, Phys. Rev. B **98**, 205132 (2018), URL https://link.aps.org/doi/10.1103/PhysRevB.98.205132.

[16] A. Himeda, T. Kato, and M. Ogata, Phys. Rev. Lett. **88**, 117001 (2002), URL https://link.aps.org/doi/10.1103/PhysRevLett.88.117001.

[17] B. Ponsioen, S. S. Chung, and P. Corboz, Phys. Rev. B **100**, 195141 (2019), URL https://link.aps.org/doi/10.1103/PhysRevB.100.195141.

[18] P. Corboz, T. M. Rice, and M. Troyer, Phys. Rev. Lett. **113**, 046402 (2014), URL https://link.aps.org/doi/10.1103/PhysRevLett.113.046402.

[19] J. P. F. LeBlanc, A. E. Antipov, F. Becca, I. W. Bulik, G. K.-L. Chan, C.-M. Chung, Y. Deng, M. Ferrero, T. M. Henderson, C. A. Jiménez-Hoyos, et al. (Simons Collaboration on the Many-Electron Problem), Phys. Rev. X **5**, 041041 (2015), URL https://link.aps.org/doi/10.1103/PhysRevX.5.041041.

[20] S. R. White, Phys. Rev. Lett. **69**, 2863 (1992), URL https://link.aps.org/doi/10.1103/PhysRevLett.69.2863.

[21] S. R. White, Phys. Rev. B **48**, 10345 (1993), URL https://link.aps.org/doi/10.1103/PhysRevB.48.10345.

[22] U. Schollwöck, Rev. Mod. Phys. **77**, 259 (2005), URL https://link.aps.org/doi/10.1103/RevModPhys.77.259.

[23] Y.-F. Jiang, J. Zaanen, T. P. Devereaux, and H.-C. Jiang, Phys. Rev. Res. **2**, 033073 (2020), URL https://link.aps.org/doi/10.1103/PhysRevResearch.2.033073.

[24] J. Jordan, R. Orús, G. Vidal, F. Verstraete, and J. I. Cirac, Phys. Rev. Lett. **101**, 250602 (2008), URL https://link.aps.org/doi/10.1103/PhysRevLett.101.250602.

[25] N. V. Prokof'ev and B. V. Svistunov, Phys. Rev. Lett. **81**, 2514 (1998), URL https://link.aps.org/doi/10.1103/PhysRevLett.81.2514.

[26] S. Zhang, J. Carlson, and J. E. Gubernatis, Phys. Rev. B **55**, 7464 (1997), URL https://link.aps.org/doi/10.1103/PhysRevB.55.7464.

[27] A. Georges, G. Kotliar, W. Krauth, and M. J. Rozenberg, Rev. Mod. Phys. **68**, 13 (1996), URL https://link.aps.org/doi/10.1103/RevModPhys.68.13.

[28] G. Knizia and G. K.-L. Chan, Phys. Rev. Lett. **109**, 186404 (2012), URL https://link.aps.org/doi/10.1103/PhysRevLett.109.186404.

[29] T. Maier, M. Jarrell, T. Pruschke, and M. H. Hettler, Rev. Mod. Phys. **77**, 1027 (2005), URL https://link.aps.org/doi/10.1103/RevModPhys.77.1027.

[30] W. Metzner, M. Salmhofer, C. Honerkamp, V. Meden, and K. Schönhammer, Rev. Mod. Phys. **84**, 299 (2012), URL https://link.aps.org/doi/10.1103/RevModPhys.84.299.

[31] C.-C. Chang and S. Zhang, Phys. Rev. B **78**, 165101 (2008), URL https://link.aps.org/doi/10.1103/PhysRevB.78.165101.

[32] M. Qin, H. Shi, and S. Zhang, Phys. Rev. B **94**, 235119 (2016), URL https://link.aps.org/doi/10.1103/PhysRevB.94.235119.

[33] B.-X. Zheng, C.-M. Chung, P. Corboz, G. Ehlers, M.-P. Qin, R. M. Noack, H. Shi, S. R. White, S. Zhang, and G. K.-L. Chan, Science **358**, 1155 (2017), ISSN 0036-8075, http://science.sciencemag.org/content/358/6367/1155.full.pdf, URL http://science.sciencemag.org/content/358/6367/1155.

[34] A. Damascelli, Z. Hussain, and Z.-X. Shen, Rev. Mod. Phys. **75**, 473 (2003), URL https://link.aps.org/doi/10.1103/RevModPhys.75.473.

[35] O. Andersen, A. Liechtenstein, O. Jepsen, and F. Paulsen, Journal of Physics and Chemistry of Solids **56**, 1573 (1995), ISSN 0022-3697, proceedings of the Conference on Spectroscopies in Novel Superconductors, URL http://www.sciencedirect.com/science/article/pii/0022369795002693.

[36] M. Hirayama, Y. Yamaji, T. Misawa, and M. Imada, Phys. Rev. B **98**, 134501 (2018), URL https://link.aps.org/doi/10.1103/PhysRevB.98.134501.

[37] A better proxy for T_c might be the magnitude of the superconducting gap. This would be more difficult to calculate, and it also is only roughly tied to T_c.

[38] V. J. Emery and S. A. Kivelson, Nature **374**, 434 (1995).

[39] D. J. Scalapino, Rev. Mod. Phys. **84**, 1383 (2012), URL https://link.aps.org/doi/10.1103/RevModPhys.84.1383.

[40] E. W. Huang, C. B. Mendl, H.-C. Jiang, B. Moritz, and T. P. Devereaux, npj Quantum Materials **3** (2018), URL https://doi.org/10.1038%2Fs41535-018-0097-0.

[41] J. M. Tranquada, B. J. Sternlieb, J. D. Axe, Y. Nakamura, and S. Uchida, Nature **375**, 561 (1995).

[42] J. M. Tranquada, Advances in Physics **69**, 437 (2020), https://doi.org/10.1080/00018732.2021.1935698, URL https://doi.org/10.1080/00018732.2021.1935698.

[43] S. Jiang, D. J. Scalapino, and S. R. White, Proceedings of the National Academy of Sciences **118**, e2109978118 (2021), https://www.pnas.org/doi/pdf/10.1073/pnas.2109978118, URL https://www.pnas.org/doi/abs/10.1073/pnas.2109978118.

[44] S. Gong, W. Zhu, and D. N. Sheng, Phys. Rev. Lett. **127**, 097003 (2021), URL https://link.aps.org/doi/10.1103/PhysRevLett.127.097003.

[45] H.-C. Jiang and S. A. Kivelson, Phys. Rev. Lett. **127**, 097002 (2021), URL https://link.aps.org/doi/10.1103/PhysRevLett.127.097002.

[46] H.-C. Jiang, S. A. Kivelson, and D.-H. Lee, *Superconducting valence bond fluid in lightly doped 8-leg t-j cylinders* (2023), URL https://arxiv.org/abs/2302.11633.

[47] H.-C. Jiang and T. P. Devereaux, Science **365**, 1424 (2019), 1806.01465.

[48] C.-M. Chung, M. Qin, S. Zhang, U. Schollwöck, and S. R. White (The Simons Collaboration on the Many-Electron Problem), Phys. Rev. B **102**, 041106 (2020), URL https://link.aps.org/doi/10.1103/PhysRevB.102.041106.

[49] C.-C. Chang and S. Zhang, Phys. Rev. Lett. **104**, 116402 (2010), URL https://link.aps.org/doi/10.1103/PhysRevLett.104.116402.

[50] H. Xu, H. Shi, E. Vitali, M. Qin, and S. Zhang, Phys. Rev. Research **4**, 013239 (2022), URL https://link.aps.org/doi/10.1103/PhysRevResearch.4.013239.

[51] S. R. White and D. J. Scalapino, Phys. Rev. B **60**, R753 (1999), URL https://link.aps.org/doi/10.1103/PhysRevB.60.R753.

[52] E. Fradkin, S. A. Kivelson, and J. M. Tranquada, Rev. Mod. Phys. **87**, 457 (2015), URL https://link.aps.org/doi/10.1103/RevModPhys.87.457.

[53] M. Fishman, S. R. White, and E. M. Stoudenmire, SciPost Phys. Codebases p. 4 (2022), URL https://scipost.org/10.21468/SciPostPhysCodeb.4.

[54] C. Hubig, F. Lachenmaier, N.-O. Linden, T. Reinhard, L. Stenzel, A. Swoboda, M. Grundner, and S. M. add other contributors here, *The* SyTen *toolkit*, URL https://syten.eu.

[55] C. Lin, F. H. Zong, and D. M. Ceperley, Phys. Rev. E **64**, 016702 (2001), URL https://link.aps.org/doi/10.1103/PhysRevE.64.016702.

[56] M. Qin, H. Shi, and S. Zhang, Phys. Rev. B **94**, 085103 (2016), URL https://link.aps.org/doi/10.1103/PhysRevB.94.085103.

[57] Y. Gannot and S. A. Kivelson, Phys. Rev. B **107**, 075127 (2023), URL https://link.aps.org/doi/10.1103/PhysRevB.107.075127.

[58] Z. Chen, Y. Wang, S. N. Rebec, T. Jia, M. Hashimoto, D. Lu, B. Moritz, R. G. Moore, T. P. Devereaux, and Z.-X. Shen, Science **373**, 1235 (2021), https://www.science.org/doi/pdf/10.1126/science.abf5174, URL https://www.science.org/doi/abs/10.1126/science.abf5174.

[59] S. Jiang, D. J. Scalapino, and S. R. White, arXiv e-prints arXiv:2303.00756 (2023), 2303.00756.

Supplementary materials for "coexistence of superconductivity with partially filled stripes in the Hubbard model"

Hao Xu,[1,*] Chia-Min Chung,[2,3,4,*] Mingpu Qin,[5] Ulrich Schollwöck,[6,7] Steven R. White,[8] and Shiwei Zhang[9]

[1]*Department of Physics, College of William and Mary, Williamsburg, Virginia 23187, USA*
[2]*Department of Physics, National Sun Yat-sen University, Kaohsiung 80424, Taiwan*
[3]*Center for Theoretical and Computational Physics, National Sun Yat-Sen University, Kaohsiung 80424, Taiwan*
[4]*Physics Division, National Center for Theoretical Sciences, Taipei 10617, Taiwan*
[5]*Key Laboratory of Artificial Structures and Quantum Control, School of Physics and Astronomy, Shanghai Jiao Tong University, Shanghai 200240, China*
[6]*Arnold Sommerfeld Center for Theoretical Physics, Ludwig-Maximilians-Universität München, 80333 Munich, Germany*
[7]*Munich Center for Quantum Science and Technology (MCQST), 80799 Munich, Germany*
[8]*Department of Physics and Astronomy, University of California, Irvine, California 92697, USA*
[9]*Center for Computational Quantum Physics, Flatiron Institute, New York, NY 10010, USA*

I. PARTIAL PARTICLE-HOLE TRANSFORMATION OF THE HUBBARD MODEL

When pairing fields are applied in the Hubbard model, the total particle number is not conserved. The usual ground-state AFQMC is formulated in the space of Slater determinant with a fixed electron number. While a more general solution is to reformulate AFQMC in Hartree-Fock-Bogoliubov (HFB) space [1], the problem here can be solved without modifying the AFQMC codes, by applying a partial particle-hole transformation [2]

$$\begin{aligned} \hat{c}_{i\uparrow} &\rightarrow \hat{d}_{i\uparrow}, \quad \hat{c}^\dagger_{i\uparrow} \rightarrow \hat{d}^\dagger_{i\uparrow} \\ \hat{c}_{i\downarrow} &\rightarrow \hat{d}^\dagger_{i\downarrow}(-1)^i, \quad \hat{c}^\dagger_{i\downarrow} \rightarrow \hat{d}_{i\downarrow}(-1)^i, \end{aligned} \tag{1}$$

where i labels the lattice sites in the bipartite lattice. With this transformation, the t' Hubbard Hamiltonian in Eq. (1) in the main text turns into

$$\begin{aligned} \hat{H} = &-t \sum_{\langle i,j\rangle\sigma} \hat{d}^\dagger_{i\sigma}\hat{d}_{j\sigma} - t' \sum_{\langle\langle i,j\rangle\rangle\sigma} s(\sigma)\hat{d}^\dagger_{i\sigma}\hat{d}_{j\sigma} \\ &+U\sum_i(\hat{m}_{i\uparrow} - \hat{m}_{i\downarrow}\hat{m}_{i\uparrow}) - \mu\sum_i(\hat{m}_{i\uparrow} + 1 - \hat{m}_{i\downarrow}), \end{aligned} \tag{2}$$

where $s(\uparrow) = +1$ and $s(\downarrow) = -1$, and $\hat{m}_{i,\sigma} = \hat{d}^\dagger_{i,\sigma}\hat{d}_{i,\sigma}$. Note that the next near-neighbor hopping changes sign for down spins after the transformation. The pairing operator $\hat{\Delta}_{ij} = (\hat{c}_{i\uparrow}\hat{c}_{j\downarrow} - \hat{c}_{i\downarrow}\hat{c}_{j\uparrow})/\sqrt{2}$ is transformed to:

$$\hat{\Delta}_{ij} = ((-1)^{j+1}\hat{d}^\dagger_{j\downarrow}\hat{d}_{i\uparrow} - (-1)^i\hat{d}^\dagger_{i\downarrow}\hat{d}_{j\uparrow}))/\sqrt{2} \tag{3}$$

which is now a spin-flip hopping term. The sign of U is reversed, meaning the interaction turns to attractive. Up and down electron now acquire effective chemical potentials $\mu - U$ and $-\mu$, respectively, which means $\langle\sum_i(\hat{m}_{i\uparrow}\rangle \neq \langle\sum_i(\hat{m}_{i\downarrow}\rangle$. After the transformation we have

$$\sum_i(\hat{m}_{i\uparrow} + \hat{m}_{i\downarrow}) = \sum_i(\hat{n}_{i\uparrow} + 1 - \hat{n}_{i\downarrow}) = N_s, \tag{4}$$

such that the total number of electrons equals the number of sites, i.e., the system is at half-filling but with spin imbalance. The random walkers (Slater determinants) are now represented as $2N \times N_e$ matrix [3] in the AFQMC calculation, and each orbital in the Slater determinant is now a spin-orbital with a mixture of up and down components.

II. TWIST BOUNDARY CONDITIONS

Twist boundary conditions (TBC) in x-direction means the wave-function satisfies:

$$\psi(\mathbf{r}_1 + L\hat{e}_x, \mathbf{r}_2, \cdots, \mathbf{r}_N) = e^{i\theta_x}\psi(\mathbf{r}_1, \mathbf{r}_2, \cdots, \mathbf{r}_N). \tag{5}$$

For convenience we have used L to denote L_x, the linear dimension of the periodic cell in x-direction. (The definitions of TBC in other directions are similar). For the two dimensional systems studied in this work, the phases for the two directions are independent of each other, and the phase factors from x- and y-directions are multiplicative. Thus, with no loss of generality, we will only explicitly write out one dimension (x) below. We will assume that the lattice sites are labeled from 1 to L.

Different gauges can be adopted to realize TBC. We discuss two common choices here. In gauge A, an electron picks up a phase only when it crosses the boundary, while in gauge B, the phase is split over all bonds evenly.

A. Gauge A

In gauge A, if we apply the same twist for $\uparrow$ and $\downarrow$-spins in the repulsive Hubbard model, we have

$$\begin{aligned} c^\dagger_{L+1,\sigma} &= \exp(i\theta)c^\dagger_{1,\sigma} \\ c_{L+1,\sigma} &= \exp(-i\theta)c_{1,\sigma} \end{aligned} \tag{6}$$

*These two authors contributed equally to this work.

So the hopping between the last and first site is modified as

$$-t\hat{c}^\dagger_{1\sigma}\hat{c}_{L\sigma} + h.c \rightarrow -t\exp(i\theta)\hat{c}^\dagger_{1\sigma}\hat{c}_{L\sigma} + h.c \quad (7)$$

while the other hopping terms remains unchanged. After the partial particle-hole transformation in Eq. (1), the spin up term is unchanged, but the phase for down spin changes to $-\theta$ as

$$-t\exp(-i\theta)\hat{d}^\dagger_{1\downarrow}\hat{d}_{L\downarrow} + h.c \quad (8)$$

The same is true for the t' term.

With TBC, we also need to modify the definition of the pairing operator ($\hat{\Delta}_{kj} = (\hat{c}_{k\uparrow}\hat{c}_{j\downarrow} - \hat{c}_{k\downarrow}\hat{c}_{j\uparrow})/\sqrt{2}$, for bonds connecting nearest-neighbor sites, $\langle jk\rangle$) for the bond connecting the first and last site as

$$\hat{\Delta}_{1L} = \exp(-i\theta)(\hat{c}_{1\uparrow}\hat{c}_{L\downarrow} - \hat{c}_{1\downarrow}\hat{c}_{L\uparrow})/\sqrt{2}\,. \quad (9)$$

When applying the pairing field to calculate the pairing order, we need to include the phase in Eq. (9) when twist boundary conditions are imposed. In the AFQMC calculation, the pairing operator in Eq. (9) can be transformed, following Eq. (1), as

$$\hat{\Delta}_{1L} = \exp(-i\theta)(\hat{d}^\dagger_{1\downarrow}\hat{d}_{L\uparrow} - (-1)^L\hat{d}^\dagger_{L\downarrow}\hat{d}_{1\uparrow})/\sqrt{2} \quad (10)$$

Other pairing terms are transformed to the $-U$ case following Eq. (3)

B. Gauge B

We next consider gauge B in a similar setup to Gauge A. Now the phase is spread evenly over each bond and we have, for the repulsive model

$$\begin{aligned} c^\dagger_{j\sigma} &\rightarrow c^\dagger_{j\sigma}\exp(i(j-1)\frac{\theta}{L}) \\ c_{j\sigma} &\rightarrow c_{j\sigma}\exp(-i(j-1)\frac{\theta}{L}) \end{aligned} \quad (11)$$

and

$$\begin{aligned} c^\dagger_{L+1,\sigma} &= \exp(i\theta)c^\dagger_{1,\sigma} \\ c_{L+1,\sigma} &= \exp(-i\theta)c_{1,\sigma} \end{aligned} \quad (12)$$

The nearest neighbor hopping term is then modified to

$$-t\sum_j \exp(i\theta/L)\hat{c}^\dagger_{j+1\sigma}\hat{c}_{j\sigma} + h.c. \quad (13)$$

The t' term has similar form.

The pairing operator $\hat{\Delta}_{kj} = (\hat{c}_{k\uparrow}\hat{c}_{j\downarrow} - \hat{c}_{k\downarrow}\hat{c}_{j\uparrow})/\sqrt{2}$ is modified as

$$\hat{\Delta}_{kj} = (\hat{c}_{k\uparrow}\hat{c}_{j\downarrow} - \hat{c}_{k\downarrow}\hat{c}_{j\uparrow})\exp(-i(k+j-2)\theta/L)/\sqrt{2} \quad (14)$$

For the bond connecting the first and last site, we have

$$\hat{\Delta}_{L,1} = (\hat{c}_{L\uparrow}\hat{c}_{1\downarrow} - \hat{c}_{1\downarrow}\hat{c}_{L\uparrow})\exp(-i(2L-1)\theta/L)/\sqrt{2} \quad (15)$$

We can then follow the particle-hole transformation in Eq. (1) to transform the definition of pairing order to the negative U model, which is used in the AFQMC calculation.

C. The equivalence of the two gauges

The two gauges discussed above are equivalent and physical quantities should have the same values under them, which we have explicitly verified. Since the interaction term is independent of the twist angle, it is convenient to test the TBC implementation in non-interacting systems. For example, in a 20×4 lattice with $t' = -0.2t$, $\mu = 0.8$, and twist angle $\theta_x = 1.2994\pi, \theta_y = 0.6026\pi$, it is easily checked in all our codes that physical quantities, such as the energy per site (-1.15861112), average pairing order per bond (0.01108939), and the electron density (0.82422077), are all exactly the same under the two gauges.

III. SELF-CONSISTENT CONSTRAINT IN AFQMC

We apply magnetic and pairing pinning fields to probe the corresponding response in the studied systems. A self-consistent procedure in AFQMC allows us to apply a constraint to remove the sign problem. We describe the pinning field calculations and the self-consistency procedure below.

The magnetic pinning fields are typically applied in cylindrical cells, to one or both ends of the cylinder, not in the rest of the cell. We try different configurations of the magnetic pinning fields to probe the possible magnetic order or correlation. The strength of the fields is fixed at $h_m = 0.25$, and limited to only the edge(s) of the cylinder. For most of the systems, we applied anti-ferromagnetic pinning fields at the open edges of the studied cylinders ($(-1)^{(i_x+i_y)}h_m$ for $i_x = 1$ and L_x). In some cases, we also test a pinning field configuration with a π phase to the pinning magnetic fields on the right edge as ($(-1)^{(i_x+i_y)}h_m$ for $i_x = 1$ and $(-1)^{(i_x+i_y+1)}h_m$ for $i_x = L_x$), and compare the energies to determine the true ground state, the one with the lower energy. Note that it is important in this scheme to examine progressively larger (longer) systems, in order to remove the effect of the local pinning field. Ref. [4] includes further details of our analysis method and how we extract information in the TDL.

To compute the pairing order parameter, we apply global pairing fields across the entire simulation cell, similar to Ref. [2]. To probe the d-wave pairing response the applied pair-inducing fields on vertical and horizontal bonds have the same strength h_d but opposite signs. The Hamiltonian with pairing fields is

$$\hat{H}'(h_d) = \hat{H} + \hat{H}_d(h_d) \quad (16)$$

where

$$\hat{H}_d(h_d) = -h_d\sum_{\langle i,j\rangle} b_{ij}\frac{\hat{\Delta}_{ij} + \hat{\Delta}^\dagger_{ij}}{2}\,, \quad (17)$$

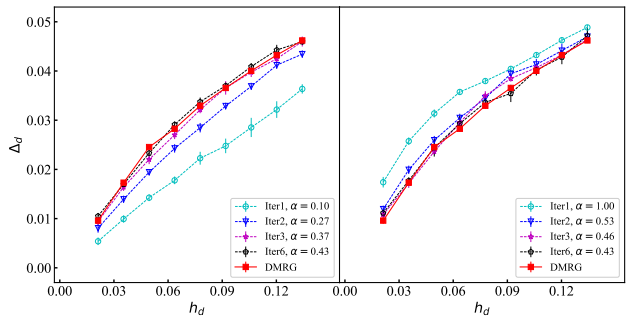

FIG. 1: Robustness of the self-consistent constraint in AFQMC. An example is shown for the pairing order parameter in the 1/4 hole-doped Hubbard model on a 16×4 cylinder. On the left panel, the self-consistent calculation starts with an initial value of $\alpha = 0.1$. The calculation converges with a handful or iterations to the exact result (DMRG, red) in this system, with a converged value $\alpha = 0.43$. On the right panel, the calculation is initialized with $\alpha = 1.0$, and converges from the opposite direction to the same result.

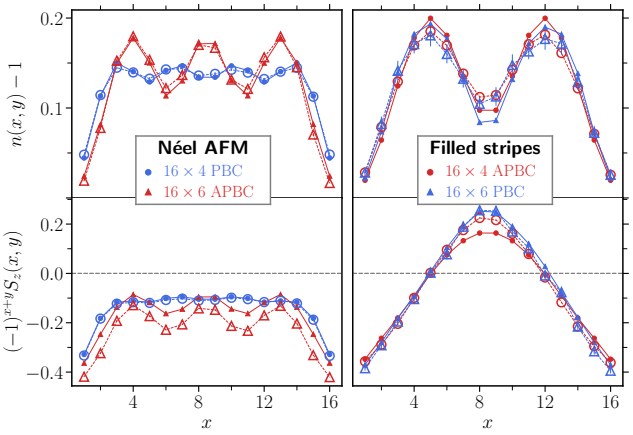

FIG. 2: Strong sensitivity of the spin and charge orders to system sizes and boundary conditions. Here we show results for four different systems, all with the same bulk parameters ($\delta = 1/8$, electron doped), but different in size and boundary conditions. Line cuts of the doped electron density (top panels) and staggered spin density (bottom) are shown, with combinations of two system sizes, 16×4 and 16×6, and periodic (PBC) and antiperiodic (APBC) boundary conditions. Antiferromagnetic pinning fields have been applied at the left and right edges of the open cylinders. Two distinct types of states appear, Néel AFM with fairly uniform electron densities (left panels), and filled stripe states (right panels). Good agreement is found between DMRG (filled symbols) and AFQMC (empty symbols); the differences are tied to the sizes and boundary conditions.

where $b_{ij} = +1$ for a bond connecting two nearest-neighbors i and j in the x-direction and $b_{ij} = -1$ if $\langle ij\rangle$ is in the y-direction.

The pairing order is calculated from the derivative of the ground state energy $E'(h_d)$ with respect to h_d, following the Hellmann-Feynman theorem. Recall these calculations are performed in the particle-hole-transformed attractive Hubbard Hamiltonian in Eq. (2). We take the ground state of the non-interacting Hamiltonian ($U = 0$ in Eq. (2)) with the pairing field αh_d as trial wave function, where α is a parameter to be determined in the self-consistent iterations. In the first step, we choose an arbitrary α and calculate the average value of pairing order with AFQMC using the corresponding trial wave function as a constraint. We then tune the value of α by minimizing the difference between the pairing orders given by the non-interacting wave-function and the previous iteration of AFQMC. We then carry out the next iteration AFQMC calculation with the new trial wave-function. This process is repeated until α is converged. In each mean-field solution we tune the value of chemical potential to target the desired spin imbalance (i.e., the electron density in the repulsive model). In performing TABC, we determine the final value of α via averaging over different twist angles. The value is found to converge quickly, so a small set of pilot calculations can be performed first to obtain a good estimate. More computations can be added if further precision is needed.

In Fig. 1, we show the computed pairing order in the self-consistent process for the 1/4 hole doped t' Hubbard model on a 16×4 cylinder. DMRG results are also shown, because for this narrow system, it provides a reference result which is essentially exact. In Fig. 1, we start the self-consistent calculation with an initial value $\alpha = 0.1$ (the left panel). After 6 iterations, the pairing order converges to the DMRG results. The converged value of α is $\alpha = 0.43$. We also obtain the same converged pairing order and α value by starting the self-consistent process with $\alpha = 1.0$ (the right panel), indicating the self-consistent calculation is independent of the initial value of α.

IV. SENSITIVITY OF ORDER TO SYSTEM SIZES AND BOUNDARY CONDITIONS

In Fig. 2 we show an example of the strong sensitivity of the ground states to system sizes and boundary conditions (BCs). Two entirely different ground states are obtained for the same physical parameters from four different combinations of size/BCs, with an alternation between the effects of size versus BC. Consistent results are seen from both methods. This sort of sensitivity is also observed on the hole-doped side (see Fig. 4). To determine the order in the thermodynamic limit in these systems thus requires computations in significantly larger sizes than has been previously reached. Below, we also show the presence of numerous low-lying states whose ordering in energy can be affected by size and BCs. In many cases these low-lying states can be tied to different stripe configurations. In the case of Fig. 2, the system may be close to a phase boundary between the two types of states[5]. The twist-averaging procedure

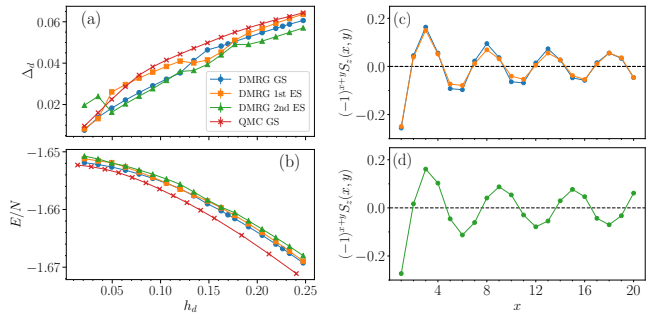

FIG. 3: Illustration of low-lying states and level-crossing. The pairing order Δ_d (a) and energy per site (b) are shown as functions of the global pairing field strength h_d for a 1/5 hole doped system in a 20×4 cylinder. The error bars are smaller than the symbol sizes. In (c) and (d) the staggered spin densities are shown along the x direction for the three low-lying states from DMRG, for $h_d \approx 0.0075$, the smallest h_d we consider. The AF magnetic pinning fields are applied at the left open edge.

adopted here tends to average over the various states, which allows better extrapolation to the TDL compared to earlier approaches[6].

V. LEVEL CROSSING WITH APPLIED PAIRING FIELDS

In addition to the enhanced sensitivity of the ground state to the boundary conditions and system sizes in the t' Hubbard model, the evolution of the ground state with the strength of the applied pairing field is subtle, and creates another computational challenge. In Fig. 3 (a) and (b), as an example, we show the evolution of a few low-lying states as a function of h_d, in a 20×4 system at 1/5 hole doping. As h_d decreases, the low-lying states, which are separated by tiny energy differences (note the small energy scale in b), exhibit crossovers between several branches. The different branches are characterized by different numbers of stripes in the states, as shown in Fig. 3 (c) and (d). That d-wave pairing field induces strong level crossings is another indication of the intimate connection between the fluctuation of the stripe state and superconductivity in the system. As mentioned, such level-crossings make the comparisons between DMRG and AFQMC more challenging, as each calculation is often sensitive to even small variations in the calculational parameters. However this effect is reduced by employing twist averaging, in which all the low-lying states are sampled. As can be seen in Fig. 5 in the main text, TABC effectively treats the crossovers as a function of h_d, which results in smooth curves, and DMRG and AFQMC agree very well.

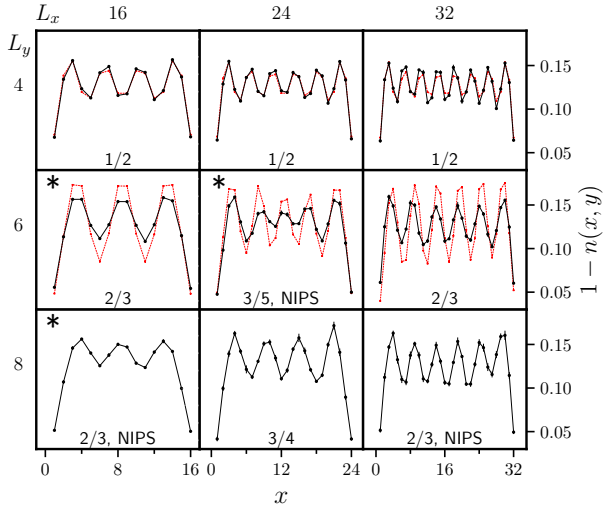

FIG. 4: Hole density for the systems in Fig. 2 in the main text for 1/8 hole doping. The evolution of the stripe patterns is shown versus system size. The hole densities are shown as linecuts along the length of the cylinders. The length of the cylinder (L_x) is varied across the three columns and the width (L_y) across rows. AFM pinning fields are applied at the two edges of the cylinder ($x = 1$ and $x = L_x$), either in phase or with a π-phase shift (marked by an asterisk); the one with lower energy is shown. The filling fraction f of each stripe pattern is indicated, with NIPS denoting non integer-pair stripes. DMRG results (red) are shown for width-4 and 6 systems, and AFQMC (black) are in good agreement with them.

VI. SUPPLEMENTAL DATA

A. Hole density for 1/8 hole doped systems

In Fig. 4, we show the hole density for the systems in Fig. 2 in the main text. For systems with width 4 and 6, for which DMRG is available, we find good agreement between AFQMC amd DMRG results. In width-6 systems, the discrepancies are somewhat larger in the density here compared to the spin in Fig. 2 in the main text. This is likely because of a combination of two factors. First AFQMC has shown in $t' = 0$ Hubbard model a slight tendency to under-estimate the amplitude of the density fluctuations in stripes [4, 7]. Second, in some cases we have seen indications that the DMRG may not have reached full convergence in width-6 systems, even with the very large bond dimensions we were able to do.

B. Additional data on pairing order parameter

In this subsection, we include the finite size data for the pairing order, as well as the extrapolation process to obtain the spontaneous pairing order in the thermodynamic limit which is plotted in Fig. 1 in the main text.

1. Electron doped region

In Figs. 5, 6, and 7 we present the data for pairing order in the electron-doped region, with $\delta = 1/8, 1/5$, and $1/3$ respectively. As discussed in the main text, we use fully periodic systems (i.e., torus simulations cells of $L_x \times L_y$) and perform TABC with quasi-random twists. We have verified that the results have converged with respect to L_x to within our statistical error. When extrapolating the pairing orders with width of the system, we omit width-4 systems. When extrapolating the TDL values versus h_d, we perform both linear and quadratic fits. In the linear fits, we use $h_d < 0.05$, when the data is clearly in the linear response regime. In the quadratic fits, we include more data points, 10-12 values of h_d. We find that the resulting extrapolated $\Delta_d(h_d \to 0)$ values are often indistinguishable. When there is a difference, the result from the better fit (smaller χ^2) is used. The final pairing order at TDL is $0.007(3), 0.007(4)$, and $0.000(2)$ for $\delta = 1/8, 1/5$, and $1/3$, respectively, as reported in Fig. 1 in the main text.

2. Hole doped region

In Figs. 8, 9, 10, and 11 we present the data for pairing order in the hole-doped region, with $\delta = 1/8, 1/5, 1/4$, and $1/3$ respectively. The final pairing order at TDL for $\delta = 1/8, 1/5, 1/4$, and $1/3$ are $0.017(3), 0.016(2), 0.007(3)$, and $0.002(3)$, as shown in Fig. 1 in the main text.

[1] H. Shi and S. Zhang, Phys. Rev. B **95**, 045144 (2017), URL https://link.aps.org/doi/10.1103/PhysRevB.95.045144.

[2] M. Qin, C.-M. Chung, H. Shi, E. Vitali, C. Hubig, U. Schollwöck, S. R. White, and S. Zhang (Simons Collaboration on the Many-Electron Problem), Phys. Rev. X **10**, 031016 (2020), URL https://link.aps.org/doi/10.1103/PhysRevX.10.031016.

[3] M. Qin, H. Shi, and S. Zhang, Phys. Rev. B **94**, 085103 (2016), URL https://link.aps.org/doi/10.1103/PhysRevB.94.085103.

[4] H. Xu, H. Shi, E. Vitali, M. Qin, and S. Zhang, Phys. Rev. Research **4**, 013239 (2022), URL https://link.aps.org/doi/10.1103/PhysRevResearch.4.013239.

[5] S. Jiang, D. J. Scalapino, and S. R. White, Proceedings of the National Academy of Sciences **118**, e2109978118 (2021), https://www.pnas.org/doi/pdf/10.1073/pnas.2109978118, URL https://www.pnas.org/doi/abs/10.1073/pnas.2109978118.

[6] H.-C. Jiang and T. P. Devereaux, Science **365**, 1424 (2019), 1806.01465.

[7] M. Qin, H. Shi, and S. Zhang, Phys. Rev. B **94**, 235119 (2016), URL https://link.aps.org/doi/10.1103/PhysRevB.94.235119.

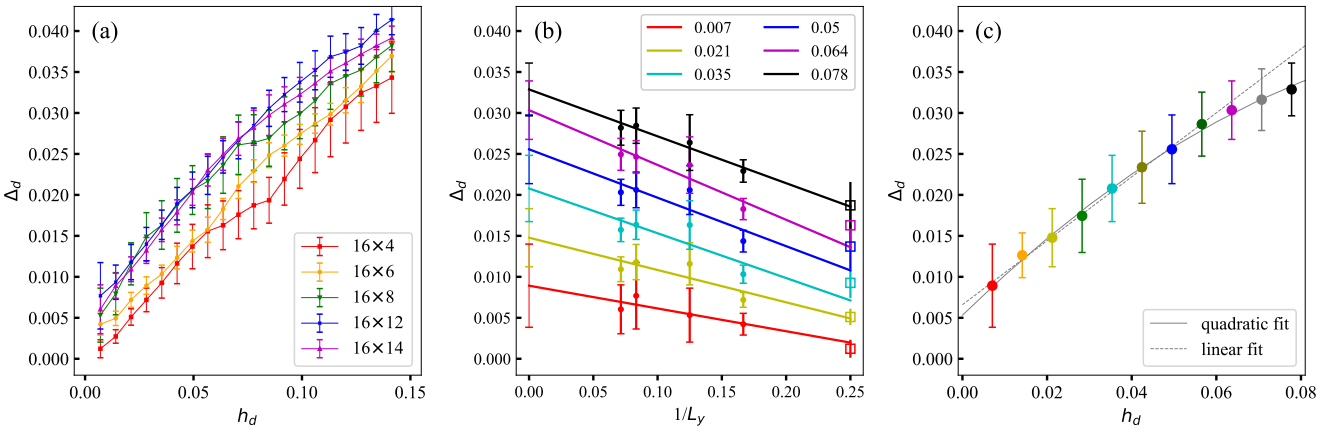

FIG. 5: The extrapolation of pairing order for 1/8 electron doping. (a) shows the pairing order parameter versus pairing field for different system sizes. The data for each torus of $L_x \times L_y$ is obtained from TABC with quasi-random twists (k_x, k_y). The number of twists is a few dozens for smaller systems and about a dozen for the larger systems. (b) shows extrapolation of the pairing order with the width of the system for each fixed pairing field. In (c) the extrapolated value in (b) is plotted against pairing field and then an extrapolation of the pairing field to $h_d \to 0$ gives the spontaneous pairing order at thermodynamic limit. Both linear and quadratic fits give consistent results.

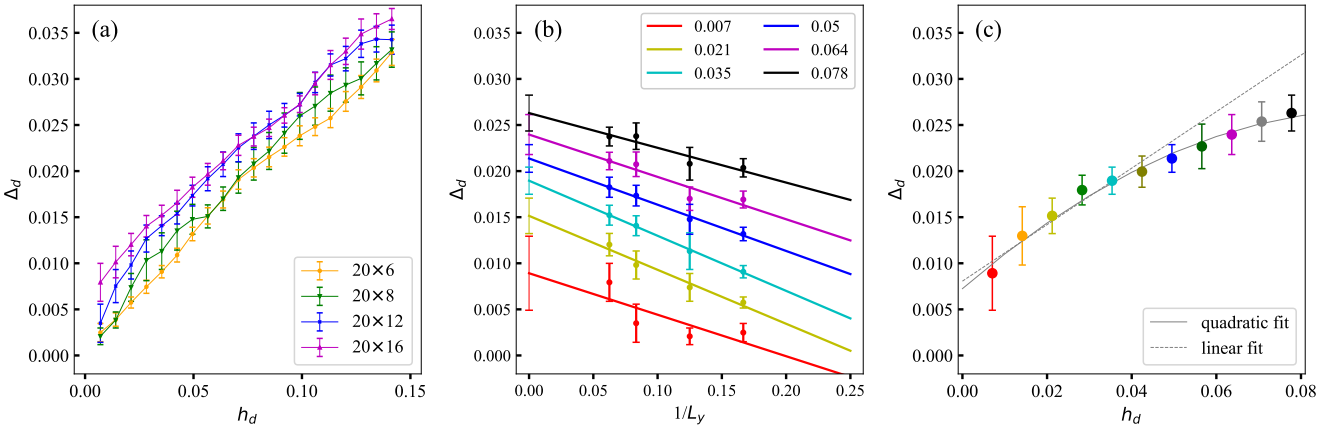

FIG. 6: Similar as Fig. 5 but for 1/5 electron doping.

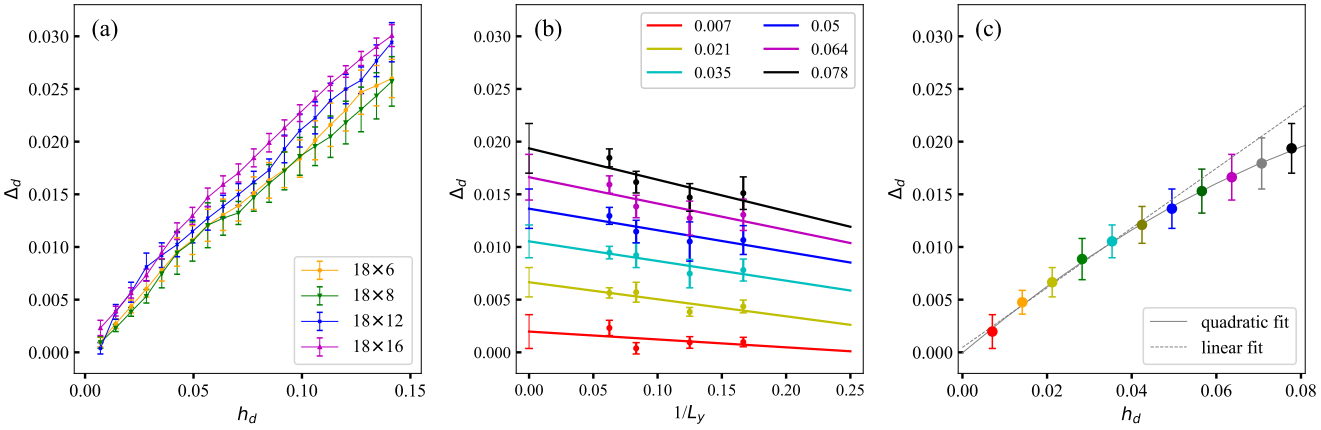

FIG. 7: Similar as Fig. 5 but for 1/3 electron doping.

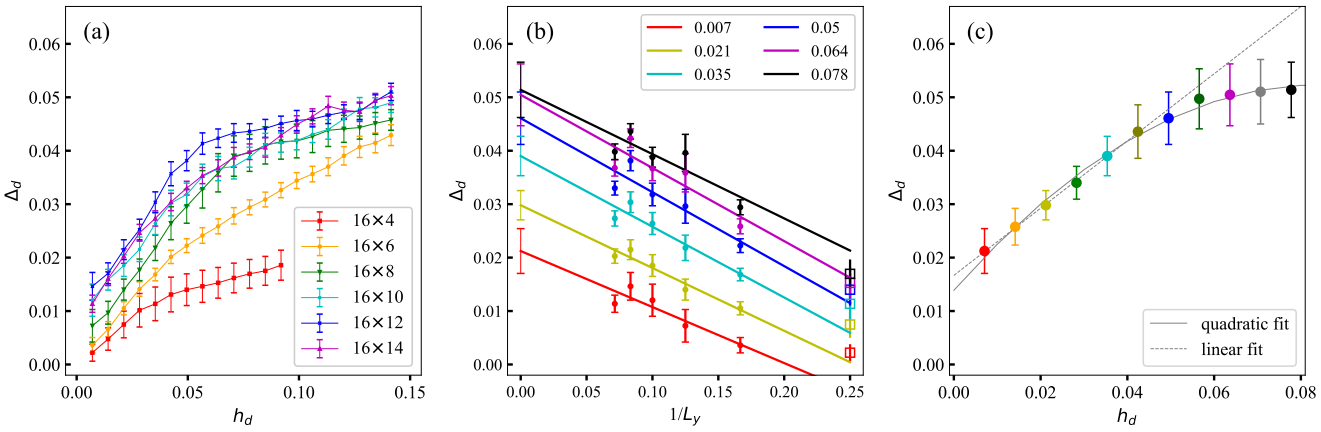

FIG. 8: Similar as Fig. 5 but for 1/8 hole doping.

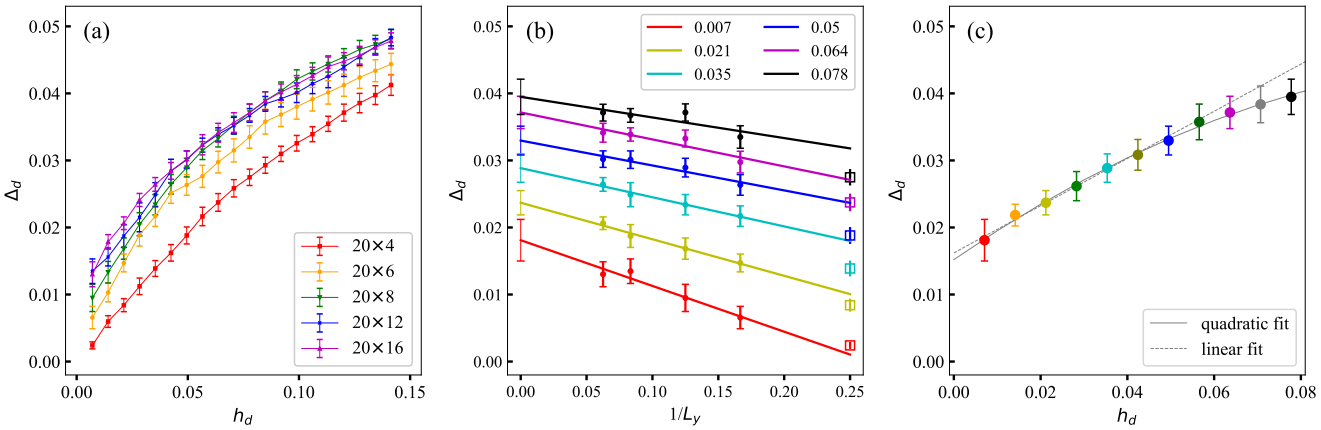

FIG. 9: Similar as Fig. 5 but for 1/5 hole doping.

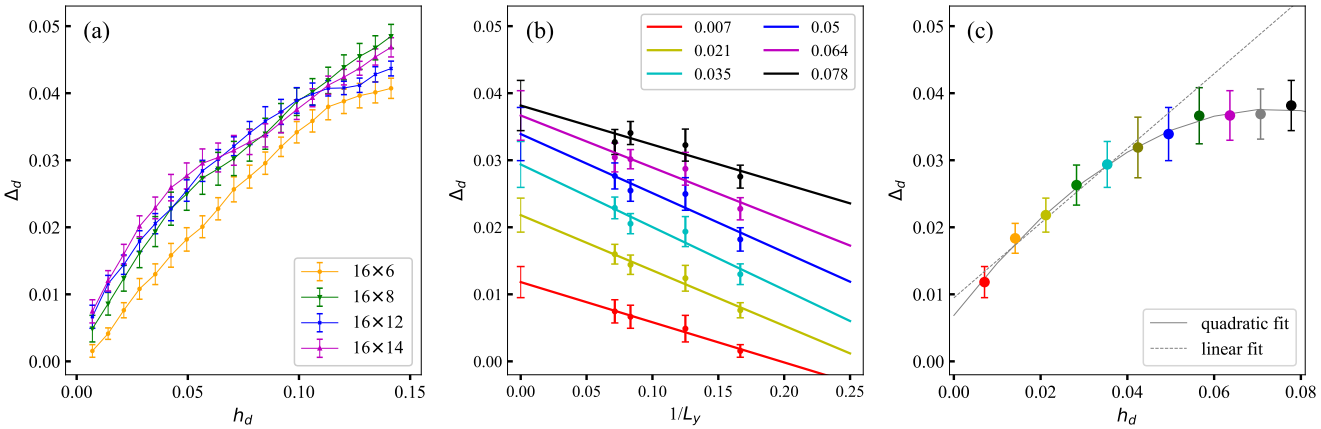

FIG. 10: Similar as Fig. 5 but for 1/4 hole doping.

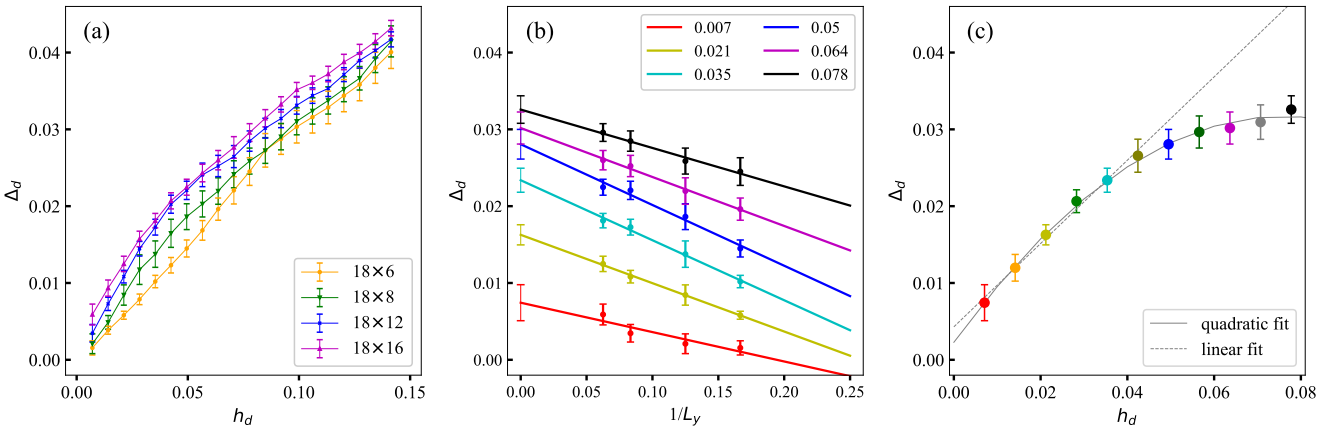

FIG. 11: Similar as Fig. 5 but for 1/3 hole doping.

Simulations of the dynamics of quantum impurity problems with matrix product states

Matteo M. Wauters,[1] Chia-Min Chung,[2,3,4] Lorenzo Maffi,[1] and Michele Burrello[1]

[1] *Niels Bohr International Academy and Center for Quantum Devices, Niels Bohr Institute, Copenhagen University, Universitetsparken 5, 2100 Copenhagen, Denmark*
[2] *Department of Physics, National Sun Yat-sen University, Kaohsiung 80424, Taiwan*
[3] *Center for Theoretical and Computational Physics, National Sun Yat-Sen University, Kaohsiung 80424, Taiwan*
[4] *Physics Division, National Center for Theoretical Sciences, Taipei 10617, Taiwan*

The Anderson impurity model is a paradigmatic example in the study of strongly correlated quantum systems and describes an interacting quantum dot coupled to electronic leads. In this work, we characterize the emergence of the Kondo effect by investigating the model dynamics following a quantum quench based on matrix product state simulations. The relaxation of the impurity magnetization allows for the estimate of the predicted universal scaling of the Kondo temperature as a function of the impurity-lead hybridization and quantum dot repulsion. Additionally, our simulations permit us to evaluate the current in the nonequilibrium quasi-steady state appearing after the quench. Through their values, we examine the dependence of the conductance on the voltage bias V_b and on the impurity chemical potential V_g, which displays a zero-bias Kondo peak. Our results are relevant for transport measurements in Coulomb blockaded devices, and, in particular, in quantum dots induced in nanowires.

Introduction. The Kondo effect is the most emblematic embodiment of strong correlations in condensed matter systems. The advances in the fabrication and measurement techniques of nanostructures allowed us to observe its distinctive zero-bias conductance peak in a wide class of systems, including gate-defined quantum dots [1, 2], nanotubes [3] and semiconducting nanowires [4].

In these mesoscopic systems, however, the dynamics of the quantum impurities at the basis of the Kondo effect is typically too fast to be observed. A complementary experimental platform has been recently offered by quantum simulators of ultracold fermionic Yb atoms [5]. In these setups, the characteristic time scales are much longer than in their solid state counterpart, thus enabling the analysis of the dynamics of the spin impurities at the basis of the Kondo effect in out-of-equilibrium transient states [6].

Inspired by these developments, in this work we analyze the dynamics of the Anderson impurity model after a quantum quench through matrix product state (MPS) simulations. By studying the transient behavior of its impurity magnetization, we provide a numerical verification of the Kondo time scale consistent with previous renormalization group results [7]. We derive the conductance of the corresponding two-terminal problem, relevant for the experimental study of Coulomb blockaded nanowires with induced quantum dots.

The out-of-equilibrium properties of quantum impurity models following quantum quenches are considered a paradigmatic playground to observe how strong correlations develop through time evolution in many-body quantum systems and have been recently studied by means of a vast set of analytical and numerical techniques [8–18]. In the following we will apply the MPS algorithm described in Ref. [19] to simulate the time evolution of the two-terminal Anderson impurity model (AIM).

The model. The AIM represents an electronic environment coupled with an interacting magnetic impurity; it is one of the most popular yet simple models that display the Kondo effect, and it constitutes the central element of dynamical mean field theory methods for studying correlated materials, making it a fundamental problem for many numerical algorithms [20]. Its Hamiltonian reads

$$\widehat{H} = \widehat{H}_{\text{leads}} + \widehat{H}_{\text{tunn}} + \widehat{H}_{\text{AIM}} \,, \tag{1}$$

where

$$\widehat{H}_{\text{AIM}} = U\hat{n}_\uparrow\hat{n}_\downarrow + V_g(\hat{n}_\uparrow + \hat{n}_\downarrow) \,, \tag{2}$$

with $\hat{n}_\sigma = \hat{d}^\dagger_\sigma \hat{d}_\sigma$ describing the occupation of the two spin states of a single-level quantum dot, which, in turn, plays the role of the magnetic impurity and is characterized by the Hubbard repulsion U and the chemical potential V_g. Unless otherwise stated, we will focus on the particle-hole symmetric point $V_g = -0.5U$.

The lead Hamiltonian

$$\widehat{H}_{\text{leads}} = -\sum_{\alpha,\sigma,l} t_{\alpha,\sigma,l}\left(\hat{c}^\dagger_{\alpha,\sigma,l}\hat{c}_{\alpha,\sigma,l} + \text{H.c.}\right) + \sum_{\alpha,\sigma,l}\mu_{\alpha,\sigma}\hat{n}_{\alpha,\sigma,l} \tag{3}$$

describes two spinful fermionic chains ($\alpha = L, R$) with a spin-dependent chemical potential $\mu_{\alpha,\sigma}$ and a hopping amplitude $t_l = t_0 \mathrm{e}^{-(l-1)/\xi}$ that decreases exponentially as a function of the distance from the site $l = 1$, with a decay length ξ. This is known as Wilson construction and it is commonly used in numerical renormalization group approaches to impurity problems. Moreover, it has been shown effective to increase both the resolution at small voltage bias, namely by mimicking an effectively larger system, and the stability of the time evolution in MPS simulation of transport problems [8, 19]. Indeed,

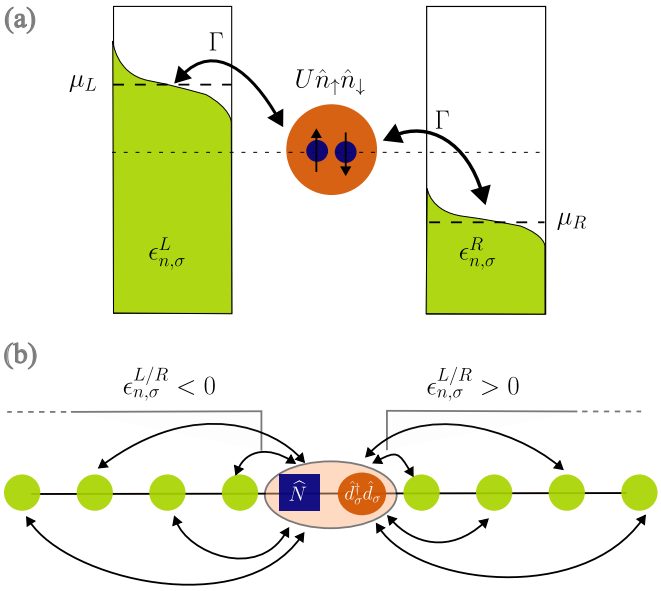

Figure 1. (a) Sketch of the AIM: a single-level quantum dot with Hubbard repulsion U is tunnel-coupled to two non-interacting leads with chemical potentials μ_L and μ_R. (b) Schematic representation of the MPS describing the system [19]. The sites of the chain represent single-particle orbitals and are ordered by their energy. To account for the interaction, we include an auxiliary bosonic charge site (represented by a square) which counts the number of particles inside the dot. This construction introduces long-range couplings (arrows) in the Hamiltonian MPO, which however do not constitute an obstacle for the TDVP algorithm used for the time evolution.

given the finite size L, the density of states around the Fermi energy depends on the hopping decay length ξ: the smaller ξ, the more states are shifted toward the Fermi energy, leading to a smaller energy level spacing. Therefore, a strong decay of the tunneling provides higher energy resolution to accurately determine the dynamics for states close to zero energy (thus at small bias voltages)[8].

Finally, the quantum dot and the leads are coupled with a standard tunneling Hamiltonian

$$\widehat{H}_{\rm tunn} = -\sum_{\alpha,\sigma} J_{\alpha,\sigma}\left(\hat{c}^\dagger_{\alpha,\sigma,1}\hat{d}_\sigma + \text{H.c.}\right) \ , \qquad (4)$$

where $\hat{d}_\sigma$ destroys an electron with spin σ on the impurity level. Throughout this paper, we consider a uniform tunneling strength between the quantum dot and the leads $J_{\alpha,\sigma} = J$ and we denote by $\Gamma = 2J^2/t_0$ the effective tunneling rate in the limit of infinite bandwidth (constant density of states).

To bring the system out of equilibrium, we adopt two different quantum quench protocols [19, 21]: *(i)* in the *zero-bias quench*, we initialize the system with $J = 0$ and $\mu_L = \mu_R$, thus preparing a product state between the impurity and the leads; at time $\mathrm{t} > 0$, the leads are connected to the quantum dot ($J > 0$) and the system equilibrates towards a stationary state. *(ii)* in the $\mu-$*quench*, the system is initialized in the ground state at half filling, i.e. with uniform chemical potential $\mu_L = \mu_R$, and then it evolves in time after a voltage bias is turned on. The first protocol is more useful to study the relaxation of the impurity magnetization and extract the Kondo temperature, while the second leads to a fast convergence of the current to a nonequilibrium quasi-steady state. Indeed, in the μ-quench the initial state already captures some of the non-perturbative Kondo correlations and therefore is closer to the Kondo-like quasi-steady state that arises in transport measurements.

Matrix product state simulations. Tensor networks offer a powerful framework to simulate the real-time evolution of quantum impurity models [8, 9, 11–13, 15, 17, 18]. To simulate the post-quench dynamics, we model the system with the MPS depicted in Fig. 1(b): each site represents a single-particle *energy* orbital of the non-interacting and decoupled system ($U, J = 0$), and we compute the unitary time evolution of the closed system with the time-dependent variational principle (TDVP) [22, 23]. In particular, we expand the construction presented in Ref. [19] with the addition of the spin degrees of freedom; the MPS "sites" are ordered based on their energies [24], such that the entropy growth during the time evolution is restricted in an energy window, thus a segment of the MPS, corresponding to the voltage bias. Since the basis states (MPS "site") are ordered by their energies regardless the number of leads, introducing multiple leads (or the spin degrees of freedom) is straightforward.

The interaction U is introduced by including an auxiliary MPS site that represents the charge $\widehat{N} = \hat{n}_\uparrow + \hat{n}_\downarrow$ of the dot [19]. Tunneling events increase or decrease this charge by one. This construction is not strictly necessary for a single impurity site as in the AIM in Eq. (1), but it can easily allow for generalizations to multilevel dots with a uniform all-to-all Coulomb repulsion described by an effective charging energy.

In the chosen single-particle eigenstate basis, the dynamics is dictated only by the tunneling Hamiltonian coupling the leads with the quantum dot. $\widehat{H}_{\rm tunn}$ is non-local in this basis, but it can be described by a matrix product operator (MPO) with limited bond dimension, such that TDVP is not hampered by the presence of these long-range interactions and can be efficiently used to simulate the dynamics for long evolution time.

The method is implemented by using ITensor library [25]. The source code can be found in Ref. [26].

Results. We first focus on the equilibration of the impurity after it is coupled to the *unbiased* leads (zero-bias quench). and here we set bias to zero ($\mu_L = \mu_R$).) The dynamics of the impurity magnetization is predicted to be characterized by two rates [27]: Γ, which determines the short-time and nonuniversal evolution; and the Kondo temperature T_K, whose inverse, the Kondo time $\mathrm{t}_K = T_K^{-1}$, defines the time scale required for the formation of the Kondo screening cloud. In the renormalization group sense, the evolution for time $\Gamma^{-1} < \mathrm{t} < \mathrm{t}_K$ is

governed by the weak-coupling fixed point of the Kondo problem [16], and $\mathtt{t}_K$ constitutes the decay time of the magnetization in this intermediate regime towards the formation of a spin singlet with the conduction electrons.

Therefore, we aim to get an estimate of the Kondo temperature as a function of the ratio between the interaction strength U and the effective tunneling rate Γ from the dynamics of the impurity magnetization $\langle\sigma^z\rangle = \langle\hat{n}_\uparrow\rangle - \langle\hat{n}_\downarrow\rangle$. We prepare the quantum dot in the polarized state $|\hat{n}_\uparrow = 1, \hat{n}_\downarrow = 0\rangle$ and measure its evolution in time after a zero-bias quench. For this analysis, we choose $L = 64$ as the lead length and the hopping decay length between $\xi = 8$ and $\xi = 32$, depending on the energy resolution needed to accurately measure the magnetization up to times of the order of $\mathtt{t}_K$.

We consider two values for the interaction strength, $U = t_0$ and $U = 0.4t_0$, and we examine the particle-hole symmetric point $V_g = -0.5U$. To extract the predicted exponential dependence of the Kondo temperature from U/Γ [7, 12, 16], we vary the hybridization strength Γ between $\sim U/20$ ($J \sim 0.15U$) and $\sim U/2$ ($J \sim 0.5U$).

Figure 2(a) shows the decay in time of the magnetization for different values of U/Γ while we fix $U = t_0$. We can easily identify three regimes: at short time $\mathtt{t} \lesssim \Gamma^{-1}$, the different curves collapse on each other as the relevant time scale for the relaxation of the impurity is set only by Γ (dashed black line). Indeed, notice that time is measured in units of Γ^{-1}. At longer times, the relaxation rate depends on the ratio U/Γ, with a slower decay the further the system lies in the strongly interacting/weak-coupling regime. For these intermediate values of $\mathtt{t}$, we can extract the relaxation time by exponential fits of the data (dot-dashed gray lines). Finally, the impurity approaches a steady state with a finite magnetization; in Fig. 2(a) this last regime is visible only for $U = 2\Gamma$. Due to the unitary dynamics, the system keeps the memory of its initial state and a complete relaxation to a $SU(2)$ invariant state can not be reached. Comparable results have been obtained in Ref. [12] with real-time density matrix renormalization group (DMRG) applied to a similar MPS construction.

Figure 2(b) illustrates the inverse of the relaxation times $\mathtt{t}_K(U/\Gamma)$ extracted from the magnetization decay at intermediate times [grey lines of panel (a)] as a function of U/Γ and for two values of the Hubbard interaction U. We interpret this quantity as the Kondo temperature $T_K \sim \mathtt{t}_K^{-1}$. A comparison with the renormalization group prediction

$$T_K \sim \sqrt{U\Gamma}\mathrm{e}^{-\frac{\pi\Gamma}{8U}} \tag{5}$$

(solid black line) shows excellent agreement with our data for both values of the interaction strength. In the inset the same data are displayed in logarithmic scale to emphasize the exponential dependence of the Kondo temperature from U/Γ. Moreover, the two datasets perfectly collapse on top of each other, highlighting the universal character of the exponential decay linked to the Kondo temperature. At very weak coupling ($U/\Gamma \gg 1$) the long evolution time needed for an accurate estimate of the relaxation time can not be reached and our data deviate from the analytical prediction. Although the entanglement growth ultimately limits our ability to simulate the evolution of large systems at long time, thus preventing the observation of Kondo correlations for very weak coupling, our method allows us to observe nonperturbative effects emerging directly from the nonequilibrium properties of the AIM.

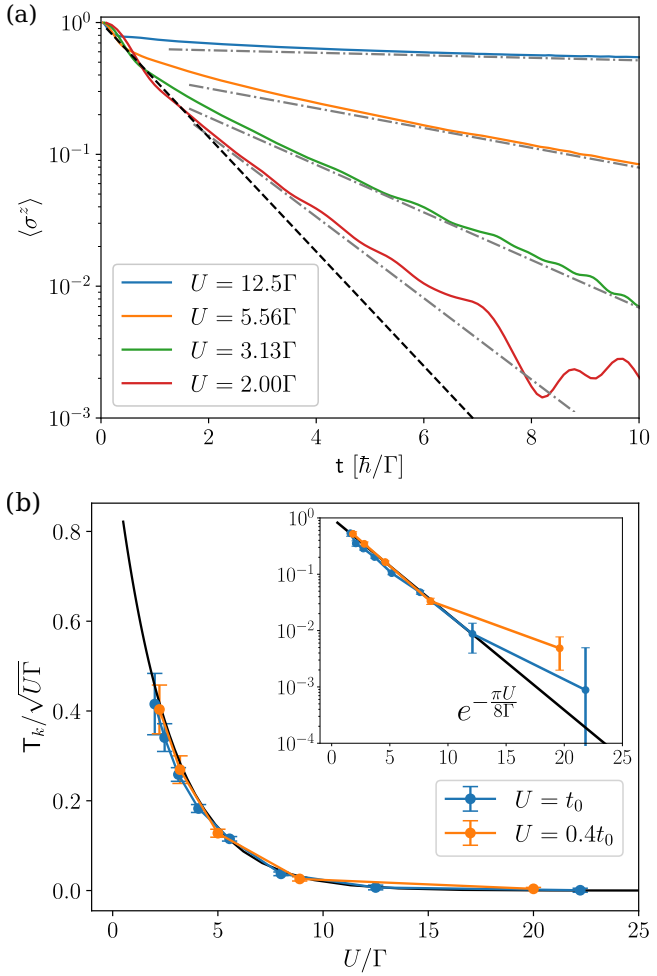

Figure 2. (a): Expectation value of the magnetization $\langle\sigma^z\rangle = \langle\hat{n}_\uparrow\rangle - \langle\hat{n}_\downarrow\rangle$ as a function of time (in units of $\hbar/\Gamma$) in a zero-bias quench. The dashed black lines indicates the short-time relaxation $\mathrm{e}^{-\mathrm{t}\Gamma/\hbar}$ while the gray dot-dashed lines highlight the slow dynamics due to the Kondo resonance $\mathrm{e}^{-\mathrm{t}/\mathrm{t}_K}$. The data correspond to $U = t_0$ (b): Kondo temperature, extracted from the slow relaxation shown in panel(a), versus the effective interaction strength for two values of U. The solid black line corresponds to the RG prediction for the Kondo temperature $T_K \sim \sqrt{U\Gamma}\mathrm{e}^{-\frac{\pi U}{8\Gamma}}$. The inset shows the same data in logarithmic scale to emphasize the exponential behaviour of T_K. For large values of U/Γ our accuracy is limited by the small signal-to-noise ratio of the time evolution of the magnetization.

The data in Fig. 2 are obtained with a zero-bias

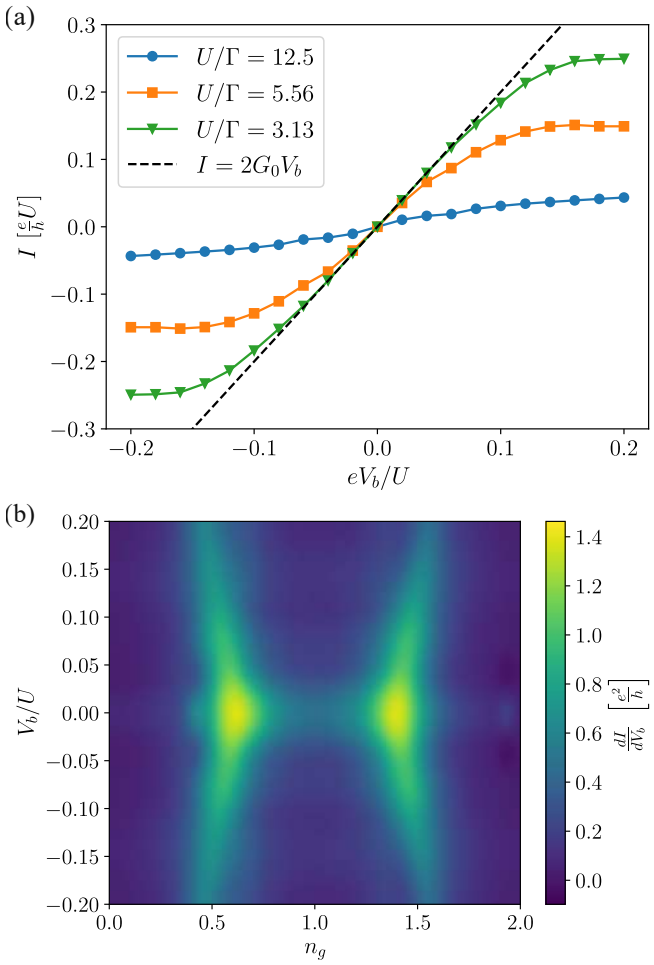

Figure 3. (a) Current vs voltage bias in the symmetric point $V_g = -0.5U$ for three different values of the hybridization strength Γ and $U = t_0$. The dashed line corresponds to the quantized current $I = 2\frac{e^2}{h}V_b$. (b) Differential conductance as a function of the induced charge n_g and of the voltage bias V_b between the left and right leads, in the strongly interacting/weak-coupling regime $U/\Gamma = 12.5$. The zero bias peak extending between the two sequential tunneling resonances at $n_g = 0.5$ and $n_g = 1.5$ signals the onset of the Kondo effect.

quench, i.e., with a vanishing bias voltage. When dealing with transport properties, we evolve instead the system with a voltage bias $V_b = \mu_L - \mu_R$ between the two leads in order to observe a quasi-stationary current. Here we use the $\mu-$quench protocol: in this scenario the initial state is the correlated ground state of the Hamiltonian $\hat{H}$ (obtained through the DMRG), quenched at $\mathtt{t} = 0$ to a Hamiltonian with a finite voltage bias. To simulate the quench dynamics at finite bias, we also need to adjust the decay length of the hopping amplitude in the lead, ξ, such that the density of states in the leads is approximately constant in the energy interval between μ_L and μ_R. The convergence in the simulation parameters (ξ, L, and the TDVP time step discretization) is reached when the current signal displays a plateau in time long enough to reliably extract its expectation value in the quasi-steady state that develops after the quantum quench. The maximum bond dimension adopted is $\chi = 2000$ with a truncation error $O(10^{-8})$.

In Fig. 3(a) we plot the quasi steady current as a function of the voltage bias for different values of the effective tunneling rate Γ, while keeping fixed the Hubbard interaction U, at the particle-hole symmetric point $V_g = 0.5U$. As we approach the strong-coupling regime $\Gamma \sim U$, the current tends toward a linear response with a quantized differential conductance $\frac{dI}{dV_b} = 2\frac{e^2}{h}$, i.e. there are two perfectly transmitting channels (dashed black line). The Kondo temperature T_K sets the extension of the bias window in which this quantization occurs [28]. In particular, as showed in Fig. 2(b), the Kondo energy scale drops down exponentially at weak coupling, $U/\Gamma \gg 1$, and can become smaller than the values of voltage bias we can resolve with the chosen lead length $L = 100$ and hopping decay length $\xi = 30$. This explains the apparent deviation from the quantized conductance at weak coupling $U/\Gamma = 12.5$ in Fig 3(a). Similar results are shown in Ref. [15]. We remark that, away from the strong coupling regime, we can simulate transport for voltages larger than the tunneling rate Γ. The main limitation comes from the fast entanglement growth when states in a large energy window contribute significantly to transport, which happens when V_b covers a significant fraction of the leads' bandwidth. In our model, this limitation becomes particularly relevant when $V_b \sim U$, t_0 is large enough to excite the quantum dot and there is a strong current flow due to sequential tunneling resonances at finite bias.

Fig. 3(b) illustrates the differential conductance in the weak-coupling regime ($U/\Gamma = 12.5$) as a function of the bias V_b and the induced charge parameter n_g which is linked to the chemical potential as $V_g = \frac{U}{2}(1 - 2n_g)$ and determines the expectation value of the total occupation of the quantum dot.

We derive the differential conductance in Fig. 3(b) from the simulation of a μ-quench protocol in which the system is initialized in the ground state of $\widehat{H}$ at half filling, thus for the particle-hole symmetric point ($n_g = 1, V_g = -0.5U$). At time $\mathtt{t} = 0$, both the induced charge n_g and the bias voltage V_b are quenched to their final value [horizontal and vertical axis of Fig. 3(b)].

At $n_g = 0.5$ and $n_g = 1.5$ we observe two bright zero-bias sequential tunneling resonance, corresponding to the degeneracies between the empty and singly-occupied dot ($n_g = 0.5$) or between the singly and doubly occupied dot ($n_g = 1.5$). At finite voltage, the conductance peaks are prolonged along the lines $V_b = \pm U(1 - 2n_g)$ and $V_b = \pm U(3 - 2n_g)$, following the resonances between each biased lead and the quantum dot. Between the two charge-degeneracy points, an extended zero bias peak indicates the onset of the Kondo effect, although for strong interaction and weak coupling we can not see the quantization of the conductance. This limitation originates mainly from the high voltage resolution needed to sam-

ple the current at energy below the Kondo temperature, which for $U/\Gamma = 12.5$ is of the order $T_K \sim 10^{-3}U$, where we expect the quantized linear response. To reach such resolution in V_b, we need either a larger system size or a shorter decay length ξ. The former makes the simulations computationally more expensive, while the latter induces nonphysical effects in simulations at higher energy, preventing the calculation of the differential conductance in a wide bias range. As common in nanostructure experiments (see, for instance, Ref. [4]), this zero-bias peak does not extend to $n_g < 0.5$ or $n_g > 1.5$ where the ground state of the quantum dot becomes respectively, empty, or fully occupied, thus loosing the doublet degeneracy necessary for the Kondo effect.

Conclusions. In this work we applied the tensor network method introduced in Ref. [19] to study the Kondo effect in the Anderson impurity model. In particular, we used a MPS+TDVP approach to study the dynamics of a single-level interacting quantum dot coupled to two fermionic leads after quantum quenches of the Hamiltonian parameters.

We examined both the out-of-equilibrium evolution of the quantum dot magnetization, and the electric transport features emerging in a nonequilibrium quasi-steady state after the quench.

The magnetization dynamic allows us to obtain a good estimate of the Kondo temperature as the inverse of its relaxation time when the quantum dot is coupled to unbiased leads. Such estimate is in agreement with renormalization group results [7]. In particular, the magnetization decay displays two typical time scales: the effective coupling rate with the leads and the Kondo time scale. The appearance of these two decay regimes for short and intermediate times is reminiscent of the experimental results concerning the evolution of the spin population of impurities in 1D ultracold Yb gases [5].

Concerning the study of the conductance of the system, relevant for transport measurements in nanostructures, our simulations allow us to study its evolution when a voltage bias is applied between the two leads. By looking at the emergent quasi-steady state, we can reconstruct its Coulomb blockade properties as well as the emergence of a Kondo peak at zero bias. The latter appears when the impurity chemical potential fixes its ground state in the degenerate singly-occupied sector and the related differential conductance approaches the quantized value $G = 2\frac{e^2}{h}$ in the strong-coupling regime.

We can simulate the system dynamics in a broad parameter range, from a strongly interacting/weak-coupling regime to a strong-coupling one, well beyond the applicability of standard perturbative master-equation approaches. Moreover, our method is not limited by single site or small impurities but can be easily extended to multilevel quantum dots or nanowires with long-range Coulomb repulsion.

Additionally, our approach can address superconducting systems, opening the path for the study of the out-of-equilibrium dynamics of the topological Kondo effect [29–31], which arises in multiterminal impurities with p-wave superconducting coupling. This kind of system can be easily described by identifying the spin degrees of freedom of the AIM as a label for different spinless leads.

In general, our method can thus be used to investigate transport phenomena in hybrid superconducting-semiconducting multiterminal devices with strong Coulomb interactions (see, for instance, Refs. [32, 33]), without being limited to a weak-coupling regime. This offers the possibility of investigating the variety of subgap states [34] that can appear in these platforms, thus providing important details towards the realization of Majorana - Cooper pair boxes and other building blocks for quantum devices [35, 36].

Acknowledgements. We thank J. Paaske and V. Baran for fruitful discussions. M.W., L.M. and M.B. are supported by the Villum Foundation (Research Grant No. 25310). This project has received funding from the European Union's Horizon 2020 research and innovation program under the Marie Skłodowska-Curie Grant Agreement No. 847523 "INTERACTIONS." C.-M.C. acknowledges the support by the Ministry of Science and Technology (MOST) under Grant No. 111-2112-M-110-006-MY3, and by the Yushan Young Scholar Program under the Ministry of Education (MOE) in Taiwan.

[1] D. Goldhaber-Gordon, H. Shtrikman, D. Mahalu, D. Abusch-Magder, U. Meirav, and M. A. Kastner, Kondo effect in a single-electron transistor, Nature **391**, 156 (1998).

[2] S. M. Cronenwett, T. H. Oosterkamp, and L. P. Kouwenhoven, A tunable kondo effect in quantum dots, Science **281**, 540 (1998).

[3] J. Nygård, D. H. Cobden, and P. E. Lindelof, Kondo physics in carbon nanotubes, Nature **408**, 342 (2000).

[4] T. S. Jespersen, M. Aagesen, C. Sørensen, P. E. Lindelof, and J. Nygård, Kondo physics in tunable semiconductor nanowire quantum dots, Phys. Rev. B **74**, 233304 (2006).

[5] L. Riegger, N. Darkwah Oppong, M. Höfer, D. R. Fernandes, I. Bloch, and S. Fölling, Localized magnetic moments with tunable spin exchange in a gas of ultracold fermions, Phys. Rev. Lett. **120**, 143601 (2018).

[6] M. Kanász-Nagy, Y. Ashida, T. Shi, C. Moca, T. N. Ikeda, S. Fölling, J. I. Cirac, G. Zaránd, and E. A. Demler, Exploring the anisotropic kondo model in and out of equilibrium with alkaline-earth atoms, Phys. Rev. B **97**, 155156 (2018).

[7] X. Wang, C. D. Spataru, M. S. Hybertsen, and A. J. Millis, Electronic correlation in nanoscale junctions: Comparison of the gw approximation to a numerically exact solution of the single-impurity anderson model, Phys. Rev. B **77**, 045119 (2008).

[8] L. G. G. V. Dias da Silva, F. Heidrich-Meisner, A. E. Feiguin, C. A. Büsser, G. B. Martins, E. V. Anda, and

E. Dagotto, Transport properties and Kondo correlations in nanostructures: Time-dependent DMRG method applied to quantum dots coupled to Wilson chains, Phys. Rev. B **78**, 195317 (2008).
[9] F. Heidrich-Meisner, A. E. Feiguin, and E. Dagotto, Real-time simulations of nonequilibrium transport in the single-impurity Anderson model, Phys. Rev. B **79**, 235336 (2009).
[10] E. Gull, D. R. Reichman, and A. J. Millis, Numerically exact long-time behavior of nonequilibrium quantum impurity models, Phys. Rev. B **84**, 085134 (2011).
[11] F. Güttge, F. B. Anders, U. Schollwöck, E. Eidelstein, and A. Schiller, Hybrid NRG-DMRG approach to real-time dynamics of quantum impurity systems, Phys. Rev. B **87**, 115115 (2013).
[12] Z. He and A. J. Millis, Entanglement entropy and computational complexity of the Anderson impurity model out of equilibrium: Quench dynamics, Phys. Rev. B **96**, 085107 (2017).
[13] F. Schwarz, I. Weymann, J. von Delft, and A. Weichselbaum, Nonequilibrium steady-state transport in quantum impurity models: A thermofield and quantum quench approach using matrix product states, Phys. Rev. Lett. **121**, 137702 (2018).
[14] R. S. Souto, R. Avriller, A. L. Yeyati, and A. Martín-Rodero, Transient dynamics in interacting nanojunctions within self-consistent perturbation theory, New Journal of Physics **20**, 083039 (2018).
[15] J. Thoenniss, M. Sonner, A. Lerose, and D. A. Abanin, An efficient method for quantum impurity problems out of equilibrium (2022).
[16] M. F. Cavalcante, R. G. Pereira, and M. C. O. Aguiar, Quench dynamics of the kondo effect: Transport across an impurity coupled to interacting wires, Phys. Rev. B **107**, 075110 (2023).
[17] A. Manaparambil, A. Weichselbaum, J. von Delft, and I. Weymann, Nonequilibrium spintronic transport through kondo impurities, Phys. Rev. B **106**, 125413 (2022).
[18] L. Kohn and G. E. Santoro, Quench dynamics of the Anderson impurity model at finite temperature using matrix product states: entanglement and bath dynamics, Journal of Statistical Mechanics: Theory and Experiment **2022**, 063102 (2022).
[19] C.-M. Chung, M. M. Wauters, and M. Burrello, Matrix product state simulations of quantum quenches and transport in coulomb blockaded superconducting devices, Phys. Rev. B **106**, 094308 (2022).
[20] H. Aoki, N. Tsuji, M. Eckstein, M. Kollar, T. Oka, and P. Werner, Nonequilibrium dynamical mean-field theory and its applications, Rev. Mod. Phys. **86**, 779 (2014).
[21] C.-C. Chien, M. Di Ventra, and M. Zwolak, Landauer, Kubo, and microcanonical approaches to quantum transport and noise: A comparison and implications for cold-atom dynamics, Phys. Rev. A **90**, 023624 (2014).
[22] J. Haegeman, J. I. Cirac, T. J. Osborne, I. Pižorn, H. Verschelde, and F. Verstraete, Time-dependent variational principle for quantum lattices, Phys. Rev. Lett. **107**, 070601 (2011).
[23] J. Haegeman, C. Lubich, I. Oseledets, B. Vandereycken, and F. Verstraete, Unifying time evolution and optimization with matrix product states, Phys. Rev. B **94**, 165116 (2016).
[24] M. M. Rams and M. Zwolak, Breaking the entanglement barrier: Tensor network simulation of quantum transport, Phys. Rev. Lett. **124**, 137701 (2020).
[25] M. Fishman, S. R. White, and E. M. Stoudenmire, The ITensor Software Library for Tensor Network Calculations, SciPost Phys. Codebases , 4 (2022).
[26] The source code can be found in the repository `https://github.com/chiamin/QuenchTranportTwoChains`.
[27] F. B. Anders and A. Schiller, Real-time dynamics in quantum-impurity systems: A time-dependent numerical renormalization-group approach, Phys. Rev. Lett. **95**, 196801 (2005).
[28] A. Kaminski, Yu. V. Nazarov, and L. I. Glazman, Universality of the Kondo effect in a quantum dot out of equilibrium, Phys. Rev. B **62**, 8154 (2000).
[29] B. Béri and N. R. Cooper, Topological Kondo effect with Majorana fermions, Phys. Rev. Lett. **109**, 156803 (2012).
[30] B. Béri, Majorana-Klein hybridization in topological superconductor junctions, Phys. Rev. Lett. **110**, 216803 (2013).
[31] A. Altland and R. Egger, Multiterminal Coulomb-Majorana junction, Phys. Rev. Lett. **110**, 196401 (2013).
[32] T. Kanne, D. Olsteins, M. Marnauza, A. Vekris, J. C. Estrada Saldaña, S. Loric, R. D. Schlosser, D. Ross, S. Csonka, K. Grove-Rasmussen, J. Nygård, Double nanowires for hybrid quantum devices, Advanced Functional Materials **32**, 2107926 (2022).
[33] A. Vekris, J. C. Estrada Saldaña, T. Kanne, T. Hvid-Olsen, M. Marnauza, D. Olsteins, M. M. Wauters, M. Burrello, J. Nygård, and K. Grove-Rasmussen, Electronic transport in double-nanowire superconducting islands with multiple terminals, Nano Letters **22**, 5765 (2022), pMID: 35833741, https://doi.org/10.1021/acs.nanolett.2c01161.
[34] R. S. Souto, M. M. Wauters, K. Flensberg, M. Leijnse, and M. Burrello, Multiterminal transport spectroscopy of subgap states in coulomb-blockaded superconductors, Phys. Rev. B **106**, 235425 (2022).
[35] Y. Oreg and F. von Oppen, Majorana zero modes in networks of cooper-pair boxes: Topologically ordered states and topological quantum computation, Annual Review of Condensed Matter Physics **11**, 397 (2020).
[36] C. W. J. Beenakker, Search for non-Abelian Majorana braiding statistics in superconductors, SciPost Phys. Lect. Notes , 15 (2020).

The topological Kondo model out of equilibrium

Matteo M. Wauters,[1] Chia-Min Chung,[2,3,4] Lorenzo Maffi,[1] and Michele Burrello[1]

[1] *Niels Bohr International Academy and Center for Quantum Devices, Niels Bohr Institute, Copenhagen University, Universitetsparken 5, 2100 Copenhagen, Denmark*
[2] *Department of Physics, National Sun Yat-sen University, Kaohsiung 80424, Taiwan*
[3] *Center for Theoretical and Computational Physics, National Sun Yat-Sen University, Kaohsiung 80424, Taiwan*
[4] *Physics Division, National Center for Theoretical Sciences, Taipei 10617, Taiwan*

The topological Kondo effect is a genuine manifestation of the nonlocality of Majorana modes. We investigate its out-of-equilibrium signatures in a model with a Cooper-pair box hosting four of these topological modes, each connected to a metallic lead. Through matrix-product-state techniques, we simulate the relaxation of the Majorana magnetization, which allows us to determine the related Kondo temperature. Then, we analyze the onset of electric transport after a quantum quench of a lead voltage. Our results apply to Majorana Cooper-pair boxes fabricated in double nanowire devices and provide non-perturbative evidence of the crossover from weak-coupling states to the strongly correlated topological Kondo regime. The latter dominates at the superconductor charge degeneracy points and displays the expected universal fractional zero-bias conductance.

The engineering of Majorana zero-energy modes (MZMs) in hybrid superconducting-semiconducting devices has been the core of strenuous theoretical and experimental activities for the last two decades [1–3]. The detection of these subgap modes relies primarily on tunneling spectroscopy applied to a rich variety of platforms. Tunneling spectroscopy, however, cannot provide direct evidence of the most intriguing properties of Majorana modes, namely their nonlocal and anyonic features. Hence, it is desirable to devise a new generation of experiments that balances the constraints imposed by the current technological limitations and the pursuit of MZM evidence beyond spectroscopy.

In this respect, the topological Kondo effect (TKE) [4–6] plays a crucial role: on one side, it is a transport signature of MZMs well-suited for experimental observations; on the other, it directly results from their nonlocality, such that it can hardly be confused with phenomena originating by nontopological subgap states [7]. The TKE is predicted to emerge in multiterminal devices where M external leads are coupled to a Majorana Cooper-pair box hosting four MZMs and characterized by a sufficiently strong charging energy E_c (Fig. 1). The TKE manifests itself as a universal nonlocal zero-bias conductance $dI_\alpha/dV_{\beta\neq\alpha}$ quantized at values $2e^2/Mh$. Such conductance is approached at low temperatures in the strong coupling regime in correspondence of both the Coulomb valleys and Coulomb peaks of the related devices [8], as derived from the renormalization group (RG) analysis of effective low-energy models describing the Majorana Cooper-pair box and its coupling to the leads [4–6, 8–12].

We adopt a more elementary approach to show the onset of the TKE in out-of-equilibrium systems: we investigate a minimal fermionic model that includes not only the zero-energy Majorana degrees of freedom of the Cooper-pair box, but also its quasiparticle excitations above the superconducting gap. We study, in particular, its dynamics following different protocols of quantum quenches. The time evolution is determined by the tunneling of single electrons from the leads to the central superconducting island, and, differently from the most typical characterizations of the TKE [4, 6, 10, 13–15], we apply matrix-product-state simulations [16] which do not rely on any perturbative approximation of this coupling. This technique allows us to examine the crossover between the predicted weak-coupling and topological Kondo strong-coupling regimes.

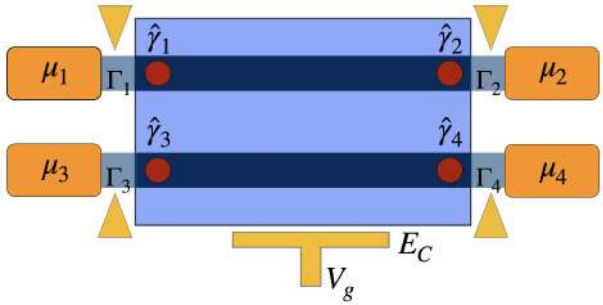

Figure 1. Schematics of the system: two p-wave superconducting nanowires with MZMs at the edges are coupled by a superconducting island (blue) with charging energy E_c. Voltage gates (yellow) tune the island induced charge, $n_g \propto V_g$, and the coupling rates Γ_α with the leads (orange). Each MZM is coupled with a single normal lead at chemical potential μ_α.

The model we propose aims at describing Majorana Cooper-pair boxes engineered from nanowires. Recent developments in the fabrication of parallel double InAs nanowires hybridized with Al [17, 18] make these platforms suitable to combine all the necessary elements for the implementation of the topological Kondo model. Such devices hold promise to investigate its transport signatures as a function of the lead voltage bias, the charge induced on the central superconducting (SC) island, and

the tunneling rates from the leads to the island (Fig. 1). In the following, we will focus on deriving the dependence of the topological Kondo temperature T_K and currents on these physical parameters.

Model and methods.- The minimal model for the TKE that we consider describes two parallel 1D topological superconductors coupled by a common floating SC island with charging energy E_c and charge n_g induced by the potential V_g (Fig. 1). These two coupled systems effectively represent two nanowires with strong spin-orbit coupling subject to a proximity-induced SC pairing and a suitable Zeeman interaction, which provide the most common route to engineer MZMs [19, 20]. Their low-energy physics is described by spinless fermions subject to an emergent p-wave SC pairing Δ_P. As a result, four MZMs $\{\gamma_\alpha\}_{\alpha=1,\dots,4}$ form at the edges of these nanowires and each of them is coupled to a spinless normal lead. The effective tunneling rates Γ_α between the leads and the MZMs can be switched off to change the number of terminals $M \leq 4$ coupled to the system.

The simplest description for each SC nanowire is a zero-bandwidth model [21, 22], where the lowest energy level is the subgap state defined by two Majorana operators while the higher energy state represents Bogoliubov quasiparticles above the SC gap. This is achieved by considering a 2-site Kitaev chain for each nanowire, with each of the four corresponding fermionic sites tunnel-coupled to one of the leads. This system defines the Majorana Cooper-box [23, 24] sketched in Fig. 1. The Hamiltonian can be decomposed into $\widehat{H} = \widehat{H}_{\rm sys} + \widehat{H}_L + \widehat{H}_{\rm t}$; $\widehat{H}_{\rm sys}$ describes the Majorana Cooper-pair box:

$$\widehat{H}_{\rm sys} = \sum_{\sigma,n} \epsilon_{n,\sigma} \hat{f}^\dagger_{n,\sigma} \hat{f}_{n\,\sigma} + E_c(\hat{N} - n_g)^2 \ , \qquad (1)$$

where $\sigma = \uparrow, \downarrow$ labels the upper and lower nanowires and $n = 0, 1$ labels the two quasiparticle energy levels in each of them[25]. $\hat{N}$ is the total charge of the box with respect to an arbitrary offset. It includes the charge of its Cooper pairs, as well as the electrons in the nanowires.

The two zero-energy quasiparticles are generated by the combinations of the MZMs $\hat{f}_{0,\uparrow} = (\hat{\gamma}_1 - i\hat{\gamma}_2)/2$ and $\hat{f}_{0,\downarrow} = (\hat{\gamma}_3 - i\hat{\gamma}_4)/2$. We label the four corresponding low-energy states by $|n_\uparrow n_\downarrow\rangle$, with $\hat{n}_\sigma = \hat{f}^\dagger_{0,\sigma}\hat{f}_{0,\sigma}$. The charging energy splits them into two two-dimensional degenerate subspaces with different total fermionic parity $(-1)^{\hat{N}}$.

The leads are modeled by Wilson chains [16, 26, 27]

$$\widehat{H}_L = \sum_{\alpha=1}^{4} \sum_{l=1}^{\mathcal{L}} \left[-t_0 \mathrm{e}^{-(l-1)/\xi} \hat{c}^\dagger_{\alpha,l+1} \hat{c}_{\alpha,l} + \mathrm{h.c.} \right] - \mu_\alpha \hat{c}^\dagger_{\alpha,l} \hat{c}_{\alpha,l} \ , \qquad (2)$$

with t_0 being the *bare* hopping amplitude which sets their bandwidth and is the largest energy scale in our simulations. The hopping decay length ξ is a numerical auxiliary variable that allows us to tune the resolution at small energies by modifying the lead level spacing [16, 27, 28]. The chemical potentials μ_α are used to bring the system out of equilibrium and study nonlocal transport properties.

Finally, the tunneling Hamiltonian between the leads and the system is

$$\widehat{H}_{\rm t} = -\sum_{\alpha=1}^{4} \sum_{\sigma,n} J_\alpha \left[\left(u_{\alpha,\sigma,n} \hat{f}^\dagger_{\sigma,n} + v_{\alpha,\sigma,n} \hat{f}_{\sigma.n} \right) \hat{c}_{\alpha,1} + \mathrm{H.c.} \right] , \qquad (3)$$

where $u_{\alpha,\sigma,n}$ ($v_{\alpha,\sigma,n}$) is the particle (hole) projection of $\hat{f}_{\sigma,n}$ on the real-space site coupled to the lead α. The tunneling amplitudes J_α are linked to the effective tunneling rates as $\Gamma_\alpha = \frac{J_\alpha^2}{2t_0}$. Throughout this paper, we fix the p-wave pairing Δ_P and the nanowire hopping amplitude $t_{\rm sys}$ to $\Delta_P = t_{\rm sys} = 0.5t_0$. We also induce a small hybridization between the MZMs on each nanowire by setting $\mu_{\rm sys} = 0.01t_0$ in both Kitaev chains [25].

In our simulations, we map the system into a matrix product state (MPS) by following the approach in Refs. [16, 28]. Each MPS site represents a single-particle eigenstate of either the leads or the nanowires (Bogoliubov quasiparticles for nanowires) and we order them based on their energy. The charge degree of freedom $\hat{N}$ is encoded in an auxiliary bosonic site [25, 29]. The real-time dynamics is simulated using the time-dependent variational principle (TDVP) algorithm [30–32] from the ITensor library [33, 34].

Relaxation towards equilibrium.- In the dynamics of Kondo problems, the formation of strong correlations and the Kondo screening cloud occurs over a time scale given by T_K^{-1} [28, 35–37]. Therefore, the relaxation after a quantum quench offers a useful probe to estimate the Kondo temperature and verify the onset of strongly correlated states.

The first quench protocol we consider aims at observing the relaxation of the Majorana Cooper-pair box caused by the coupling with the leads. The SC box is initially prepared in the ground state $|00\rangle$ ($N = 0$) for $n_g < 0.5$, or $|10\rangle$ ($N = 1$) for $n_g > 0.5$. The box is originally decoupled from the leads, which are set at half-filling. At time $\mathtt{t} = 0$, the couplings Γ are suddenly turned on and the device begins relaxing toward equilibrium. To characterize this relaxation, we analyze the average charge on the island $\langle \hat{N}(t) \rangle$, and the effective Majorana magnetization [4, 13], defined as $\langle \hat{Z}_{\rm eff}(t) \rangle \equiv \langle i\hat{\gamma}_3\hat{\gamma}_4(t) \rangle = 1 - 2\langle \hat{n}_\downarrow(t) \rangle$.

The observed dependence of the charge $\langle \hat{N} \rangle$ on n_g after equilibration (Fig. 2) shows the crossover between the weak-coupling and the strong-coupling regime. In particular, following Ref. [38], we characterize the weak-coupling regime at $n_g \sim 0$ by the slope of $\langle \hat{N} \rangle$:

$$\left. \frac{\partial \langle \hat{N} \rangle}{\partial n_g} \right|_{n_g = 0} = \frac{M \Delta_P \Gamma}{E_c t_0} \ . \qquad (4)$$

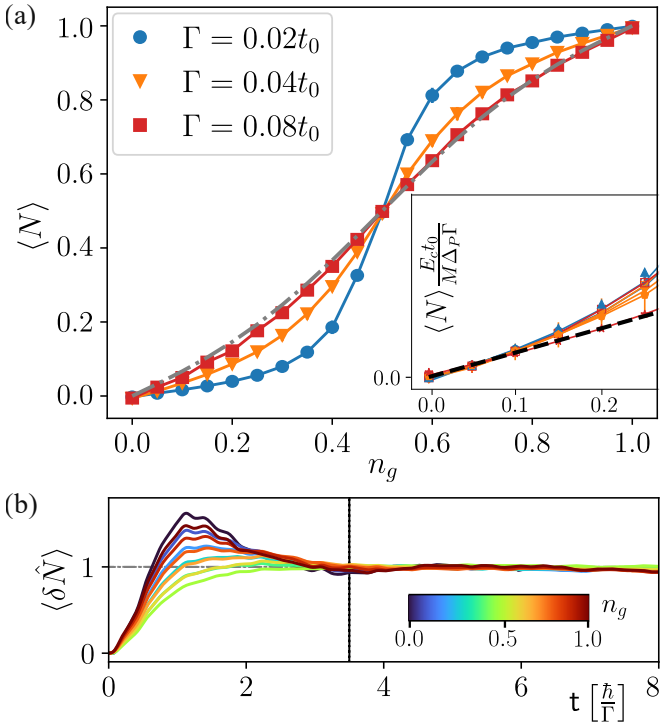

Figure 2. (a) Equilibrium charge as a function of n_g, for $M = 3$, $E_c = 0.2t_0$. The gray dot-dashed line corresponds to Eq. (5) for $\Gamma = 0.08t_0$. The inset shows data for different values of E_c ($0.2t_0$ and $0.4t_0$) and $M = 3$, 4 in the weak coupling regime, rescaled by $\frac{M\Delta_P\Gamma}{E_c t_0}$. The dashed black line corresponds to Eq. (4). (b) Relaxation of the charge for different values of $n_g \in [0, 1]$, $E_c = 0.2t_0$ and $\Gamma = 0.04t_0$. All data are obtained with $\mathcal{L} = 64$ and $\xi = 16$.

When the coupling Γ is weak, the charge datasets corresponding to different choices of E_c, and M exhibit a good agreement with Eq. (4) [inset of Fig. 2(a)]. On the other hand, the sinusoidal correction derived in Ref. [38] for the strong-coupling regime,

$$\langle \hat{N} \rangle = n_g - \left(\frac{E_c}{\Delta_P} \sqrt{1 - \Gamma/t_0} \right)^M \sin(2\pi n_g), \qquad (5)$$

closely matches the numerical data for the highest value of the tunneling rate $\Gamma = 0.08t_0$ [gray dot-dashed line and red squares in Fig. 2(a)], thus suggesting the emergence of Kondo correlations.

Importantly, the time scale associated with the relaxation of $\langle \hat{N} \rangle$ depends on the ratio Γ/E_c but not on the induced charge n_g, as shown in Fig. 2(b) where we plot the time dependence of the relative charge variation, defined as

$$\langle \delta \hat{N}(t) \rangle = \frac{|\langle \hat{N}(t) \rangle - \langle \hat{N}(0) \rangle|}{|\langle \hat{N}(t \to \infty) \rangle - \langle \hat{N}(0) \rangle|} . \qquad (6)$$

The vertical line marks the equilibration time and different curves, corresponding to different values of

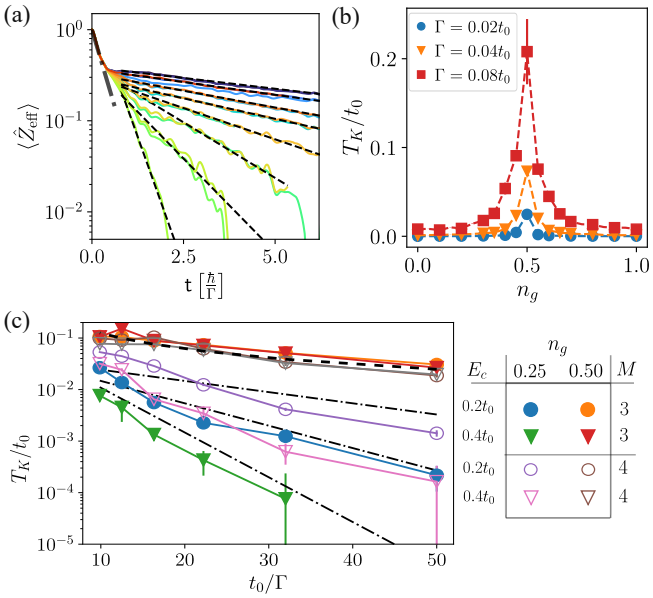

Figure 3. (a): Dynamics of the Majorana magnetization for different values of $n_g \in [0, 1]$. The dot-dashed line marks the fast relaxation depending on Γ alone. (b) T_K extracted as the relaxation rate of $\langle \hat{Z}_{\rm eff} \rangle$ —dashed black lines in panel (a)— as a function of n_g. (c) T_K as a function of the timescale Γ^{-1} at $n_g = 0.5$ and in the even-parity Coulomb valley ($n_g = 0.25$). Dot-dashed lines indicate the expected scaling in the valleys [Eq. (7)], whereas the dashed line marks the scaling at the charge degeneracy point $T_K \sim M\Gamma$. A non-universal prefactor $C \sim 0.2$ has been manually set to approximately match the data. All data are obtained with $\mathcal{L} = 64$, $\xi = 16$.

$n_g \in [0, 1]$, converge to the asymptotic value on similar time scales.

The magnetization, instead, displays a remarkably different behavior, as shown in Fig.3(a). At short times, $\mathsf{t} < \hbar/\Gamma$, the relaxation is dominated by the fast rate Γ (dot-dashed line) independently of both E_c and n_g. Then, there emerges a second timescale that depends on both Γ and the energy difference $\delta E(n_g) = E_c|1 - 2n_g|$ between the charge sectors $N = 0$ and $N = 1$. The black dashed lines in Fig. 3(a) are exponential fits of these slower decays for different values of $n_g \in [0, 1]$, while $E_c = 0.2t_0$ and $\Gamma = 0.08t_0$. This behavior is analogous to the relaxation of the magnetization in the Anderson impurity model [28, 39], suggesting that this longer timescale is associated with the energy scale T_K of the emerging TKE.

The comparison of Figs. 3(a) and 2(b) makes it evident that this Kondo timescale characterizes only the Majorana magnetization but not the charge; the former constitutes indeed one of the effective Pauli operators, $\langle \hat{Z}_{\rm eff} \rangle$, at the heart of the definition of the TKE, whereas $\langle \hat{N} \rangle$ depends only on the fermionic parity of the SC island. Therefore, we interpret this charge - "spin" separation after the quantum quench as evidence of the emergence of the TKE.

Motivated by this observation, we analyze the dependence of the so-derived decay rates T_K on n_g, Γ, and E_c. Figure 3(b) depicts the fitted T_K as a function of the induced charge for different values of the coupling Γ and $E_c = 0.2t_0$. As expected from RG analyses, T_K is larger at the charge degeneracy point, where it is proportional to $M\Gamma$, consistently with Ref. [38]. In the Coulomb valleys, instead, T_K is qualitatively compatible with standard RG predictions [38]:

$$T_K \sim E_c \mathrm{e}^{-\frac{\delta E(n_g) t_0}{2(M-2)\Gamma\Delta_P}}. \tag{7}$$

The different behaviors at the charge degeneracy point ($n_g = 0.5$) and in the even Coulomb valley ($n_g = 0.25$) are exemplified in Fig. 3(c), where we plot T_K versus t_0/Γ for $E_c = 0.2t_0$ (circles) and $E_c = 0.4t_0$ (triangles), with both $M = 3$ (full symbols) and $M = 4$ (empty symbols). The Kondo temperature extracted at $n_g = 0.5$ is independent of both E_c and M and it decreases with a power law compatible with $T_K \sim \Gamma$ (dashed line). For large values of Γ, the magnetization can change sign, preventing us from extracting T_K with high precision (see also the large errorbar at $n_g = 0.5$ in Fig. 3(b)). When looking at the Coulomb valleys, instead, T_K shows a substantial drop when increasing the charging energy: not only it is smaller for $E_c = 0.4t_0$, but it decreases faster with $1/\Gamma$, in accordance with Eq. (7) (dot-dashed lines). Notice that the data for $M = 4$, $E_c = 0.4t_0$ and $M = 3$, $E_c = 0.2t_0$ almost coincide as Eq. (7) predicts the same behavior but for a factor 2 in front. Our data display a concavity that is absent in Eq. (7) and suggests a competing power law dependence on Γ in agreement with NRG results of the low-energy effective model [10].

Nonlocal transport.- To investigate multiterminal transport properties, we adopt a different quench protocol, using DMRG to prepare the ground state corresponding to the device coupled with M leads at equilibrium ($\mu_\alpha = 0$) and induced charge n_g. In general, such a state is a superposition of different charge and magnetization states. At $\mathrm{t} = 0$ we quench the chemical potential in the first lead to a finite value $\mu_1 = eV_b$ and compute the average current flowing through the remaining connected terminals. We refer to the latter as average nonlocal current.

RG predicts a fractional zero-bias nonlocal conductance, $G_{\mathrm{TKE}} = \frac{2}{M}\frac{e^2}{h}$, independent from all other physical parameters for $T \ll T_K$, both in the Coulomb valleys[4–6], and at the charge-degeneracy points [8, 11, 15, 38]. Our simulations capture this fractional conductance for $M = 3, 4$ for sufficiently strong coupling in proximity of the charge degeneracy point where T_K is maximum and the behavior of this fixed point can be observed for an extended voltage bias window (Fig. 4). Close to the charge degeneracy point, we observe non-Fermi liquid power-law corrections with non-integer exponents which, however, do not seem compatible with the first-order scaling predicted by bosonization and RG [8, 11, 15, 25, 38, 40].

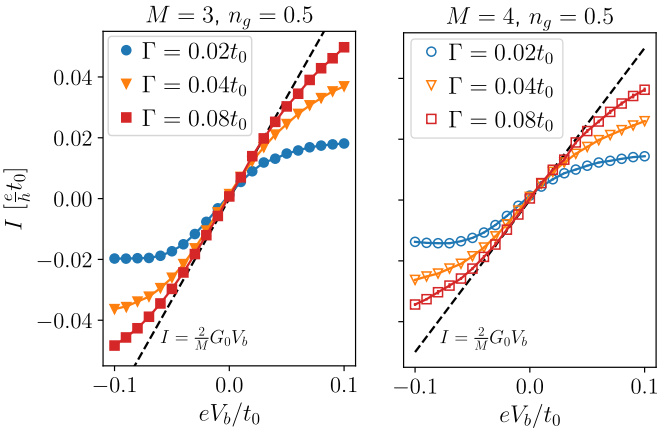

Figure 4. Average nonlocal current as a function of the voltage bias at $n_g = 0.5$, for $M = 3$, 4. The dashed line highlights the TKE prediction $G = \frac{2}{M}G_0$. The data are obtained with $\mathcal{L} = 100$ and $\xi = 32$.

Our simulations are performed at zero temperature, but, away from the charge degeneracy point, T_K becomes comparable with the energy we introduce with the finite bias eV_b, such that we cannot easily capture the universal strong-coupling features of the model. In Fig. 5 we plot the average nonlocal current ($M = 3$ and $E_c = 0.4t_0$) divided by the voltage bias as a function of n_g. We set $\mu_1 = eV_b = 0.02t_0$, which is small enough to probe the response close to the linear regime, yet the data display a good signal-to-noise ratio allowing for a reliable estimate of the current. The TKE prediction is met only at the charge degeneracy point and strong coupling, consistently with Fig. 4, while the strong n_g dependence confirms that we are not deep in the TKE regime; however, there are several hints of the emergence of a strongly-correlated Kondo state also in the Coulomb valleys.

In Fig. 5, we compare our numerical data with the conductance of a single noninteracting resonant fermionic level (dashed lines), which represents the charge degree of freedom coupled with $M = 3$ leads:

$$G_{\mathrm{rl}}(n_g, \mu) = \frac{e^2}{h}\frac{4\Gamma^2}{M^2\Gamma^2 + 4[\mu - E_c(1-2n_g)]^2}\ . \tag{8}$$

G_{rl} exhibits a peak scaling as $4G_0/M^2$ with width $\sim M\Gamma/E_c$. The data with the weakest coupling ($\Gamma = 0.02t_0$, blue circles) match well the corresponding resonant level approximation (8), as expected in a weak coupling regime. When we increase Γ, our data display large discrepancies with Eq. (8), with a conductance rapidly approaching the TKE value of $\frac{2}{3}G_0$ (horizontal dot-dashed line) for $n_g \sim 0.5$. Indeed, in this regime, the applied voltage $\mu_1 = 0.02t_0$ is one order of magnitude smaller than the estimate of the Kondo temperature, $T_K \sim 0.1t_0$ in Fig. 3(c). Moreover, we see a substantial current flowing deep in the Coulomb valleys

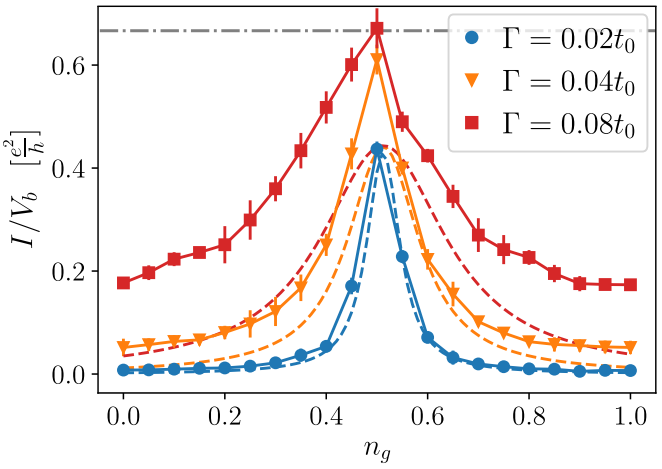

Figure 5. Nonlocal current as a function of n_g, for $E_c = 0.4t_0$. The dashed lines correspond to the resonant level approximation, Eq. (8). The horizontal dot-dashed line is the TKE prediction $\frac{2e^2}{hM}$ with $M = 3$.

$(\Gamma = 0.08t_0, 0.04t_0)$ with apparent plateaus that suggest a crossover to the TKE regime. This is further confirmed by the analysis of the data averaged over the decay length ξ for $n_g = 0.25$, $\Gamma = 0.08t_0$, and $\mu_1 = 10^{-3}t_0$ [25].

Conclusions.- We analyzed the out-of-equilibrium properties of a minimal model for the topological Kondo effect. We aimed at a microscopic description alternative to RG approaches and a qualitative understanding of transport signatures that may arise in double nanowire experiments. The data we collected present evidence of the onset of strongly-correlated states compatible with a crossover between a weak-coupling and a topological Kondo regime.

First, the charge and the effective magnetization of the Majorana Cooper-pair box are characterized by different relaxation behaviors: the former only depends on the system-leads hybridization Γ, whereas the latter presents two separate decay timescales. In analogy with the dynamical features of the Anderson impurity model, we used the longer timescale to estimate the Kondo temperature associated with the TKE, with results compatible with the RG predictions [4, 6].

Second, the nonlocal multiterminal conductance in the intermediate to strong coupling regimes matches the predicted value $G_{\rm TKE} = 2G_0/M$ at the charge degeneracy point, where T_K is the largest. In the Coulomb valleys, it presents large deviations from the noninteracting resonant level approximation that well describes the weak-coupling regime and two-terminal devices [16]. When the resonant level approximation fails, the conductance displays a plateau in the Coulomb valleys, hinting at a crossover to the topological Kondo regime.

Our results are obtained through a matrix product state approach that allows for the study of topological Kondo models without recurring to perturbation theory in the Majorana - lead coupling and does not require any particular hierarchy of the involved energy scales. It is therefore well suited to understand the crossover between strong and weak coupling regimes as well as the corrections to the RG predictions on the TKE when we probe the system at energy scales comparable with T_K.

Finally, our method can be extended to deviations from the minimal topological Kondo models, such as the coupling of Majorana modes [9] caused by crossed-Andreev and cotunneling processes, and adopted to predict the transport features in a wide variety of strongly interacting nanodevices based on systems with quantum dots coupled to superconducting islands[41–44].

ACKNOWLEDGEMENTS

M.W., L.M., and M.B. are supported by the Villum Foundation (Research Grant No. 25310). This project has received funding from the European Union's Horizon 2020 research and innovation program under the Marie Skłodowska-Curie Grant Agreement No. 847523 "INTERACTIONS." C.-M.C. acknowledges the support by the Ministry of Science and Technology (MOST) under Grant No. 111-2112-M-110-006-MY3, and by the Yushan Young Scholar Program under the Ministry of Education (MOE) in Taiwan.

Supplemental Material

Minimal two-sites Kitaev chain description

In this Appendix we review the minimal two-site Kitaev chain description we use for modelling each nanowire. It should be noted that this model can be extended for longer chains. The Hamiltonian for the chain $\sigma = \uparrow, \downarrow$ is given by:

$$\widehat{H}^{(\sigma)}_{\rm kit} = \sum_{j=1}^{2} \left[-\mu_{\rm sys}\, \hat{d}^{\dagger}_{j,\sigma}\hat{d}_{j,\sigma} + \left(-t_{\rm sys}\hat{d}^{\dagger}_{j+1,\sigma}\hat{d}_{j,\sigma} + \Delta_P e^{i\Phi}\hat{d}_{j+1,\sigma}\hat{d}_{j,\sigma} + \text{H.c.} \right) \right], \tag{9}$$

where the index j labels the site and Φ is the superconducting phase of the aluminum backbone. In our simulations, we set $t_{\rm sys} = \Delta_P = 0.5t_0$ and $\mu_{\rm sys} = 0.01t_0$ to avoid a perfect degeneracy of the states. Before constructing the

MPS representation of the full system, we diagonalize the quadratic Hamiltonians in Equation (9) and define the quasiparticle excitations.

For simplicity, in the following, we consider only the upper chain, as the two chains are indistinguishable at equilibrium.

The physics of the MZMs is manifest by expressing each fermionic operator in terms of two Majorana fermions. In the case of the upper wire, we define:

$$\hat{d}_{j,\uparrow} = \frac{\mathrm{e}^{-i\Phi/2}}{2}\left(\hat{\gamma}_{j,B} - i\hat{\gamma}_{j,A}\right) \tag{10}$$

as schematically represented in Fig. 6. We consider the limit with $\mu_{\mathrm{sys}} = 0$ and $\Delta_P = t_{\mathrm{sys}}$, such that the Hamiltonian is given by $\widehat{H}^{(\uparrow)}_{\mathrm{kit}} = -i\Delta_P \hat{\gamma}_{2,A}\hat{\gamma}_{1,B}$ and couples Majorana fermions only at adjacent lattice sites (Fig. 6). The ends of the chain support the unpaired MZMs $\hat{\gamma}_1 = \hat{\gamma}_{1,A}$ and $\hat{\gamma}_2 = \hat{\gamma}_{2,B}$ which allow us to define the zero-energy quasiparticle operator $\hat{f}_{0,\uparrow}$ introduced in the main text. In the quasiparticle basis, the first excited state has energy $\epsilon_{1,\uparrow} = 2\Delta_P$ and corresponds to the operator $\hat{f}_{1,\uparrow} = (\hat{\gamma}_{2,A} - i\hat{\gamma}_{1,B})/2$, such that the Hamiltonian can be written as

$$\widehat{H}^{(\uparrow)}_{\mathrm{Kit}} = 2\Delta_P\left(\hat{f}^{\dagger}_{1,\uparrow}\hat{f}_{1,\uparrow} - 1/2\right). \tag{11}$$

The same construction is valid for the lower chain.

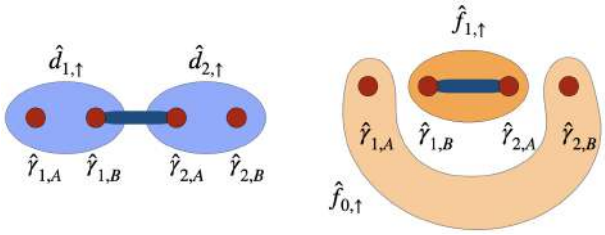

Figure 6. Each fermionic site of the Kitaev chain can be decomposed in two Majorana operators to make the MZMs physics more transparent. Quasiparticles states are represented schematically on the right. The thick blue link represents the interaction in Eq. (11).

The matrix product state construction

Auxiliary charge site

In order to simulate the topological Kondo model, we need to account for both its superconducting pairing and the charging energy of the Cooper-pair box. Importantly, the mean field BCS description of the superconducting system does not preserve the total particle number, but only its parity. This means that we cannot deduce the total charge of the Cooper-pair box $\hat{N}$ directly from the quasiparticle MPS construction. In order to overcome this problem we add an independent auxiliary charge site to the tensor network representation to keep track of the charge and its dynamics [16, 29].

First of all, one can promote the SC phase $\mathrm{e}^{-i\Phi/2}$ in (10) as the operator $\mathrm{e}^{-i\hat{\Phi}/2}$ which lowers the number of electrons on the box by one (due to the charge phase relation $[\hat{N}, \hat{\Phi}] = -2i$). In this way, the decomposition in Eq. (10) enables to separate this charge degree of freedom from the quasiparticle number. We can therefore describe charge dynamics by adding to our MPS an auxiliary site whose local Hilbert space is spanned by the eigenstates $|N\rangle$ of the charge $\hat{N}$ [16].

The tunneling Hamiltonian $\widehat{H}_{\mathrm{t}}$ becomes the sum of three-site operators of the form:

$$\widehat{H}_{\mathrm{t}} = -\sum_{\alpha=1}^{4}\sum_{\sigma,n} J_\alpha \mathrm{e}^{i\hat{\Phi}/2}\left[\left(u_{\alpha,\sigma,n}\hat{f}^{\dagger}_{\sigma,n} + v_{\alpha,\sigma,n}\hat{f}_{\sigma.n}\right)\hat{c}_{\alpha,1} \qquad + \mathrm{H.c.}\right]. \tag{12}$$

where the operator $\mathrm{e}^{\pm i\hat{\Phi}/2}$ acts on the auxiliary site and raises/lowers the charge eigenvalue N. Finally, charging energy costs are straightforwardly taken into account by considering the state of the auxiliary site, via $\widehat{H}_c = E_c\left(\hat{N} - n_g\right)^2$.

The auxiliary charge site construction is numerically implemented by restricting its local Hilbert, $N \in [-N_{\max}, N_{\max}]$, with $N_{\max} = 5$ (such that $e^{\pm i\hat{\Phi}/2}$ are represented as 11×11 matrices). Moreover, to remove the redundancy introduced by the auxiliary site, we constrain the parity of $\hat{N}$ to be the same as the parity of the total occupation of the quasiparticle states in the Majorana Cooper-pair box [16]. Namely, once defining the operator

$$\widehat{P} = (-1)^{\hat{N}+\sum_{n,\sigma} \hat{f}^\dagger_{n,\sigma}\hat{f}_{n,\sigma}}\,, \tag{13}$$

the following relation

$$\widehat{P}|\psi_{\rm phys}\rangle = |\psi_{\rm phys}\rangle, \tag{14}$$

has to be valid for any physical states $|\psi_{\rm phys}\rangle$. Our MPS and matrix product operator construction encodes such $\mathbb{Z}_2$ constraint.

TDVP Dynamics and transport quantities

We simulate the dynamics of the system through the TDVP algorithm, which is not limited by the long-range Hamiltonian resulting from the energy basis choice for the MPS. The Hamiltonian $\widehat{H}$ is represented as a matrix product operator of maximum bond dimension $\chi = 16$.

Through a suitable choice of the system size and Wilson decay length ξ, we observe the emergence of non-equilibrium quasi-steady states, that provide faithful descriptions of the physical behavior of the (infinite) system in its stationary state (see, for instance, Refs. [45, 46]). An example of the current after the quench is depicted in Fig. 7(a). To extract the values of the currents analyzed in the main text, we average the signal after it reaches the stationary value and estimate the errorbars through standard binning techniques.

Thanks to the chosen basis, after the quantum quench, the entanglement entropy of the system increases logarithmically with time [16, 47] and it is mainly localized in an energy window proportional to the voltage bias. Outside that window, the entanglement entropy is mostly time-independent, as we show in Fig. 7(b) and (c). See Ref. [16] for more details about the MPS construction and dynamics.

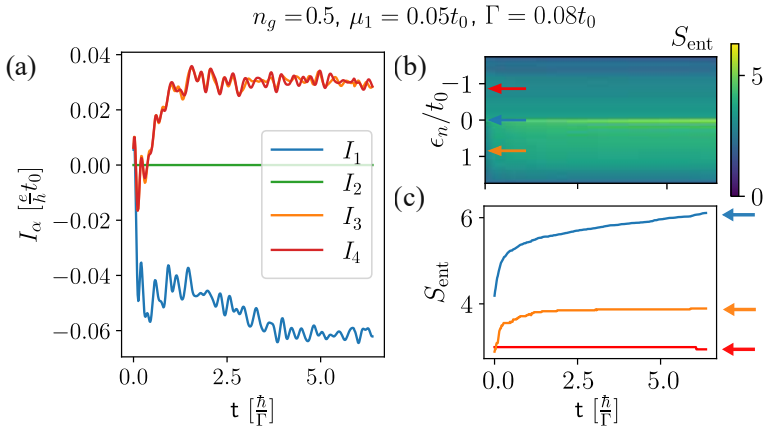

Figure 7. Typical dynamics of the current and entanglement entropy after a quantum quench for a three-terminal device. (a) Time dependence of the current on each lead. I_1 has a negative sign because it is the only in-going current. $I_2 = 0$ because the corresponding lead is decoupled from the device. (b) Entanglement entropy at each bond of the MPS as a function of energy and time. The three arrows mark the horizontal line cuts corresponding to the curves shown in panel (c). Simulation parameters: $\mathcal{L} = 100$, $\xi = 32$.

We finally observe that the Hamiltonian we adopt to describe the double-nanowire model displays an additional symmetry with respect to the most common topological Kondo models [4–6]. Indeed, the dynamics we analyze separately preserves the two fermionic parities:

$$\hat{P}_\uparrow = (-1)^{\sum_{\alpha=1,2}\sum_{l=1}^{\mathcal{L}} \hat{c}^\dagger_{\alpha,l}\hat{c}_{\alpha,l}+\sum_{n=0,1}\hat{f}^\dagger_{n,\uparrow}\hat{f}_{n\uparrow}}\,, \tag{15}$$

$$\hat{P}_\downarrow = (-1)^{\sum_{\alpha=3,4}\sum_{l=1}^{\mathcal{L}} \hat{c}^\dagger_{\alpha,l}\hat{c}_{\alpha,l}+\sum_{n=0,1}\hat{f}^\dagger_{n,\downarrow}\hat{f}_{n\downarrow}}\,. \tag{16}$$

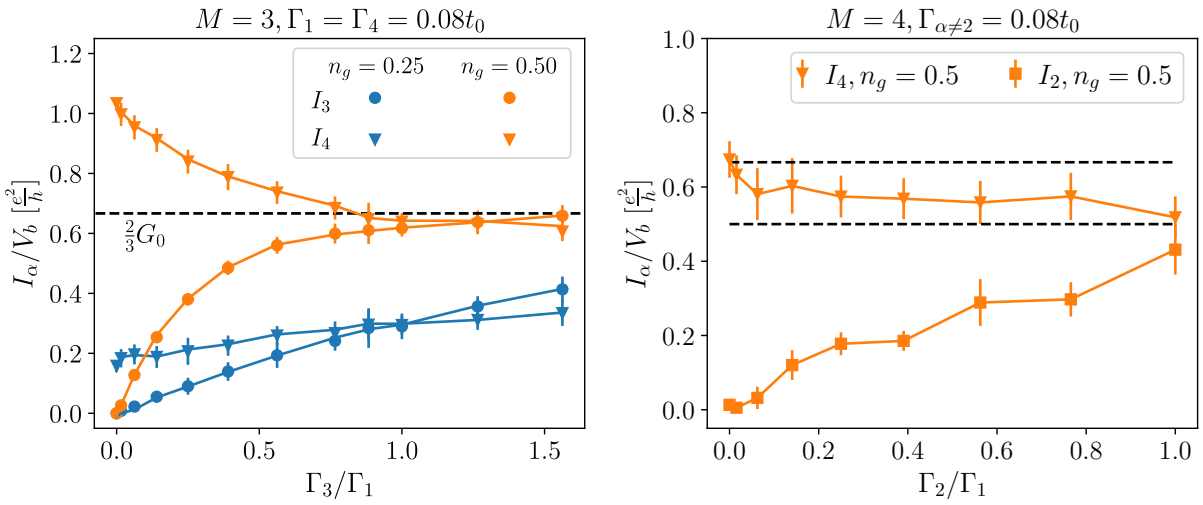

Figure 8. Left: Nonlocal current as a function of the varying coupling strength Γ_3, at the charge degeneracy point $n_g = 0.5$ and in the even valley $n_g = 0.25$. Right: Nonlocal currents as a function of the varying coupling strength Γ_2, at the charge degeneracy point $n_g = 0.5$. The two horizontal dashed lines mark $G = \frac{2}{M}G_0$ for $M = 3, 4$. In both panels $E_c = 0.4$, $eV_b = 0.01t_0$, $L = 100$, and $\xi = 32$.

These symmetries reflect the fact that we are neglecting crossed-Andreev and direct cotunneling processes mediated by the superconducting island between the two nanowires. These conservations have the important effect of breaking the particle-hole-like symmetry of the dynamics between systems characterized by n_g and $1 - n_g$, as can be seen from Fig.[5] of the main text, at large coupling. The initial ground states $|00\rangle$ ($N = 0$) for $n_g < 0.5$ and $|10\rangle$ ($N = 1$) for $n_g > 0.5$ correspond to different sectors of $\hat{P}_\downarrow$ and are not mapped one into the other by the symmetry.

Further transport results

Asymmetric couplings

Here we investigate the effect of introducing an asymmetry in the couplings Γ_α on the transport properties.

We first analyze a device with three leads ($\Gamma_2 = 0$), where two of them have the same coupling strength $\Gamma_1 = \Gamma_4 = 0.08t_0$, which corresponds to the strong coupling regime explored in the main text, while the third is varied. In Fig. 8 (right panel) we plot the nonlocal currents I_3 and I_4 divided by the bias on lead 1 as we vary $\Gamma_3 \in [0, 1.6\Gamma_1]$. At the charge degeneracy point (orange symbols), the data suggest that the current is approximately stable for a broad range of couplings $\Gamma_3 \gtrsim \Gamma_1$, and, within the error bars, is compatible with the linear conductance associated to the TKE (horizontal dashed line). As Γ_3 decreases, I_3 also decreases and vanishes when the lead is finally decoupled from the system. At the same time, I_4 increases and approaches the quantized value $I_4 = G_0 V_b$ when the device has only two terminals, as we expect from the resonant tunneling mediated by MZMs with symmetric couplings [16, 48]. As we move deeper in the Coulomb valley ($n_g = 0.25$, blue symbols), the system appears to be further away from the TKE regime and the current shows a roughly linear dependence on Γ_3. Interestingly, however, the current I_4 decreases upon switching off Γ_3, despite keeping Γ_4 constant. This is in contrast with the single resonant level prediction

$$G_{\rm rl}(n_g, \mu) = \frac{e^2}{h} \frac{4\Gamma^2}{M^2\Gamma^2 + 4[\mu - E_c(1 - 2n_g)]^2} \ , \tag{17}$$

confirming that a contribution to the current originating from a strongly coupled state is present also in the Coulomb valleys, even though the TKE quantization of the conductance is not recovered for the chosen parameter ranges.

Let us now focus on the crossover between $M = 4$ and $M = 3$: we consider a four-terminal device where we tune the coupling Γ_2 from the symmetric configuration, $\Gamma_\alpha = 0.08t_0$ on any lead, to $\Gamma_2 = 0$, while keeping a small voltage bias $eV_b = 0.01t_0$ on lead 1. In Fig. 8 (right panel) we show the nonlocal currents I_2 and I_4 for $n_g = 0.5$, where the Kondo tmperature is maximal, as we switch off Γ_2. When $\Gamma_2 = \Gamma_1$, the current on both leads is again compatible with the TKE prediction with $M = 4$ (lower horizontal dashed line). As Γ_2 decreases, I_2 and I_4 display opposite behaviors;

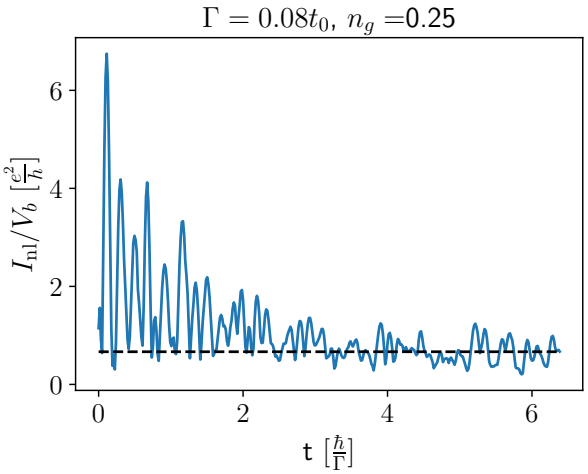

Figure 9. Time dependence of the nonlocal current for $M = 3$ and $n_g = 0.25$, averaged over 4 values of $\xi = 2, 4, 8, 16$. The horizontal dashed line marks the TKE prediction.

the former decreases and vanishes following Γ_2 while the latter displays first a rather flat plateau followed by a rapid increase to match the TKE prediction for $M = 3$ when $\Gamma_2 \to 0$ (higher horizontal dashed line). The current on lead 3 (data not shown) follows closely the signal on I_4.

Low bias transport

Transport simulations at very low bias are hampered by a low signal-to-noise ratio that prevents from an accurate estimate of the average current in the nonequilibrium quasi-steady state. This limitation is relevant for low Kondo temperatures as, for instance, in the Coulomb valleys. To partially circumvent this issue, inspired by the so-called z-trick [49] commonly used in NRG methods, here we consider data obtained by averaging over different logarithmic discretizations of the energy levels of the leads. In particular, we average the currents over different decay lengths of the hopping amplitude in the leads. In Fig. 9 we plot an example of this procedure: we consider $n_g = 0.25$ (even-parity Coulomb valley), $E_c = 0.4t_0$, $M = 3$, and $\Gamma = 0.08t_0$. The corresponding Kondo temperature extracted from the magnetization dynamics is $T_K \sim 0.01t_0$, see Fig.[3](c) of the main text. To capture the transport signature of the TKE, we perform different simulations with a small bias $eV_b = 10^{-3}t_0$ on lead 1 and $\xi = \{2, 4, 8, 16\}$. We then average the outgoing current over the different values of ξ. This reduces the amplitude of the current oscillations, and leads to a good match with the TKE prediction $G_{\rm TKE} = \frac{2}{M}G_0$ also in the Coulomb valleys.

Finite bias corrections

Finally, we discuss the finite bias corrections to the currents close to TKE linear response behaviour, $I = \frac{2}{M}G_0V_b$. In a renormalization group sense, a power law correction $G = 2G_0/M - AV_b^\alpha$ is related to the scaling dimension of the most relevant operator which arises at the TKE fixed point. In particular, a fixed point described by the Fermi liquid (FL) theory displays a quadratic correction for the conductance ($\alpha = 2$). The topological Kondo effect, instead, is predicted to display non-Fermi liquid corrections defined by the universal fractional exponent $\alpha = 2(1-2/M)$[11, 40].

In Fig. 10, we show the bias dependence of the current deviation from the TKE regime, $I - \frac{2}{M}G_0V_b$, for $M = 3, 4$. The data show a clear power-law behavior, particularly for bias values V_b that are not excessively small (such that the signal-to-noise ratio is reliable). In the displayed cases, the deviation of the current from the power-law fits is below the numerical precision $\sim 10^{-3}$.

In all cases, we observe a non-Fermi liquid scaling which significantly deviates from the cubic FL behaviour of the current V_b^3. However, the fitted exponents do not match the RG predicted values $\alpha + 1 = 3 - 4/M$. The absence of a clear separation of energy scales in the problem might be a source of deviation from the perturbative RG analysis. Moreover, close to the charge degeneracy point, intermediate fixed points are believed to emerge [11]. Finally, the

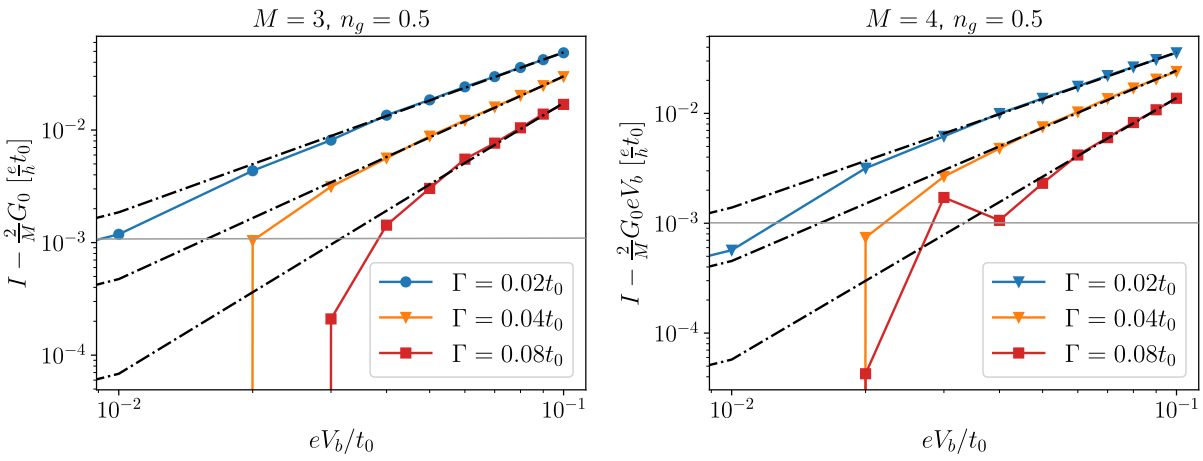

Figure 10. Deviation of the average non-local current from the linear regime $I = \frac{2}{M} G_0 V_b$, for $M = 3, 4$, $n_g = 0.5$ and $E_c = 0.4t_0$. The black dashed lines are power-law fits bx^a of the data. The values of a for $M = 3$ are 1.42(1) ($\Gamma = 0.02t_0$), 1.80(1) ($\Gamma = 0.04t_0$), and 2.41(3) ($\Gamma = 0.08t_0$), while for $M = 4$ we obtain 1.41(2) ($\Gamma = 0.02t_0$), 1.73(2) ($\Gamma = 0.04t_0$), and 2.38(4) ($\Gamma = 0.08t_0$). The grey line indicates the numerical precision.

fitted exponents seems to depend continuously on the coupling strength Γ and, while this analysis has shed light on a non-Fermi liquid behaviour, further analysis is needed to understand these power-law corrections.

[1] E. Prada, P. San-Jose, M. W. de Moor, A. Geresdi, E. J. Lee, J. Klinovaja, D. Loss, J. Nygård, R. Aguado, and L. P. Kouwenhoven, From andreev to majorana bound states in hybrid superconductor–semiconductor nanowires, Nature Reviews Physics **2**, 575 (2020).

[2] C. W. J. Beenakker, Search for non-Abelian Majorana braiding statistics in superconductors, SciPost Phys. Lect. Notes , 15 (2020).

[3] K. Flensberg, F. von Oppen, and A. Stern, Engineered platforms for topological superconductivity and majorana zero modes, Nature Reviews Materials **6**, 944 (2021).

[4] B. Béri and N. R. Cooper, Topological Kondo effect with Majorana fermions, Phys. Rev. Lett. **109**, 156803 (2012).

[5] B. Béri, Majorana-Klein hybridization in topological superconductor junctions, Phys. Rev. Lett. **110**, 216803 (2013).

[6] A. Altland and R. Egger, Multiterminal Coulomb-Majorana junction, Phys. Rev. Lett. **110**, 196401 (2013).

[7] D. Liu, Z. Cao, X. Liu, H. Zhang, and D. E. Liu, Topological kondo device for distinguishing quasi-majorana and majorana signatures, Phys. Rev. B **104**, 205125 (2021).

[8] K. Michaeli, L. A. Landau, E. Sela, and L. Fu, Electron teleportation and statistical transmutation in multiterminal Majorana islands, Phys. Rev. B **96**, 205403 (2017).

[9] A. Altland, B. Béri, R. Egger, and A. M. Tsvelik, Multichannel Kondo impurity dynamics in a Majorana device, Phys. Rev. Lett. **113**, 076401 (2014).

[10] M. R. Galpin, A. K. Mitchell, J. Temaismithi, D. E. Logan, B. Béri, and N. R. Cooper, Conductance fingerprint of majorana fermions in the topological kondo effect, Phys. Rev. B **89**, 045143 (2014).

[11] L. Herviou, K. Le Hur, and C. Mora, Many-terminal Majorana island: From topological to multichannel Kondo model, Phys. Rev. B **94**, 235102 (2016).

[12] F. Buccheri, A. Nava, R. Egger, P. Sodano, and D. Giuliano, Violation of the wiedemann-franz law in the topological kondo model, Phys. Rev. B **105**, L081403 (2022).

[13] A. Altland, B. Béri, R. Egger, and A. M. Tsvelik, Bethe ansatz solution of the topological Kondo model, J. Phys. A: Math. Theor. **47**, 265001 (2014).

[14] F. Buccheri, H. Babujian, V. E. Korepin, P. Sodano, and A. Trombettoni, Thermodynamics of the topological Kondo model, Nucl. Phys. B **896**, 52 (2015).

[15] M. Papaj, Z. Zhu, and L. Fu, Multichannel charge Kondo effect and non-Fermi-liquid fixed points in conventional and topological superconductor islands, Phys. Rev. B **99**, 014512 (2019).

[16] C.-M. Chung, M. M. Wauters, and M. Burrello, Matrix product state simulations of quantum quenches and transport in coulomb blockaded superconducting devices, Phys. Rev. B **106**, 094308 (2022).

[17] T. Kanne, D. Olsteins, M. Marnauza, A. Vekris, J. C. Estrada Saldaña, S. Loric, R. D. Schlosser, D. Ross, S. Csonka, K. Grove-Rasmussen, and J. Nygård, Double nanowires for hybrid quantum devices, Advanced Functional Materials **32**, 2107926 (2022).

[18] A. Vekris, J. C. Estrada Saldaña, T. Kanne, T. Hvid-Olsen, M. Marnauza, D. Olsteins, M. M. Wauters, M. Burrello, J. Nygård, and K. Grove-Rasmussen, Electronic transport in double-nanowire superconducting islands with multiple terminals, Nano Letters **22**, 5765 (2022), pMID: 35833741, https://doi.org/10.1021/acs.nanolett.2c01161.

[19] Y. Oreg, G. Refael, and F. von Oppen, Helical liquids and majorana bound states in quantum wires, Phys. Rev. Lett. **105**, 177002 (2010).

[20] R. M. Lutchyn, J. D. Sau, and S. Das Sarma, Majorana fermions and a topological phase transition in semiconductor-superconductor heterostructures, Phys. Rev. Lett. **105**, 077001 (2010).

[21] S. Vaitiekėnas, R. S. Souto, Y. Liu, P. Krogstrup, K. Flensberg, M. Leijnse, and C. M. Marcus, Evidence for spin-polarized bound states in semiconductor–superconductor–ferromagnetic-insulator islands, Phys. Rev. B **105**, L041304 (2022).

[22] R. S. Souto, M. M. Wauters, K. Flensberg, M. Leijnse, and M. Burrello, Multiterminal transport spectroscopy of subgap states in coulomb-blockaded superconductors, Phys. Rev. B **106**, 235425 (2022).

[23] B. van Heck, A. R. Akhmerov, F. Hassler, M. Burrello, and C. W. J. Beenakker, Coulomb-assisted braiding of Majorana fermions in a Josephson junction array, New J. Phys. **14**, 035019 (2012).

[24] S. Plugge, A. Rasmussen, R. Egger, and K. Flensberg, Majorana box qubits, New J. Phys. **19**, 012001 (2017).

[25] See supplemental material for further data and technical details.

[26] K. G. Wilson, The renormalization group: Critical phenomena and the Kondo problem, Rev. Mod. Phys. **47**, 773 (1975).

[27] L. G. G. V. Dias da Silva, F. Heidrich-Meisner, A. E. Feiguin, C. A. Büsser, G. B. Martins, E. V. Anda, and E. Dagotto, Transport properties and Kondo correlations in nanostructures: Time-dependent DMRG method applied to quantum dots coupled to Wilson chains, Phys. Rev. B **78**, 195317 (2008).

[28] M. M. Wauters, C.-M. Chung, L. Maffi, and M. Burrello, Simulations of the dynamics of quantum impurity problems with matrix product states (2023), arXiv:2304.13756 [cond-mat.str-el].

[29] A. Keselman, C. Murthy, B. van Heck, and B. Bauer, Spectral response of Josephson junctions with low-energy quasiparticles, SciPost Phys. **7**, 50 (2019).

[30] J. Haegeman, J. I. Cirac, T. J. Osborne, I. Pižorn, H. Verschelde, and F. Verstraete, Time-dependent variational principle for quantum lattices, Phys. Rev. Lett. **107**, 070601 (2011).

[31] J. Haegeman, C. Lubich, I. Oseledets, B. Vandereycken, and F. Verstraete, Unifying time evolution and optimization with matrix product states, Phys. Rev. B **94**, 165116 (2016).

[32] M. Yang and S. R. White, Time-dependent variational principle with ancillary Krylov subspace, Phys. Rev. B **102**, 094315 (2020).

[33] M. Fishman, S. R. White, and E. M. Stoudenmire, The ITensor Software Library for Tensor Network Calculations, SciPost Phys. Codebases , 4 (2022).

[34] The source code can be found in the repository `https://github.com/chiamin/QuenchTranportTwoChains`.

[35] D. Lobaskin and S. Kehrein, Crossover from nonequilibrium to equilibrium behavior in the time-dependent kondo model, Phys. Rev. B **71**, 193303 (2005).

[36] F. B. Anders and A. Schiller, Real-time dynamics in quantum-impurity systems: A time-dependent numerical renormalization-group approach, Phys. Rev. Lett. **95**, 196801 (2005).

[37] M. F. Cavalcante, R. G. Pereira, and M. C. O. Aguiar, Quench dynamics of the kondo effect: Transport across an impurity coupled to interacting wires, Phys. Rev. B **107**, 075110 (2023).

[38] J. I. Väyrynen, A. E. Feiguin, and R. M. Lutchyn, Signatures of topological ground state degeneracy in majorana islands, Phys. Rev. Res. **2**, 043228 (2020).

[39] Z. He and A. J. Millis, Entanglement entropy and computational complexity of the Anderson impurity model out of equilibrium: Quench dynamics, Phys. Rev. B **96**, 085107 (2017).

[40] A. Zazunov, A. Altland, and R. Egger, Transport properties of the Coulomb–Majorana junction, New J. Phys. **16**, 015010 (2014).

[41] C.-X. Liu, G. Wang, T. Dvir, and M. Wimmer, Tunable superconducting coupling of quantum dots via andreev bound states in semiconductor-superconductor nanowires, Phys. Rev. Lett. **129**, 267701 (2022).

[42] A. Tsintzis, R. S. Souto, and M. Leijnse, Creating and detecting poor man's majorana bound states in interacting quantum dots, Phys. Rev. B **106**, L201404 (2022).

[43] T. Dvir, G. Wang, N. van Loo, C.-X. Liu, G. P. Mazur, A. Bordin, S. L. D. Ten Haaf, J.-Y. Wang, D. van Driel, F. Zatelli, X. Li, F. K. Malinowski, S. Gazibegovic, G. Badawy, E. P. A. M. Bakkers, M. Wimmer, and L. P. Kouwenhoven, Realization of a minimal Kitaev chain in coupled quantum dots, Nature **614**, 445 (2023).

[44] A. Tsintzis, R. S. Souto, K. Flensberg, J. Danon, and M. Leijnse, Roadmap towards majorana qubits and nonabelian physics in quantum dot-based minimal kitaev chains (2023), arXiv:2306.16289 [cond-mat.mes-hall].

[45] B. Bertini, M. Collura, J. De Nardis, and M. Fagotti, Transport in out-of-equilibrium xxz chains: Exact profiles of charges and currents, Phys. Rev. Lett. **117**, 207201 (2016).

[46] F. H. L. Essler and M. Fagotti, Quench dynamics and relaxation in isolated integrable quantum spin chains, Journal of Statistical Mechanics: Theory and Experiment **2016**, 064002 (2016).

[47] M. M. Rams and M. Zwolak, Breaking the entanglement barrier: Tensor network simulation of quantum transport, Phys. Rev. Lett. **124**, 137701 (2020).

[48] B. van Heck, R. M. Lutchyn, and L. I. Glazman, Conductance of a proximitized nanowire in the Coulomb blockade regime, Phys. Rev. B **93**, 235431 (2016).

[49] M. Yoshida, M. A. Whitaker, and L. N. Oliveira, Renormalization-group calculation of excitation properties for impurity models, Phys. Rev. B **41**, 9403 (1990).

pcs Center for Theoretical Physics of Complex Systems

ibs Institute for Basic Science

Center for Theoretical Physics
of Complex Systems

pcs@ibs.re.kr
+82 428788633

24.05.2023

Prof. Chia-Min Chung
National Sun Yat-Sen University
Taiwan

Dear Prof. Chung,

We have the pleasure of inviting you to participate in the meeting of the Advanced Study Group (ASG) *Tensor Network Approaches to Many-Body Systems* organized by the Center for Theoretical Physics of Complex Systems (PCS) of the Institute for Basic Science (IBS) in Daejeon, Republic of Korea in the periods of July 9 – July 16, 2023.

Your accommodation will be booked and covered by the PCS. We will also purchase your flight ticket (economy class). Please contact us at pcs@ibs.re.kr as soon as possible.

Furthermore, we can support your local expenses in Korea, provided the total duration of your visit in Korea does not exceed 7 working days, or you secure a C–4 visa prior to the entry into the Republic of Korea.

You are expected to secure an entry visa into the Republic of Korea, if necessary – please contact us at pcs@ibs.re.kr for details well in advance of your visit. Moreover, the PCS recommends you to arrange a travel health insurance for the entire duration of your stay.

As the PCS aims to further develop its active Visitor Program, we are confident that you will find here a stimulating environment for carrying out your research work. More information about the PCS can be found at pcs.ibs.re.kr.

Yours sincerely,

Prof. Sergej Flach, Director
Center for Theoretical Physics of Complex Systems
Institute for Basic Science

O5-CMD 強關聯系統與量子多體動力學 Topical Symposia：Correlated many-body dynamics Chair:Chia-Min Chung (鍾佳民) 物理系館36206室 Room 36206 of Dept. of Physics	Wei-Lin Tu Korea University Invited speaker		Chia-Min Chung 國立中山大學 Invited speaker	
O5-MSP 磁性與自旋物理 Magnetism/Spin Physics Chair:Tzu-Hung Chuang (莊子弘) 土木系館4509室 Room 4509 of Dept. of Civil Eng.	Chao-Yao Yang National Yang Ming Chiao Tung University Invited speaker		Ko-Hsuan Mandy Chen National Tsing Hua University	Jhen-Yong Hong Tamkang University
O5-OP 光學 Optics and Photonics Chair:Chaw-Keong Yong (楊超強) 化學系館36104室 Room 36104 of Dept. of Chemistry	Chang-Hua Liu National Tsing Hua University Invited speaker		Lam Yen Thi Nguyen National Chung Cheng University	Bor-Wei Liang National Taiwan Normal University
O5-PF 粒子與場 Particles and Fields Chair:Yi Yang (楊毅) 測量系館55170室 Room 55170 of Dept. of Geomatics	C.-J. David Lin National Yang Ming Chiao Tung University	Sheng-Hong Lai National Yang Ming Chiao Tung University	Patrick Copinger Academia Sinica	Zheng-Gang Chen National Taiwan University
O5-QI 量子資訊與量子計算 Quantum Information and Quantum Computing Chair:Hung-Bin Chen (陳宏斌) 土木系館4507室 Room 4507 of Dept. of Civil Eng.	Hsin-Yu Hsu Center for Quantum Frontiers of Research & Technology (QFort) National Cheng Kung University	Gelo Noel Tabia National Cheng Kung Univeristy National Center for Theoretical Sciences		